DEVELOPMENT OF SELF-DIAGNOSTIC COMPOSITE STRUCTURES USING EMBEDDED FIBER-BRAGG GRATING SENSORS

By

Anthony Dellicolli

A THESIS

Submitted to
Michigan State University
in partial fulfillment of the requirements
for a degree of

MASTER OF SCIENCE

ENGINEERING MECHANICS

2012

ABSTRACT

DEVELOPMENT OF SELF-DIAGNOSTIC COMPOSITE STRUCTURES USING EMBEDDED FIBER-BRAGG GRATING SENSORS

By

Anthony Dellicolli

The use of composite materials in large structures has grown rapidly over the past decade. Consequently, the need to identify a technique for robust structural health monitoring of these composite structures has arisen. Developing composite structures that are capable of diagnosing their own structural health using embedded sensors would allow proper monitoring of structural integrity and further increase the advantages of working with composites. Fiber-Bragg Grating (FBG) sensors have been used to monitor the structural health of composite structures in real-time and are well suited to the task due to their non-intrusive size and multiplexing capability.

In this thesis, the durability of embedded FBG sensors is first explored through tension and impact testing. The effect of non-uniform strain on the embedded FBG sensor is investigated through the implementation of a numerical analysis that can predict a reflection spectrum when given a non-uniform strain distribution. It will be shown that a new proposed reflection spectrum interrogation method will improve crack detection capability. The new interrogation method is validated by multiple experiments in which embedded FBG sensors are used to monitor crack propagation in composite specimens using various geometries. Health monitoring capabilities are extended to thick-section composite panels with multiple FBG sensors to detect and monitor impact damage. The use of embedded FBG sensors is found to be an effective method of structural health monitoring in multiple applications.

This thesis is dedicated to my family for making this all possible and always being there for me.

ACKNOWLEDGEMENTS

I would like to thank everyone who played a part in my schooling at Michigan State University as I feel everything I have learned here has contributed to the completion of this thesis. I would like to thank Dr. Soonsung Hong for believing in me and guiding me through all the work and research to earn my Masters. Thank you to the U.S. Tank Army Research, Development and Engineering Center (TARDEC) and the Composite Vehicle Research Center for their funding and allowing me the opportunity to conduct research that I truly believe in. Thank you to all my fellow research assistants and students that shared a laugh when we were too tired to stare at computer screens any longer.

TABLE OF CONTENTS

LIST OF TABLES

LIST OF FIGURES

CHAPTER 1
INTRODUCTION

Motivation

The use of composite materials in large structures has become increasingly prevalent due to the high stiffness-to-weight ratio of the materials. Inspection of large areas of composite structures using the conventional non-destructive testing approach is a time-consuming process. Consequently, the need to develop structural health monitoring (SHM) techniques for composite structures has emerged. Developing smart composite structures that are capable of diagnosing their own structural health using embedded sensors will allow real-time monitoring of defects and damage in composites and enable condition-based maintenance of the composite structures.

Fiber-Bragg grating (FBG) sensors developed for strain sensing capability have been extensively investigated to be used for structural health monitoring of composite structures. The FBG sensors are well-suited for the SHM applications due to their non-intrusive size and excellent multiplexing capability and can be easily embedded in composite structures during the manufacturing process. The reflection spectrum obtained from the embedded FBG sensors contains information on local deformation which can be related to the location and extent of defects and damage.

However, the existing interrogation method developed for strain measurement by monitoring the peak-wavelength shift of the reflection spectrum has several limitations to be used for damage identification. The limitations include the lack of quantitative damage monitoring capability and the ambiguity in differentiating normal structural response from the abnormal response caused by damage. Therefore, a new interrogation method which will allow early detection and quantitative monitoring of damage progression is required for the development of a robust health monitoring system.

Another challenge comes from the concern that the failure of the embedded sensor will result in a loss of structural health monitoring capabilities. Thus, the durability of embedded FBG sensors subjected to static and dynamic loading conditions must be verified to ensure the sensor's ability to maintain its functionality. Once the sensor's durability is confirmed, validation experiments are required to demonstrate the improved damage monitoring capabilities of the new interrogation method. The experiments should be designed to create stable and well-characterized defects in composites, so that the quantitative monitoring capability could be evaluated.

Finally, the structural health monitoring abilities of the FBG sensors must be extended to large-scale structures to make further progress towards full-scale, realistic applications. Structural health monitoring of a large-scale panel requires multiple embedded FBG sensors to adequately monitor damage in large areas.

Objectives

In this thesis, the following objectives have been established for the development of self-diagnostic composite structures using embedded FBG sensors.

- Demonstrate the durability and survivability of FBG sensors embedded in composite laminates when subjected to static and impact loading conditions.
- Design interlaminar fracture tests that will be used to validate structural health monitoring capability of embedded FBG sensors for crack detection and monitoring.
- Develop a new interrogation method well-suited to quantify the FBG reflection spectrum for damage monitoring by conducting numerical simulation of the spectral response of an FBG sensor under non-uniform strain.

- Demonstrate improved crack detection capability of the new interrogation method by performing validation experiments including interlaminar fracture and fatigue tests of composite laminates with embedded FBG sensors.

- Extend damage monitoring capabilities to a large-scale, thick-section composite panel with multiple embedded FBG sensors for detecting impact damage.

Scope

Chapter 3 presents durability testing of embedded FBG sensors in composite laminates subjected to quasi-static tensile loading and drop-weight impact loading. The ability of an FBG sensor to survive and maintain its functionality is demonstrated. These preliminary tests aim to counter the perceived fragility of FBG sensors and provide a baseline for further development of self-diagnostic composite structures.

Chapter 4 presents standard interlaminar fracture test procedures that are developed to determine the Mode-I and Mode-II fracture toughness of unidirectional fiber-reinforced composites. The specimen design and experimental procedures will be used in Chapter 6 to demonstrate the structural health monitoring capability of embedded FBG sensors.

In Chapter 5, a new interrogation method is proposed to analyze the reflection spectrum of FBG sensors for health monitoring purposes. Following a numerical analysis designed to predict the effect of non-uniform strain on the FBG reflection spectrum, the spectral bandwidth and center wavelength are identified as simple and robust indicators for tracking the growth of defects in composite structures.

In Chapter 6, the effectiveness of the new interrogation method is demonstrated by conducting validation experiments which include interlaminar fracture and fatigue testing of composite specimens with an embedded FBG sensor. The crack-detection capability of the proposed interrogation method is compared to that of the existing peak-wavelength monitoring technique under quasi-static and cyclic loading conditions.

Chapter 7 presents an application of multiple embedded FBG sensors to impact damage monitoring in a large-scale, thick-section composite panel. The method utilizes the sensors' response to a simulated in-service loading experienced by the composite structure after sustaining damage.

CHAPTER 2
STATE OF THE ART

Structural Health Monitoring

With the increased use of composite materials in military vehicles and commercial airliners, developing a better understanding of the damage sustainability and failure behavior of composite structures becomes a crucial aspect in safely utilizing them. The development of structural health monitoring capabilities aims to improve passenger safety and increase the reliability of composites.

Structural health monitoring is the practice of embedding sensors in a composite structure to create real-time damage detection capabilities and allow the structure to diagnose its own structural health. Such sensors are typically embedded in the composite structure during the manufacturing process and have very little effect on the material properties. The sensors are designed to provide structural integrity information to an operator to allow for repair or replacement decisions based on damage size and severity. Some of the potential sensors that have been identified for this purpose include ultrasonic-based sensors and fiber optic sensors.

A decision matrix based on meeting key requirements, technology readiness level, existing limitations, mass, and cost produced piezoelectric, magnetostrictive, and fiber-Bragg grating sensors as the top three options to serve this purpose.

Potential Sensors for Structural Health Monitoring

Piezoelectric sensors utilize lead zirconate titanate (PZT) transducers and ultrasonic waves for structural health monitoring by relating changes in wave propagation to damage size and location. Piezoelectric sensors have been used successfully to identify cracking and delamination in composites [1-8]. They have also been used to effectively detect impact damage in composite structures [9-13]. The film-based nature of the sensors allows them to be applied to the surface of a composite or embedded within. The sensors are also well suited to use in composites with curved surfaces [1]. However, the embedment of piezoelectric sensors is more complicated than optical fiber sensors due to the presence of connecting wires [3]. Additionally, piezoelectric sensors have not been proven effective for use in thick composites.

Magnetostrictive sensors relate changes in the magnetic state of a magnetostrictive material to damage size and location using ultrasonic waves. These sensors can be embedded in composites as a film layer and have been shown to be capable of delamination detection [15-18] although no work could be found on impact damage detection.

Fiber-Bragg grating (FBG) sensors employ a refractive index embedded in a small length of an optical fiber to reflect a narrow bandwidth of light that changes as the sensor experiences strain. Their structural health monitoring capabilities have been employed in detecting both delamination [19-34] and impact damage [21, 35-43] in composites and offer efficient methods for quantitative characterization of defects and damages [27, 31-34]. FBG sensors have been chosen as the optimal sensors for structural health monitoring due to their non-intrusive size, multiplexing capabilities, and ease of imbedding.

Fiber-Bragg Grating Sensors

An FBG sensor is a short length of FBG contained in a polyimide coated optical fiber meant for fiber optic strain sensing purposes. FBG sensors are extremely sensitive to strain and can provide accurate axial strain measurements of a structure by monitoring the peak wavelength shift of the returned signal due to the linearly-proportional relationship between the peak wavelength shift and applied strain. They can be easily and quickly embedded in between plies of composite panels during the hand lay-up process and require minimal training to operate and obtain data without any calibration necessary. The multiplexing capability of FBG sensors allows for up to 100 sensors to be embedded in a single optical fiber thus providing many damage monitoring points in a structure without complicating the manufacturing process. The optical fiber is small in diameter (~0.15 – 0.25 mm) and has no effect on the material properties of the composite in which it is embedded. The sensor gauge length varies in size (~mm) to accommodate multiple damage types and sizes. FBG sensors remain reliable for great lengths of time due to their passive sensing ability and are suitable for applications in which the expected service time of a structure is multiple decades.

Principles of Fiber-Bragg Grating Sensors

An FBG sensor is designed to reflect light with a narrow bandwidth while transmitting all other wavelengths by using a sinusoidal variation in the refractive index of the fiber core. The wavelength of the reflected light, called the Bragg wavelength, is determined by

$$\lambda = 2n\Lambda \tag{1}$$

where n is the average refractive index and Λ is the grating period. A typical reflection spectrum of an FBG sensor is shown in Figure 1.

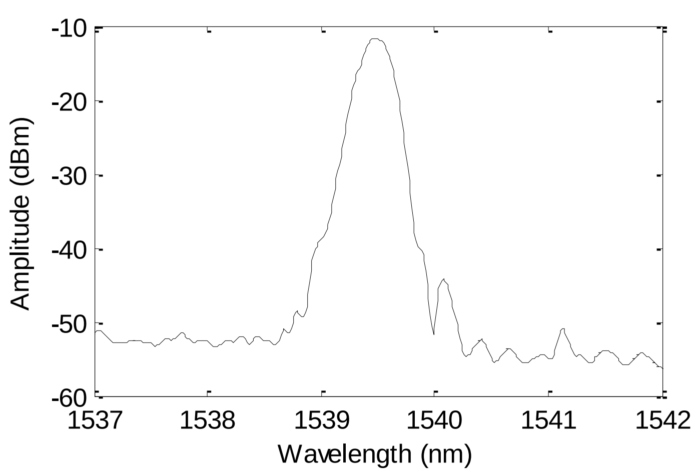

Figure 1. Typical reflection spectrum of an FBG sensor

When the FBG sensor is subjected to a uniform strain distribution, n and Λ can be expressed as [44]:

$$n = n_0 - \frac{n_0^3}{2}\left[P_{12}\varepsilon_1 + (P_{11} + P_{12})\frac{\varepsilon_2+\varepsilon_3}{2}\right] \tag{2}$$

$$\Lambda = (1 + \varepsilon_1)\Lambda_0 \tag{3}$$

where n_0 is the initial average refractive index, Λ_0 is the initial grating period at a strain-free state, $P_{11} = 0.17$ and $P_{12} = 0.36$ are the Pockel's constants of silica, ε_1 is an axial strain and ε_2 and ε_3 are transverse strains. An FBG sensor subjected to uniform strain along its gage length will reflect light with a different peak wavelength. Therefore, the axial strain can be determined by measuring the peak wavelength shift, $\Delta\lambda_B$, with respect to the initial Bragg wavelength of the FBG sensor, λ_B, [2] by

$$\varepsilon = \frac{(\Delta\lambda_B/\lambda_B)}{\left[1-\frac{1}{2}n_{eff}^2\{P_{12}-\upsilon(P_{11}+P_{12})\}\right]} \tag{4}$$

where n_{eff} is the effective index of refraction of the fundamental mode of the optical fiber, and $\upsilon = 0.16$ is the Poisson's ratio of silica.

Application of FBG Sensors to Structural Health Monitoring

The use of FBG sensor for the structural health monitoring of composite structures has become increasingly popular due to the low cost of introducing embedded FBG sensors relative to the benefits of creating self-diagnostic composite structures. The use of embedded FBG sensors could prevent the costly and time-intensive tear down inspection of structural components by providing structural integrity information. The real-time structural health monitoring ability increases the safety of composite vehicles by delivering information to operators as soon as the structure becomes compromised. This allows the operator the opportunity to immediately determine if the vehicle can continue service or if it must be repaired.

When an FBG sensor is subjected to a non-uniform strain distribution along the gage length, the spectral response will change as a function of the non-uniform strain distribution, and the linear relationship in (4) will no longer hold true. The reflection spectrum will become wider and may contain multiple peaks as the non-uniform strain increases (Figure 2).

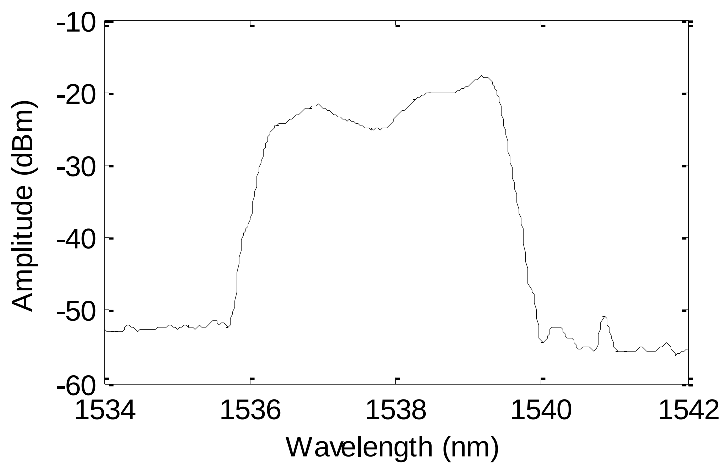

Figure 2. A reflection spectrum of a FBG sensor subjected to non-uniform strain

The spectrum broadening and multiple peaks due to the non-uniform strain fields can be used as indicators of strain concentration caused by the defects and damage in composite structures.

FBG Sensor Durability and Survivability

The possibility that FBG sensors could be too fragile and fail before the composite structures they are embedded in, resulting in a loss of structural health monitoring capabilities, is a concern that must be addressed. Typically, FBG sensors are given a strain limit by the manufacturer and exceeding this point potentially results in unreliable data and damage to the sensor. While exceeding this point will not cause the sensor to lose its signal entirely, it could result in residual damage and reduce the strength of the signal even if the strain being sustained by the sensor is returned to a value below the limit. Ang et al. [45] found that above the prescribed strain limit, the reflection spectrum of an uncoated, surface-mounted FBG sensor progressively deteriorated until catastrophic failure of the optical fiber. The reflection spectrum at the failure of the optical fiber showed significant broadening and multiple peaks. However, it was noted that remaining below the endurance strain limit prevented damage to the FBG sensor and its reflection spectrum regardless of the number of load cycles. Theoretically, the sensor should be able to sustain millions of load cycles over many years without any residual damage or signal deterioration.

Despite the fact that the strain limit of FBG sensors has been explored, it was tested for an uncoated, surface-mounted sensor and is the opposite of the application of the FBG sensors used in this thesis. Furthermore, the method of mechanically or chemically stripping the coating from the FBG sensor results in cracking in the optical fiber and a reduction of its strength. In the work to come, coated FBG sensors are embedded in composite specimens and it will be essential to explore the strain limit of the sensors in this scenario.

Another scenario in which an FBG sensor could fail is when the composite in which it is embedded in is subjected to impact damage. Repeated impacts near an embedded FBG sensor have been shown to cause spectrum broadening [38], although this is not an absolute indicator of when or if the sensor will eventually fail. It is likely that repeated impacts directly centered on the optical fiber transmitting light to the sensor could cause a deformation or deterioration in the signal or complete loss of signal due to splitting of the fiber. With the gauge length of the sensor being the most fragile part of the embedded sensor, a single direct impact to it of sufficient energy will cause both a loss of intensity and broadening of the reflection spectrum [46]. The potential for sensor failure when subjected to repeated impacts designed to cause visible external damage to the composite is worth investigating further.

The Effect of Delamination Damage on the Reflection Spectrum

One excellent use of embedded FBG sensors is in the detection of delamination damage in composite laminates. Delamination damage is an often occurring failure mechanism in composites because it can grow between plies or from an edge and is prevalent under many types of loading including impact, fatigue, and various bending modes. To internally monitor for this type of damage, FBG sensors are embedded in locations near which delamination is likely to occur. In situations where the delamination results in stable crack propagation, the growth of the crack tip will result in a non-uniform strain across the FBG sensor's gauge length. Thus, the broadening of the spectrum that occurs can be used as an indication of damage detection and as a method to approximate delamination length.

As soon as a propagating crack exits the gauge length of the sensor, the reflection spectrum returns to the narrow, single peak form with a slight shift in peak wavelength assuming the now debonded region it is contained in is still under stress. Problems arise in scenarios in which the crack propagation is not stable and travels across the gauge length of the sensor almost instantaneously. Due to the low frequency of the full-spectrum interrogator, unstable crack propagation is problematic because the spectrum does not remain broadened for the adequate amount of time for detection. Even after the crack 'jumps' across the gauge length, the peak wavelength shift acts as a poor indicator of damage detection because change in the peak wavelength is not exclusively caused by non-uniform strain.

The challenge in analyzing the reflection spectrum under non-uniform strain lies in properly quantifying it for monitoring purposes and identifying a parameter that can be related to damage presence, type, and size. Okabe et al. [31] found that the broadening of the spectrum increased as a function of transverse crack density and showed that the spectrum bandwidth at half of its maximum intensity could be used to determine the transverse crack density in real time. Takeda et al. [27, 32, 33] proposed a method of measuring the intensity ratio of the two peaks that appear in the spectrum when subjected to non-uniform strain as a way to measure delamination length. However, there are problems that can arise when using this method including an intermittent signal presence. Using this method for real-time damage monitoring is unreliable because it requires the presence of only two peaks in the reflection spectrum under non-uniform strain. This is not always the case, as the spectrum can display either a single peak or several peaks which would result in a faulty signal. The work in this thesis will focus on taking a simpler approach to relating the reflection spectrum to damage presence by investigating the peak wavelength, center wavelength, and bandwidth (Figure 3) as spectrum monitoring methods.

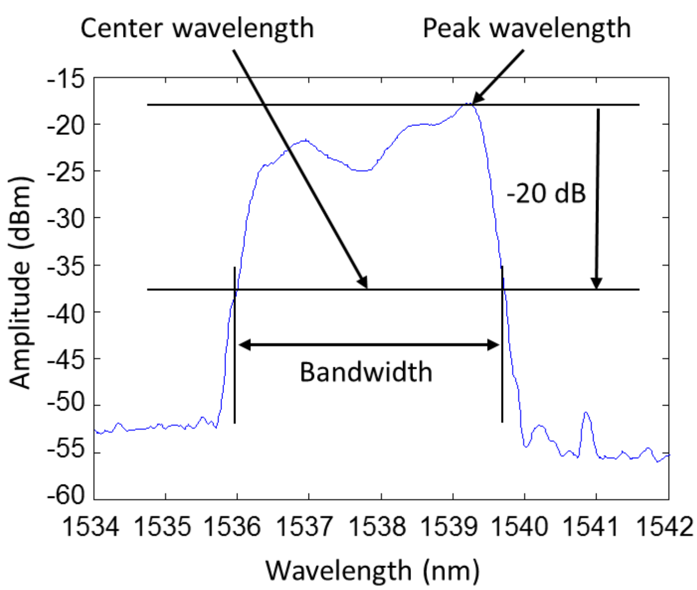

Figure 3. Peak wavelength, center wavelength, and -20 dB bandwidth of the reflection spectrum identified for spectrum monitoring purposes. For interpretation of the references to color in this and all other figures, the reader is referred to the electronic version of this thesis.

An efficient method for further exploring how the reflection spectrum will react to non-uniform strain is through the use of a numerical analysis of an FBG sensor by utilizing a transfer matrix formulation.

The Transfer Matrix Method

It is possible to design a numerical analysis to predict the effect of non-uniform strain on the reflection spectrum and investigate the ability to determine the actual strain distribution of a specimen with embedded FBG sensors by using the Transfer Matrix Method (TMM). Formulated by Yamada and Sakuda [47], it allows for the creation of a reflection spectrum based on a user-input strain distribution. It is often used for verification purposes where experimental reflection spectra obtained from an FBG sensor embedded in a composite specimen are compared with simulated reflection spectra produced using the TMM [27, 48, 49]. The matching of simulated and experimental spectral responses in this manner allows for the determination of the associated strain distribution [50-52]. If the produced reflection spectra are similar, the strain distribution used in the numerical analysis can be assumed to be the strain distribution in the specimen.

An additional benefit of a numerical analysis of an FBG sensor subjected to non-uniform strain is the ability to produce many reflection spectra for an investigation of spectrum monitoring methods without wasting FBG sensors in physical experiments. An optimal spectrum monitoring method can be determined through this method and experiments with FBG sensors embedded in composite laminates will only be necessary for a validation of the chosen method for monitoring damage.

Design of a Smart Composite Panel

While the TMM allows for a better understanding of the behavior of FBG sensors when subjected to non-uniform strain, this knowledge can be extended to more complex experiments in which large-scale panels that are more representative of realistic applications are tested.

The term ‘smart composite panel’ can be used to refer to any panel with at least one embedded sensor that allows it to diagnose its own structural health by monitoring and detecting damage. In this thesis, it will be used to specifically refer to large-scale, thick-section composite panels with multiple embedded FBG sensors. The goal in creating a smart composite panel is to utilize multiple FBG sensors throughout its area or surface that can guarantee the detection of damage without the prior knowledge of where it will occur.

Large-scale self-diagnostic composite structures are highly desirable in applications where impact damage is experienced. The occurrence of a dynamic impact event can cause significant damage to a composite structure in a short amount of time and quick detection is crucial in preventing catastrophic failure. Composite panels have even been designed to self-heal by restoring compressive strength after detecting impact damage with a vascular network carrying an epoxy resin system [53] and shape memory alloy wires [54]. Hence, a smart composite panel’s ability to effectively self-diagnose becomes even more important.

A dynamic impact event can be instantaneously detected with an embedded FBG sensor when a high frequency (>200 kHz) interrogator is used and is indicated by a jump in signal that occurs within a matter of milliseconds before the signal returns to its initial value. A low frequency (<200 kHz) interrogator may be used only if the composite specimen or structure is repeatedly impacted at the same point in a manner that causes the edge of propagating damage to slowly travel across the gauge length of the FBG sensor as the number of impacts increases. In this case, the peak wavelength would shift and the spectrum would broaden allowing an increase of the full width at half-maximum to serve as a damage indicator [38]. However, if the impact were great enough that the damage encompassed the gauge length of the sensor after a single impact, it would be tough to determine from the reflection spectrum if damage had been sustained.

A low frequency interrogator (<100 Hz) presents a significant challenge in detecting impact damage with FBG sensors. Low frequency interrogators are significantly less expensive than high frequency units, although they are incapable of measuring a dynamic impact event because of the speed at which it occurs. One potential method for solving this problem is periodically introducing strain to the embedded FBG sensors through bending of the composite structure based on the theory that the sensors will measure significantly higher strain values if damage has occurred due to the resulting increased compliance. In one instance, compressive loading was employed to detect impact damage in a large composite panel with embedded FBG sensors long after it had occurred [46], although the panel was destroyed in the process. For structural health monitoring purposes with realistic applications in mind, this method must be tweaked to detect impact damage while remaining in the linear-elastic range of the panel.

Efforts have been made in determining the location of impact with time-of-flight measurements by three surface-mounted FBG sensors of the Lamb waves that propagate through a structure when impact occurs [54]. The impacts were located using an iterative algorithm implemented in MATLAB based on work by Jeong and Jang [55]. However, the surface mounting of the FBG sensors makes them vulnerable to impact damage. For structural health monitoring applications in which impact could occur at any random location on the panel, it will be necessary to explore alternatives. The work to come will find a solution in which impact damage can be located using embedded FBG sensors so that the survival of the sensors is assured.

CHAPTER 3
DURABILITY TESTING OF EMBEDDED FBG SENSORS

Introduction

The durability of embedded FBG sensors subject to impact and tensile loading is a concern that must be addressed to ensure that the sensor's ability to monitor structural health is not lost during service. The failure of a sensor embedded in a composite structure would likely result in a blind spot in a high-probability failure area without the ability to repair the sensor and re-gain a signal. The significant drawback of embedded FBG sensors in composite structures is that the sensors are contained within the structure itself rather than on the surface and become immovable and unreachable after material curing. Although, this single negative aspect is of little consequence compared to the potential benefits of self-diagnostic composites.

FBG Sensor Strain Limit

FBG sensors obtained from commercial manufacturers will typically come with a prescribed strain limit. This prescribed strain limit is a value beyond which the manufacturer deems data retrieved using the FBG sensor as unreliable. It is not explicitly stated that this strain limit is the point at which the sensor will fail although it is recommended that it not be exceeded.

Previous Work

Extensive work has been done using FBG sensors to detect both crack propagation in specimens subjected to multiple bending modes and damage in specimen subjected to dynamic impact loading. However, little work has actually been done on pushing FBG sensors to their limits in these applications to determine the extent of damage the sensors can withstand without failing and the residual effects of loading beyond the sensor's strain limit. Ang et al. [45]

examined similar situations by attaching an uncoated FBG sensor to the surface of a composite subjected to four-point bending. Their work found that the sensor failed at approximately 6000 $\mu\varepsilon$ and had an apparent endurance strain limit above which the reflection spectrum deteriorated. While the sensors used in these tests failed at 6000 $\mu\varepsilon$, there is no information given on the value of the manufacturer's prescribed strain limit. Additionally, the methods used to strip the coating of the sensor by mechanical and chemical means left scratches and cracks on the uncoated fiber that reduced the durability of the sensor and initiated failure.

The FBG sensors investigated in this chapter have a protective polyimide coating and a prescribed strain limit, specified as 5000 $\mu\varepsilon$, and it is necessary to perform tests that further explore the consequences of exceeding this point to determine if there is a strain at which the embedded sensors fail before the composite material.

Objectives

This work aims to address sensor durability issues through two simple yet effective experiments aimed at providing concrete information about the survivability of FBG sensors embedded in a glass/epoxy composite specimen. The prescribed 5000 $\mu\varepsilon$ limit of the FBG sensors will be investigated through a uni-axial tension test while the survivability of the sensors will be scrutinized through a drop-weight impact test. The goal of these tests is to verify sensor durability and their ability to maintain functionality after damage has occurred.

Manufacturing of Composite Specimen

A thin unidirectional glass/epoxy composite specimen of approximately 152.4 x 25.4 x 1.75 mm^3 made using a hand lay-up process of pre-preg sheets (Cycom 1003) and cured in a hot oven press was used in this experiment. During the hand lay-up process, an FBG sensor (Micron

Optics os1100) with a 10 mm gauge length was embedded between the fourth and fifth plies of the 8-ply specimen. The positioning of the sensor is shown in Figure 4. The optical fiber was embedded parallel to the fiber direction in the composite.

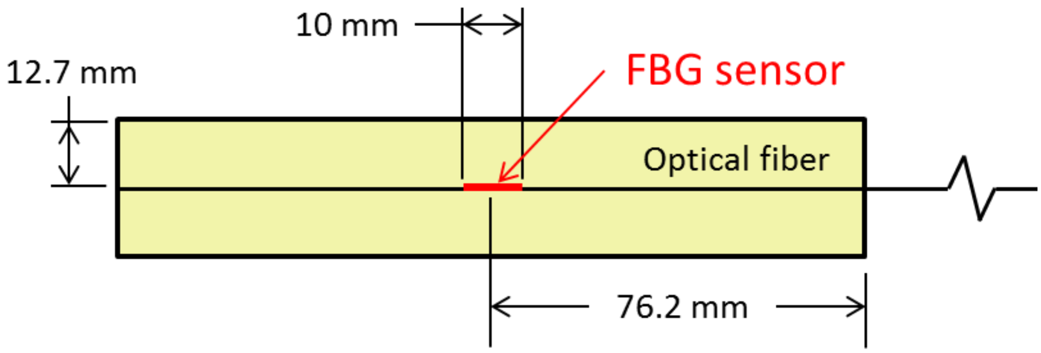

Figure 4. Glass-fiber epoxy specimen with embedded FBG sensor

Uni-Axial Tension Test

A static uni-axial tension test was performed on the specimen using a MTS 793 uni-axial testing machine. Thick composite tabs covered with sandpaper were attached at the ends to absorb the gripping force, prevent slipping between the specimen and the grip, and prevent unwanted compression on the embedded optical fiber. The tabs also prevented failure of the specimen near the gripped ends and allowed for catastrophic failure in the fiber direction. The uni-axial tension test specimen with an embedded FBG sensor is shown in Figure 5.

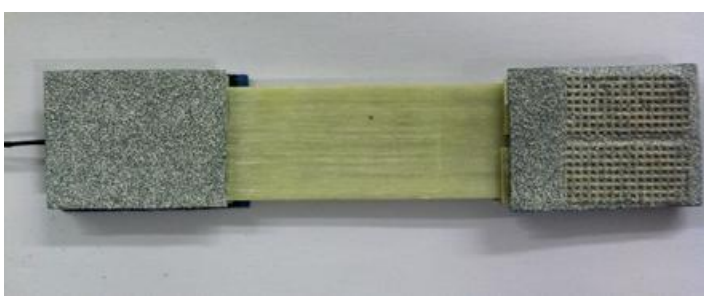

Figure 5. The uni-axial tension test specimen with an embedded FBG sensor

A laser extensometer (Electronic Instrument Research Model LE-05) with a 10 mm gauge length and clip extensometer (MTS Model 632.11B-20) with a one inch gauge length were employed to measure the strain experienced by the embedded FBG sensor during loading and the data was recorded using the MTS Station Manager software. An Optical Sensing Interrogator (Micron Optics sm-125) and Micron Optics ENLIGHT software were used to record the reflection spectrum of the FBG sensor. The experimental set-up is shown in Figure 6.

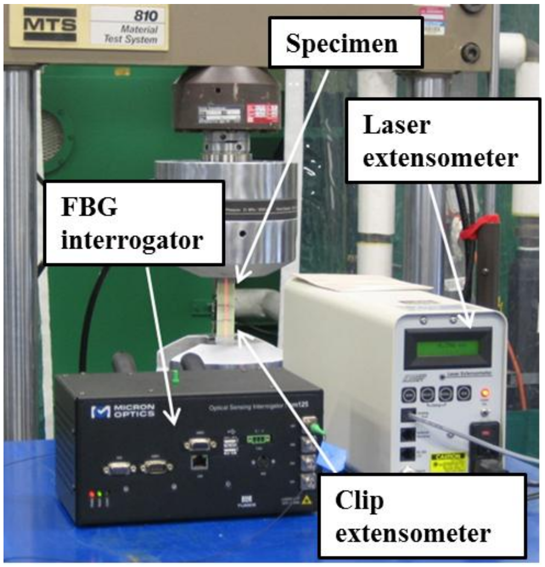

Figure 6. Static uni-axial tension test experimental set-up

The time history of load applied to the specimen is shown in Figure 7. The specimen was subjected to two loading cycles to investigate the effect of exceeding the FBG sensor's strain limit on the reflection spectrum.

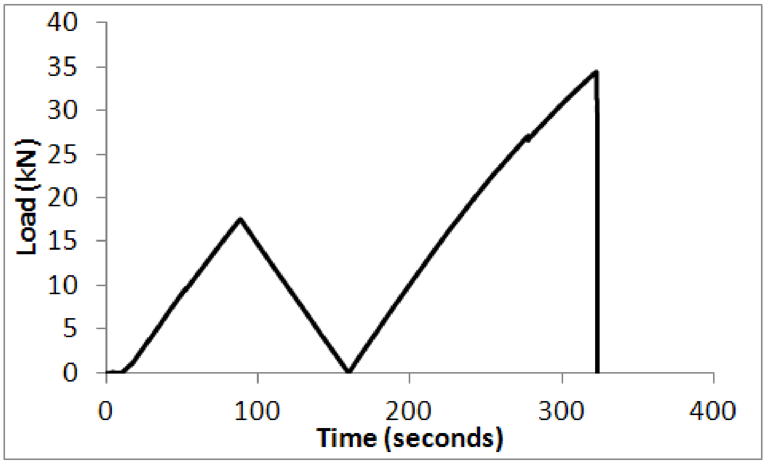

Figure 7. Time history of load applied to specimen

The slight notch at approximately 275 seconds marks the initial breakage along the fiber direction of the specimen and breakage continued until failure. The specimen experienced catastrophic failure at approximately 325 seconds. At this point, the composite split along the fiber direction and the test was stopped. The specimen after failure with breakage along the fiber direction is shown in Figure 8.

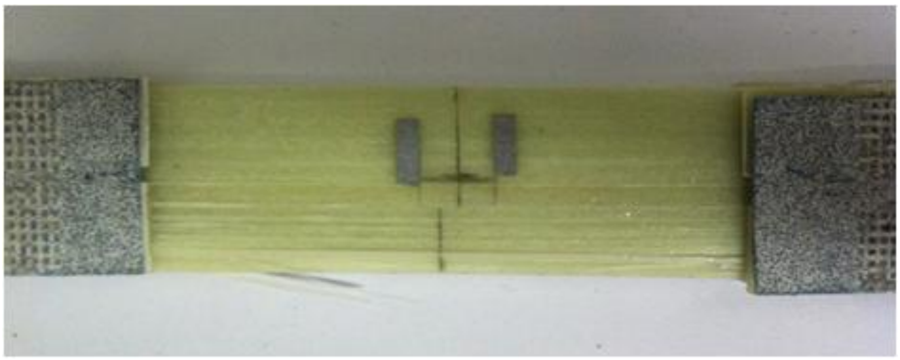

Figure 8. Uni-axial tension test specimen after failure

Impact Damage Test

Thin glass-fiber epoxy specimens made using a hand lay-up process of pre-preg sheets and cured in a hot press of approximately 152.4 x 25.4 x 1.75 mm^3 were used in this experiment. During the hand lay-up process, an FBG sensor was embedded in each specimen parallel to the fiber direction. Each specimen was impacted using the drop weight impact tower shown in Figure 9. The drop weight impact tower utilized a rounded-tip impactor with a quarter-inch radius and a drop weight of 4.59 kg. The specimen and an aluminum backing plate were clamped in a metal fixture composed of two rectangular metal frames held together with screws.

Each specimen was impacted at least five times with an impact energy of 10 J at a single location a different distance away from the center of the gauge length of the FBG sensor. Impact locations included the center of the gauge length, 5 mm from the center of the gauge length (edge of the gauge length), and 10 mm from the center of the gauge length. The impact locations and specimen configuration are shown in Figure 10. The ply locations of the embedded sensors and specimen lay-up are given in Table 1.

The reflection spectrum of the embedded FBG sensor was recorded prior to impact using a Micron Optics Optical Sensing Interrogator (sm-125). During the impact event, the signal voltage was measured using a Redondo Optics FBG-Transceiver (M600) capable of dynamic strain measurement due to its 320 kHz scanning frequency. After each of the five impacts, the reflection spectrum was again recorded using the Micron Optics interrogator.

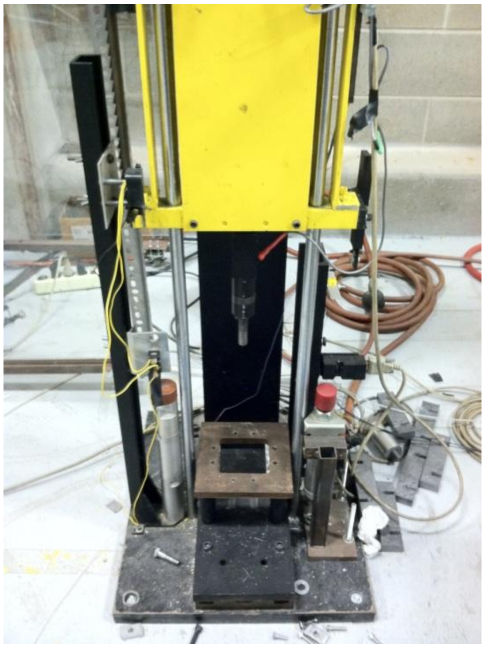

Figure 9. Drop weight impact tower

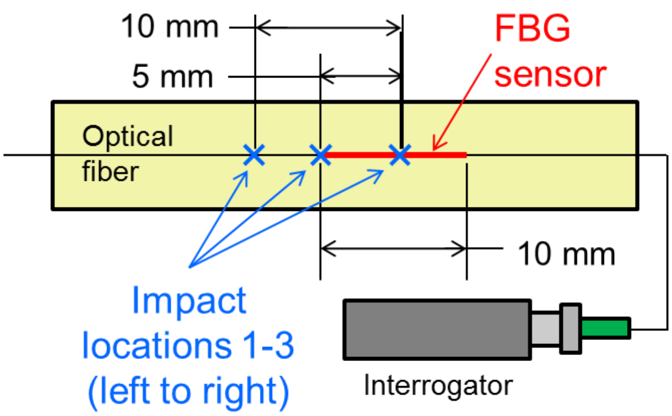

Figure 10. Impact locations and specimen configuration (not to scale)

Table 1. Ply locations of the embedded sensors and specimen lay-up configuration

Impact location	Layup (from bottom to top)
10 mm from center of gauge length (Impact location 1)	$[0°]_6$/[FBG]/ $[0°]_2$
5 mm from center of gauge length (Impact location 2)	$[0°]_2$/[FBG]/ $[0°]_6$
Center of gauge length (Impact location 3)	$[0°]_6$/[FBG]/ $[0°]_2$

Consequences of Exceeding the Strain Limit

The time history of strain measured using the laser and clip extensometers during tensile testing and FBG sensor strain limit are shown in Figure 11. The first loading cycle is designed to load the specimen to 10,000 με, or twice the prescribed strain limit. The specimen is then unloaded to zero and pulled to composite failure.

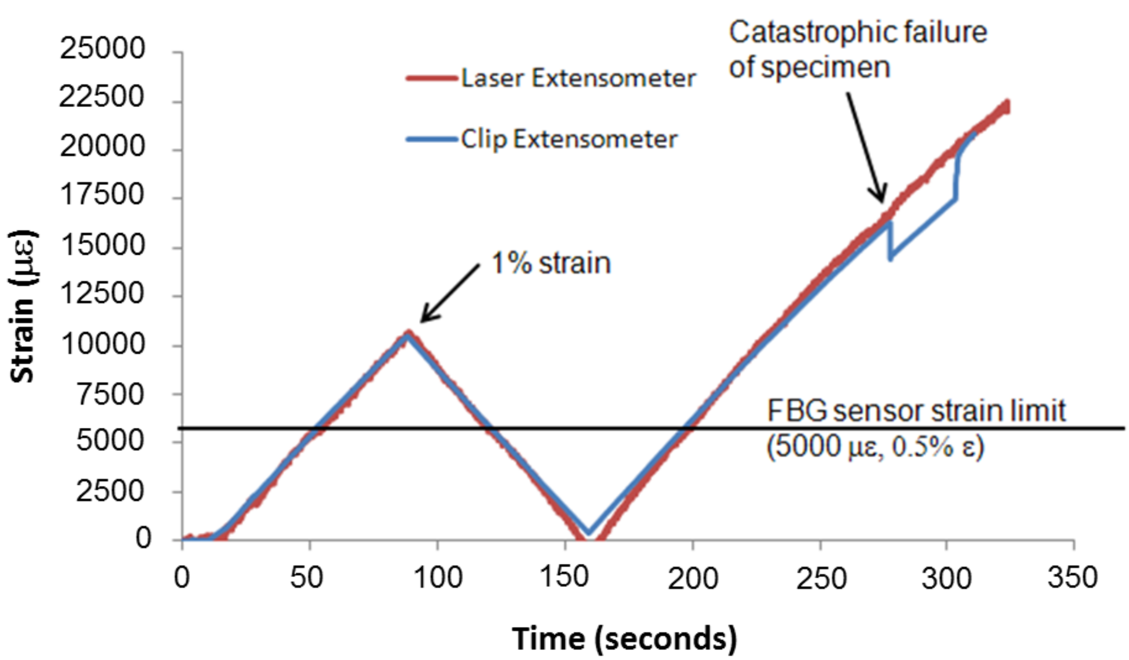

Figure 11. Time history of strain measured using the laser and clip extensometers during tensile testing and FBG sensor strain limit

Critical points must be identified in the time history of measured strain to investigate the behavior of the FBG sensor beyond the strain limit. Five critical points have been identified in Figure 12.

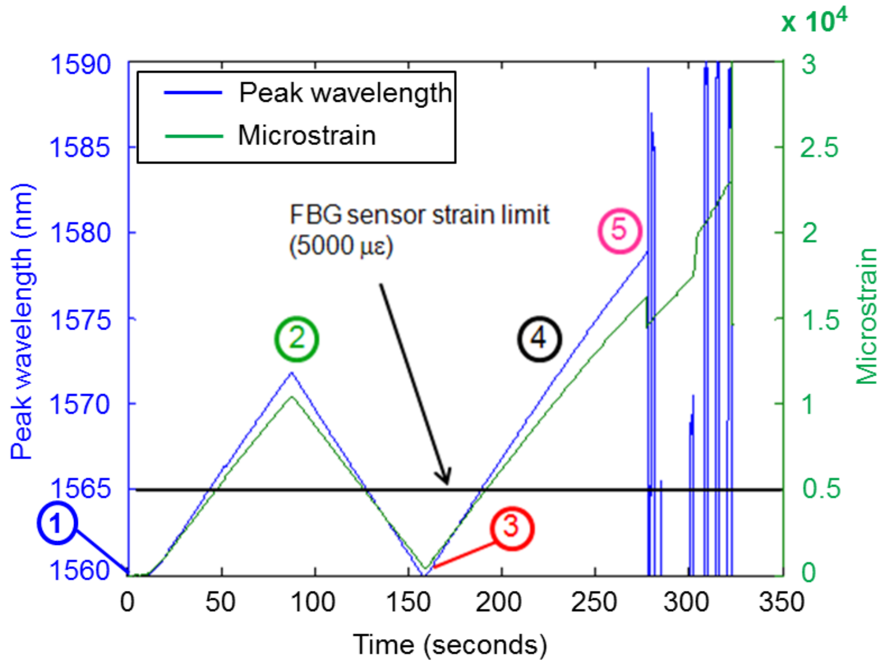

Figure 12. Critical points during tensile testing

Critical points 1 and 3 provide a comparison at zero strain before and after exceeding the FBG sensor's strain limit. Points 2 and 4 provide a comparison between the first and second loading cycles at 10,000 με. Point 5 provides a checkpoint to determine if the FBG sensor is active just after catastrophic failure of the composite specimen.

The reflection spectra of normalized intensity for the critical points marked in Figure 12 are presented in Figure 13. The colors correspond to the color of the critical point marker and the reflection spectra are further identified by the time at which they are obtained. Comparing the reflection spectra obtained at points 1 and 3 shows there is a significant intensity reduction of approximately 65%. This demonstrates that exceeding the FBG sensor's strain limit will indeed have an effect on the reflection spectrum. Comparing the reflection spectra obtained at points 2 and 4 shows an intensity reduction of approximately 10%. This demonstrates that multiple passes above the strain limit cause a further reduction of spectrum intensity.

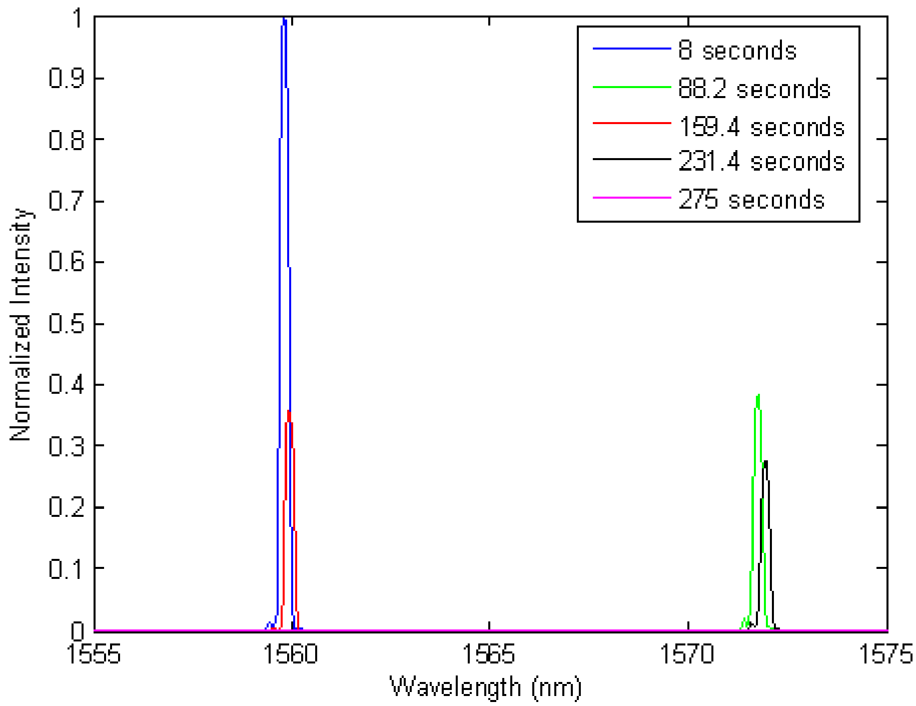

Figure 13. Reflection spectra of normalized intensity for the critical points marked in Figure 12

An investigation of the reflection spectrum at point 5 results in a signal with zero intensity. At this point, the sensor has been damaged and is no longer capable of reporting data. However, the sensor has been active up until this point, confirmed by the presence of a spectrum at point 4, and has successfully remained active until catastrophic failure despite being strained far beyond the strain limit.

The survivability of the sensor is further confirmed by monitoring the peak wavelength, center wavelength, and spectral bandwidth during tensile testing as plotted in Figure 14. The measurements of all spectrum quantification methods remain reliable until catastrophic failure of the specimen occurs at a time of approximately 275 seconds and the signals become erratic.

While monitoring the peak and center wavelength will do little more than identify the point at which the FBG sensor breaks, monitoring the spectral bandwidth during loading of the specimen may serve an additional purpose. The small jump in width that occurs during high strain and prior to failure can act as a rough indication of when the sensor has exceeded the strain limit. The benefit of monitoring the spectral bandwidth is that the value remains constant during loading and unloading of the specimen.

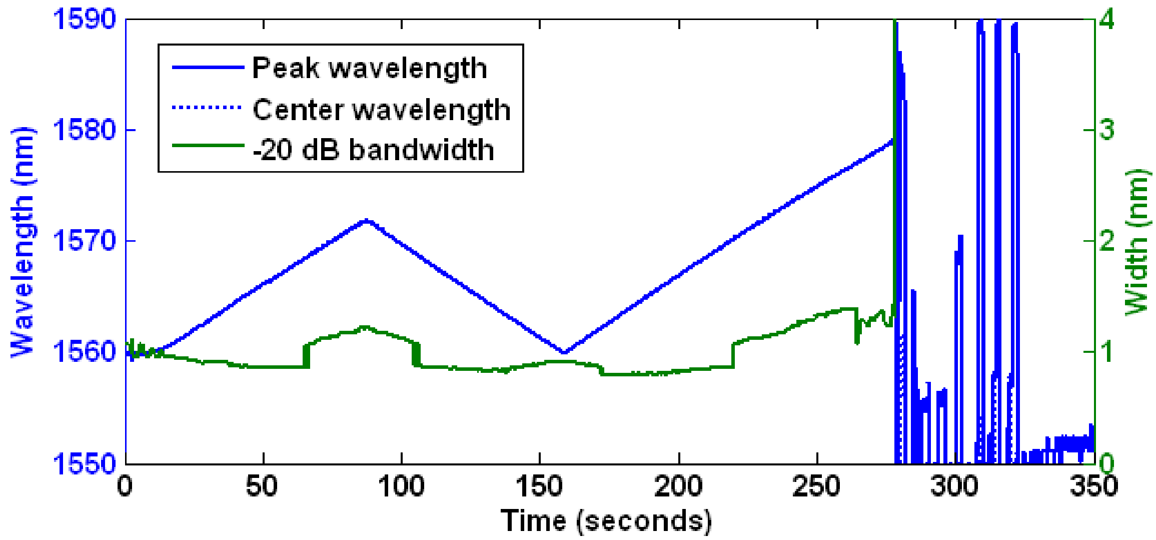

Figure 14. Time history of peak wavelength, center wavelength, and spectral bandwidth during tensile testing

Effect of Impact on the Reflection Spectrum

The reflection spectrum before any impact damage and the reflection spectrum after the fifth and final impact for the specimen at an impact location of 10 mm from the center of gauge length are compared in Figure 15. Most importantly, the results demonstrate that the FBG sensor survives all five impacts and remains capable of reporting a reflection spectrum. While the reflection spectrum after the final impact has broadened and shows an increased amount of noise near the peak, it remains sensitive to strain. The spectrum broadening is most likely directly related to the proximity of the embedded FBG sensor to the specimen's surface. The sensor's embedding position of a +6 ply location means that there are only two plies between it and the impact surface. The FBG sensor is demonstrating the consequences of experiencing both external damage from the impactor's force on the specimen's surface and internal damage caused by absorbed impact energy.

The reflection spectrum before any impact damage and the reflection spectrum after the fifth and final impact for the specimen at an impact location of 5 mm from the center of gauge length are compared in Figure 16. Again, the results show that the sensor survives the impact testing and continues to return a reflection spectrum that is nearly identical to the initial reflection spectrum. The smaller change between these spectra and the spectra shown previously in Figure 15 is due to the embedding position of the FBG sensors. The reflection spectra for the previous specimen impacted 10 mm from the center of the gauge length had its FBG sensor embedded at a +6 ply location while this specimen had its FBG sensor embedded at a +2 ply location, meaning there are six plies between the FBG sensor and the impact surface. The embedding location and the FBG sensor's proximity to the impact surface appears to have more effect on the broadening of the signal than the impact location relative to the center of the sensor's gauge length.

The reflection spectrum before any impact damage and the reflection spectrum after the seventh and final impact for the specimen at an impact location at the center of the gauge length are compared in Figure 17. This specimen was impacted an additional two times in an effort to establish how many impacts the embedded FBG sensor could survive and still return a reliable reflection spectrum. It was determined that after approximately six impacts, the reflection spectrum broadened and its intensity deteriorated in a way that it was no longer effective in measuring strain and was ruled catastrophically damaged. This scenario subjects the FBG sensor to the most damage per impact based on the impact location and its embedding position and it is for this reason that this case was tested to complete failure of the FBG sensor.

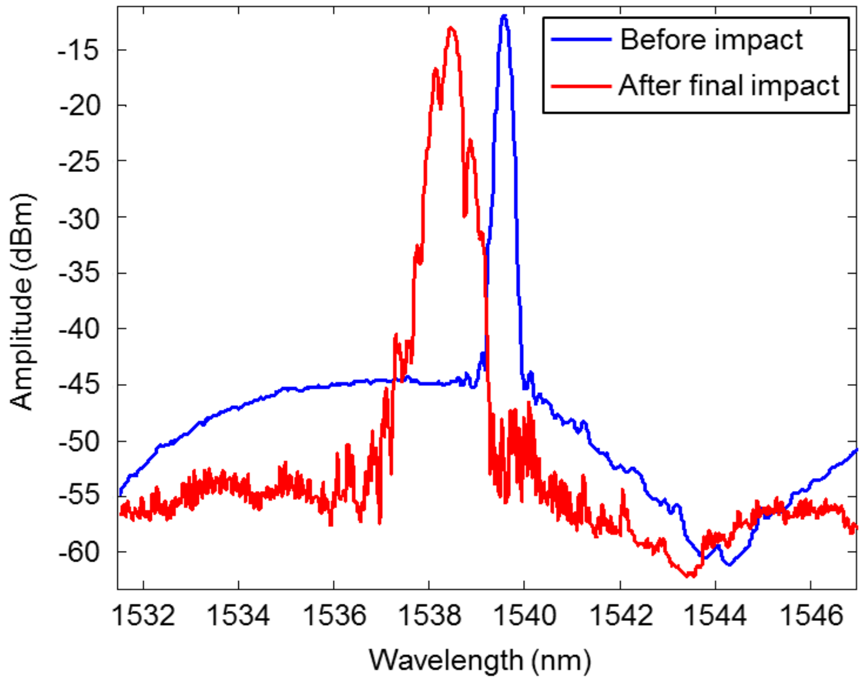

Figure 15. The reflection spectrum before any impact damage and the reflection spectrum after the fifth and final impact for the specimen with an impact location at 10 mm from the center of gauge length (impact location 1)

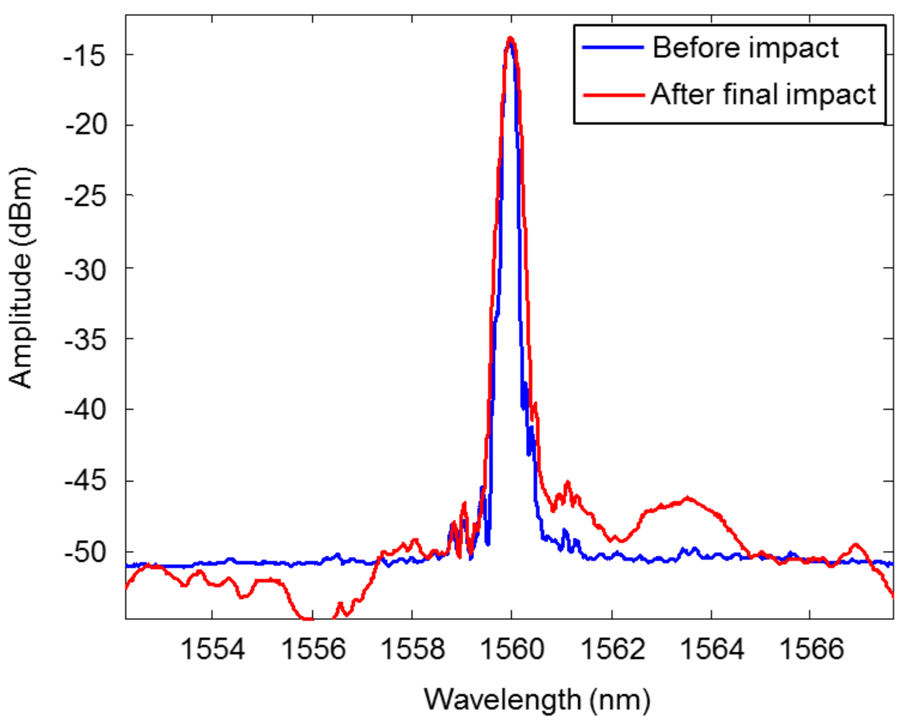

Figure 16. The reflection spectrum before any impact damage and the reflection spectrum after the fifth and final impact for the specimen with an impact location at 5 mm from the center of gauge length (impact location 2)

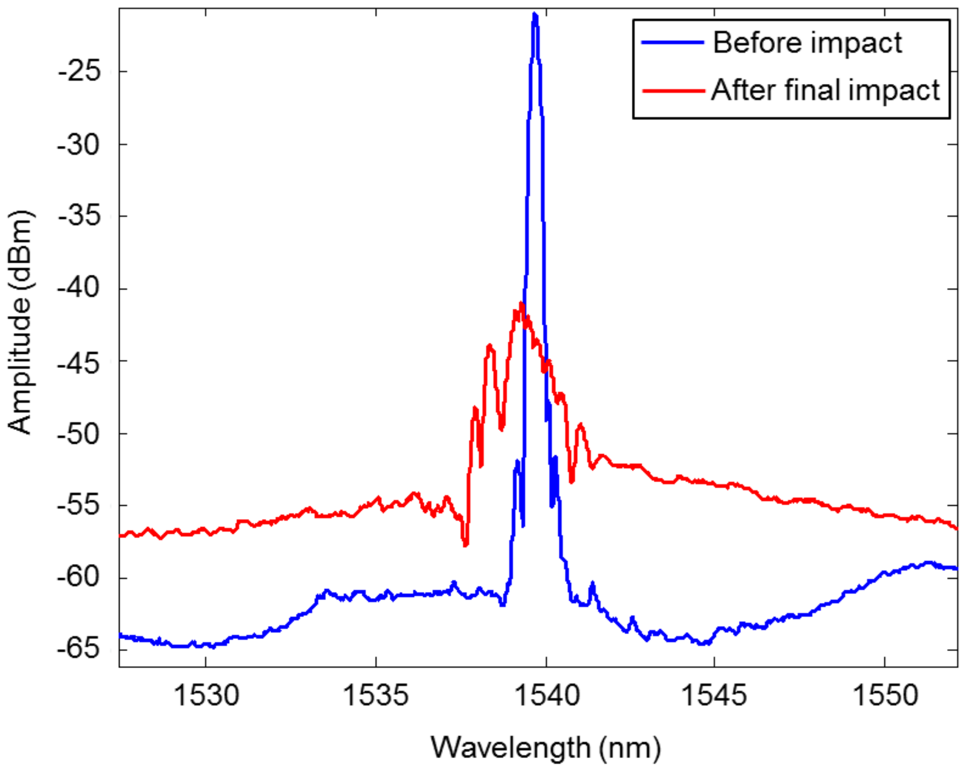

Figure 17. The reflection spectrum before any impact damage and the reflection spectrum after the seventh and final impact for the specimen with an impact location at the center of gauge length (impact location 3)

The reflection spectra at incremental number of impacts at the center of the FBG sensor's gauge length (impact location 3) are shown in Figure 18. The transition from a narrow, single-peak reflection spectrum with high amplitude to a broad, multi-peak reflection spectrum with low amplitude as the number of impacts increases is illustrated. As previously demonstrated, it takes a significant number of impacts at the same location to wear down the signal strength of the embedded FBG sensor.

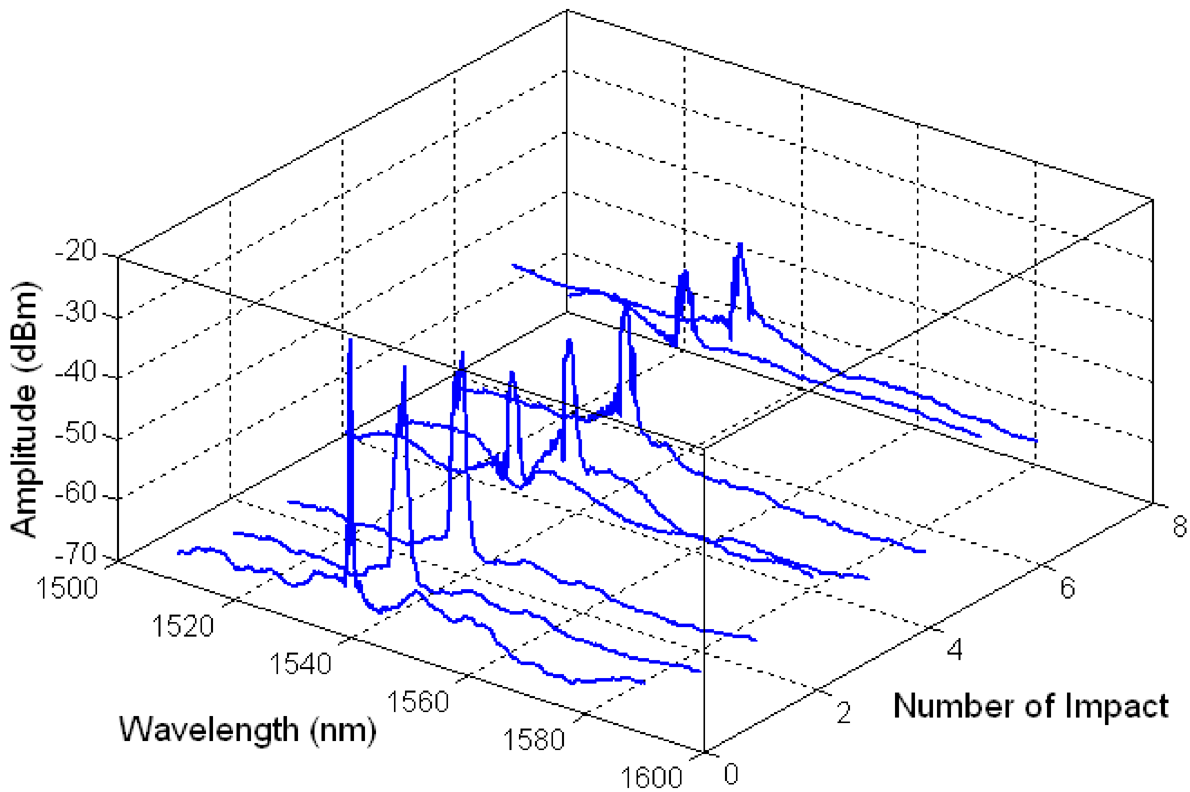

Figure 18. Reflection spectra at incremental number of impacts at the center of the FBG sensor's gauge length (impact location 3)

Findings

It has been demonstrated that embedded FBG sensors are extremely reliable and capable of withstanding amounts of strain exceeding the manufacturer's prescribed limit without failing. The embedded FBG sensor subjected to static loading remained intact and functional until the composite failed. However, it was found that exceeding the strain limit resulted in a residual effect on the sensor's signal that caused the signal's intensity to deteriorate upon reloading of the specimen.

An FBG sensor embedded in a thin composite laminate has been shown to be resistant to failure when subjected to impact near its embedding location. Impacts that occurred at the center of the gauge length of the sensor caused the reflection spectrum to broaden and drop in intensity at a rate much faster than other impact locations. However, it required at least seven impacts at the most vulnerable location to produce this effect and the endurance of the sensor to this extent is impressive.

Ultimately, the sensors have been proven capable of surviving for the entire life of a specimen subjected to static loading or impact. Having established the great survivability of embedded FBG sensors for structural health monitoring purposes, it is safe to further explore the development of self-diagnostic composites using these sensors.

CHAPTER 4
BASELINE TESTING OF COMPOSITE SPECIMENS

Introduction

The experiments performed in this chapter will simulate delamination in a composite structure by creating a propagating crack in a small composite specimen through Mode-I and Mode-II bending. The experiments will be a trial run before testing specimens with embedded FBG sensors to ensure that the tests are repeatable and that stable crack propagation can be achieved. Stable crack propagation is required due to the low scanning frequency of the FBG interrogator used to record the signal of an embedded FBG sensor. It will give the interrogator ample time to record the change in the reflection spectrum as the crack slowly propagates along the gauge length of the FBG sensor.

The use of dummy specimen in these experiments will reduce the number of FBG sensors required to obtain sufficient results in later testing. Once stable crack propagation is achieved, the tests will be repeated with an FBG sensor embedded in the specimen in Chapter 6 to validate the structural health monitoring capabilities of FBG sensors.

The first experiment performed uses a double cantilever beam (DCB) specimen subjected to Mode-I bending in which a slowly propagating crack is grown along the mid-plane of the specimen. The procedure is based on ASTM D 5528 [60] and is modified to allow for the tracking of crack propagation at approximately ten second intervals using a CCD camera. The second experiment uses the same specimen and subjects it to Mode-II bending to facilitate shear loading. Because there is no ASTM Standard for this type of bending, the ability to grow a stable crack in this configuration is uncertain.

The experiments carried out also allowed for the calculation of the Mode-I and Mode-II fracture toughness. These values are not provided by the composite's manufacturer and will be beneficial to add to the material properties list of the glass/epoxy unidirectional composite (Cycom 1003) used in these tests.

Mode-I and Mode-II Fracture Toughness

Sanford [61] defines a measure of tracking the ability of a crack to grow in a geometry, the strain energy release rate, G, as the spatial rate of change of stored strain energy under system isolated conditions. It is defined numerically as,

$$G = -\left.\frac{\partial U}{\partial A}\right|_{\delta} \tag{5}$$

where U is the strain energy of the system, and the negative sign produces a positive quantity. Under linear-elastic conditions, the strain energy of the system can be written as,

$$U = \frac{1}{2} P\delta \tag{6}$$

and

$$\delta = CP \tag{7}$$

where P is the applied load, d is the deflection, and C, the compliance, is the reciprocal of the slope of the load-deflection line. By replacing the deflection in Eq. (6) with Eq. (7) and differentiating with respect to A, it follows that

$$G = \frac{P^2}{2}\frac{\partial C}{\partial A} \tag{8}$$

It is important to note that this equation derived for the strain energy release rate is independent of specimen dimensions and can therefore be applied to any geometry through a compliance calibration method. Sanford specifies that assuming the crack length, *a*, is short compared to the overall length of the specimen, the undamaged portion of the specimen can be treated as the rigid support for the double cantilever beams formed by the crack and from elementary beam theory the deflection of the beams is given as,

$$\delta = \frac{2Pa^3}{3EI} \tag{9}$$

and

$$I = \frac{Bh^3}{12} \tag{10}$$

where B is the width of the specimen and h is half the thickness of the specimen. Based on Eq. (8), (9), and (10), the strain energy release rate of the DCB specimen can be written as,

$$G = \frac{P^2}{2}\frac{\partial C}{\partial A} = \frac{P^2 a^2}{BI} \tag{11}$$

The experiment used four different methods to calculate the fracture toughness of the composite material as stipulated by ASTM D 5528. The first equation, known as the Modified Beam Theory, is given as,

$$G_I = \frac{3P\delta}{2ba} \tag{12}$$

where δ is the load point displacement, b is the specimen width, and a is the delamination length. The ASTM Standard simplifies Eq. (11) to Eq. (12) for cases in which the load and deflection can be measured at the point of delamination. To account for the rotation at the delamination front caused by the piano hinges, a correction factor, Δ, is introduced. This factor can be determined using a least squares plot of the cubed root of compliance, $C^{1/3}$, versus delamination length. The compliance is calculated as the ratio of load point displacement to applied load, δ/P. The corrected equation, referred to as the Corrected Modified Beam Theory, is defined as,

$$G_I = \frac{3P\delta}{2b(a+|\Delta|)} \tag{13}$$

The Compliance Calibration (CC) Method, introduced as Eq. (14), calculates fracture toughness using an alternative correction factor, *n*. The CC Method defines *n* as the slope of the best least-squares fit of the curve generated by a least squares plot of log (δ_i/P_i) versus log (a_i).

$$G_I = \frac{nP\delta}{2ba} \tag{14}$$

The Modified Compliance Calibration (MCC) Method uses the correction factor A_1. A_1 is defined as the slope of the best least-squares fit of the curve generated by a least squares plot of *(a/h)* versus cubed root of compliance, $C^{1/3}$, where *h* is the specimen thickness.

$$G_I = \frac{3P^2C^{2/3}}{2A_1bh} \tag{15}$$

To arrive at an equation to calculate the Mode-II fracture toughness, a method similar to that used to derive Eq. (11) is used. Chatterjee [62] specifies the Mode II strain energy release rate as,

$$G_{II} = \frac{9}{2}\frac{P^2(a+\alpha h)^2}{E_{11}b^2h^3} \tag{16}$$

where *a* in Eq. (11) has been replaced with $(a + \alpha h)$ and

$$\alpha = 0.13\sqrt{\frac{E_{11}}{G_{13}}} \tag{17}$$

where G_{13} is the through thickness shear modulus and E_{11} is the axial Young's Modulus.

Mode-I Bending Test

A panel of Cycom 1003, a unidirectional glass/epoxy composite (E = 39.3 GPa), was manufactured using a hand lay-up technique and tetrahedral oven press for curing with an approximate thickness of 3 mm. During lay-up, a thin sheet of Teflon was inserted in the mid-plane of the composite approximately two inches deep from one end to initiate crack growth. Individual specimens were cut using a diamond saw to be approximately 25.4 x 152.4 mm^2.

The Mode-I bending experiment was done on an MTS uni-axial testing machine capable of measuring extension and load. Load versus extension data was recorded using TestWorks 4 software and saved for later analysis. The specimen was modified so that it could be loaded in a fashion similar to a double cantilever beam. Aluminum piano hinges were attached to the specimen on the Teflon-inserted end using a high-strength epoxy so that the specimen could be loaded into the testing machine and delaminated. The specimen was loaded at 5 mm/min as specified in ASTM D 5528. The final specimen is shown in Figure 19 with the necessary measurements prior to testing.

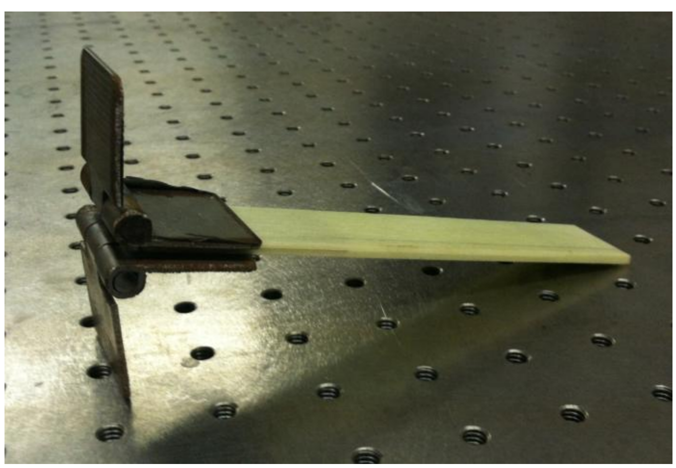

Figure 19. DCB Specimen with attached hinges

In order to track crack growth during testing, a mirror and camera were set up to record images of the flat side of the specimen at 10 second intervals. By illuminating the specimen with a lamp attached to the crosshead, the propagation of the crack could be tracked in the images. The setup of the experiment is shown in Figure 20.

The mirror side of the DCB specimen was marked at 10 mm intervals starting at the initial delamination length to aid in the tracking of crack growth as shown in Figure 21. The images were captured using ImageCapture 2.0 and analyzed using MATLAB. MATLAB aided in the location of the crack at 10 second intervals and this data was interpolated in Microsoft Excel to approximate delamination length at roughly one second intervals that matched up to the time recorded by TestWorks 4 corresponding to load and extension data.

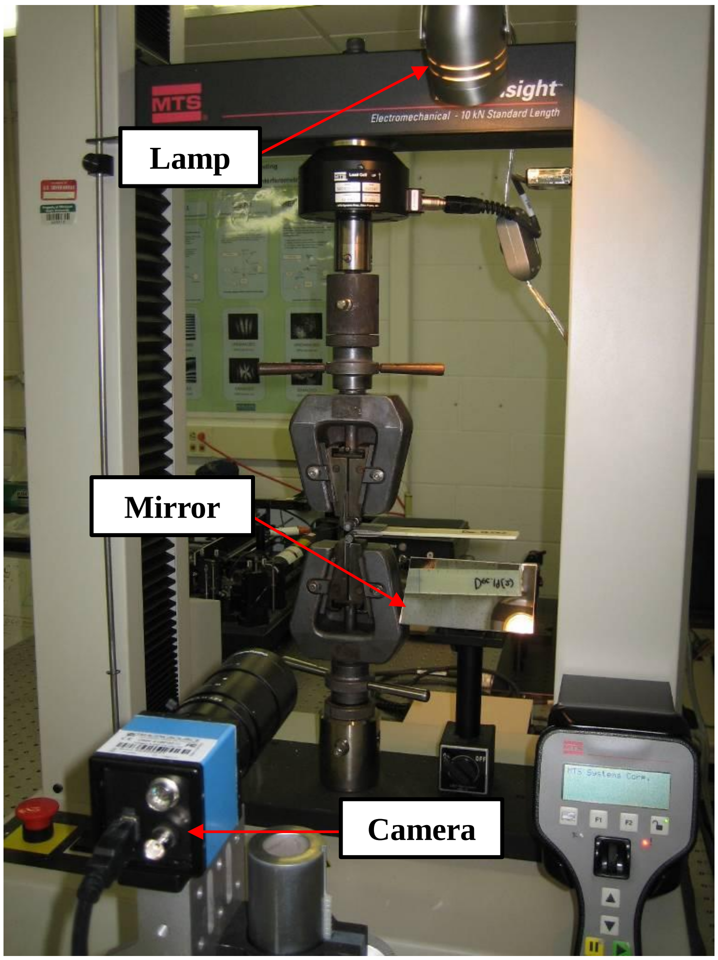

Figure 20. Experimental setup of Mode-I bending experiment

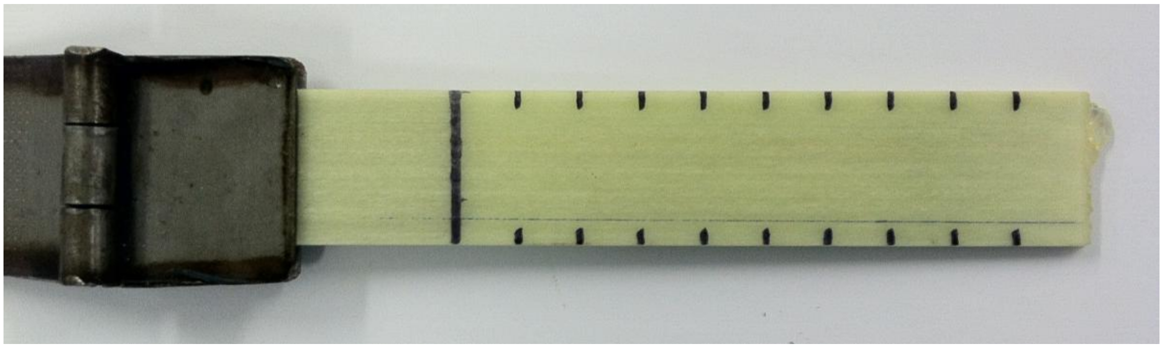

Figure 21. DCB specimen marked at 10 mm intervals

The Mode-I bending experiment was conducted with slight variation from ASTM D 5528. The ASTM Standard specified that an initial delamination length of 63.5 mm was optimal however the specimen used were manufactured with an initial delamination length of approximately 50.8 mm. The ASTM Standard dictated that once the piano hinges were applied, the distance from the initial delamination point to loading point, or pin of the piano hinges, should be approximately 50.8 mm. Because of this, the piano hinges had to be applied to the specimen in the opposite direction of how they are typically applied according to the ASTM Standard. This allowed for the specified distance between initial delamination point and loading point to be approximately 50.8 mm to comply with the ASTM Standard.

In addition to the modified piano hinges, the procedure in which the delamination length was tracked throughout the experiment was modified from the ASTM Standard specification. The ASTM Standard uses a procedure in which the delamination length is tracked with the naked eye using tick marks on the side of the specimen during testing and loading is paused to observe the corresponding load, displacement, and delamination length values. In order to make the measurement of delamination length more precise and allow for a continuous experiment, the mirror and digital camera were introduced to record images at ten second intervals during testing so the delamination could be measured digitally through MATLAB. This modified procedure allows for data points in excess of 700 compared to the 10 to 20 data points recorded with the ASTM Standard procedure. It is expected that this procedure eliminates human error from visually measuring the delamination length during testing as the tip of the crack is tough to locate from the side. By illuminating the specimen and instead tracking the crack from the flat side of the specimen, the crack tip can be easily located. A sample image from the set of images processed using MATLAB to locate the crack tip is shown in Figure 22.

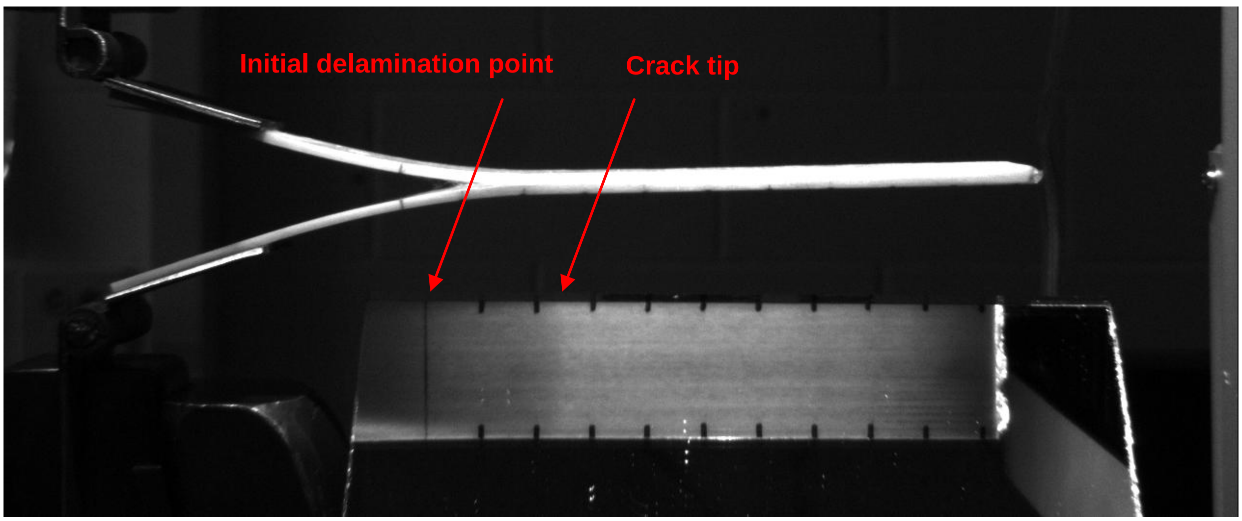

Figure 22. Sample image used to locate the crack tip

Mode-II Bending Test

The Mode-II bending experiment used the same testing machine and composite specimen as in the Mode-I bending test. The grips of the uni-axial testing machine were replaced with a three-point flexure test fixture outlined in ASTM D 790 [63] and the setup can be seen in Figure 23. The specimen was supported on the bottom by two rolling pins and loaded at the mid-span by a third rolling pin and loaded at 2 mm/min. The compression force applied caused a shearing load at the mid-plane of the specimen and initiated crack propagation.

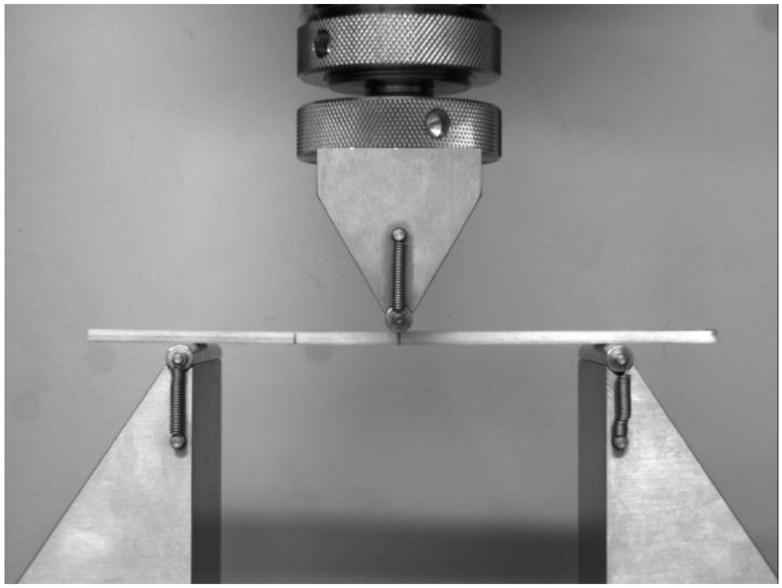

Figure 23. Experimental setup of Mode-II bending experiment

The end notched flexure (ENF) specimen used and the critical dimensions are shown in Figure 24. Initial specimens were manufactured with an *a/L* ratio of 0.5, however it became necessary to manufacture additional specimens with an a/L ratio of 0.75 for reasons that will be later explained. Overall dimensions of the specimens were approximately 25.4 x 152.4 mm^2.

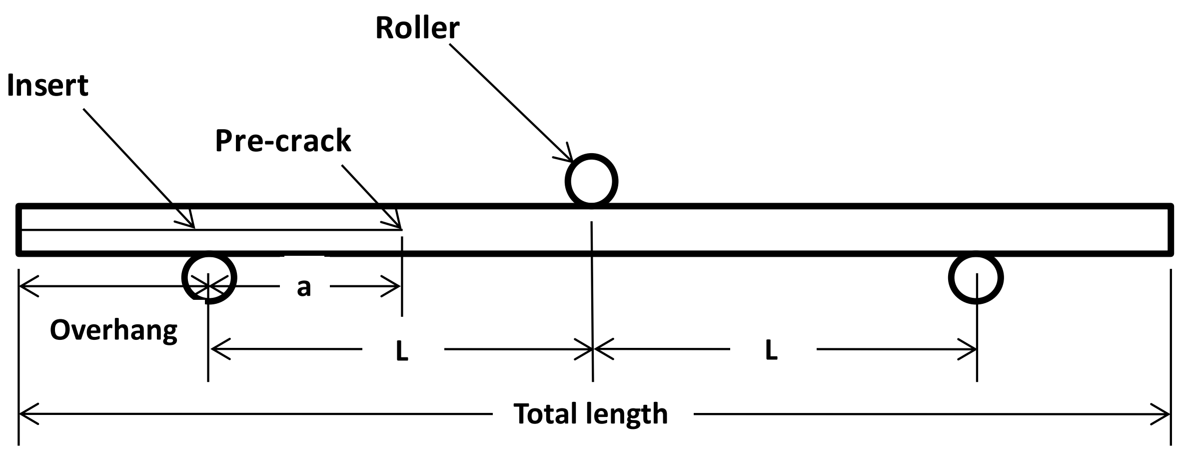

Figure 24. ENF specimen geometry

Measuring Mode-I Fracture Toughness

The interlaminar fracture toughness versus delamination length, also referred to as the resistance curve or R-curve, of one of the tested specimen is shown in Figure 25. The four different curves use slightly different equations to calculate the interlaminar fracture toughness at each recorded data point. These equations are given by Eq. (12) through (15).

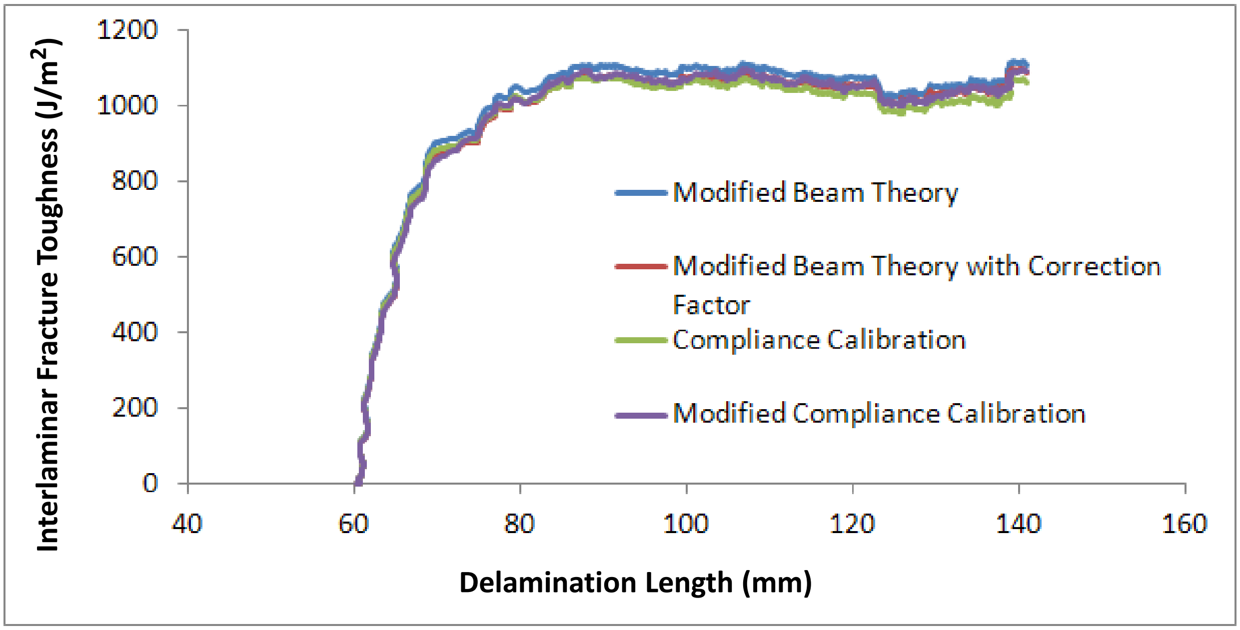

Figure 25. Interlaminar fracture toughness calculated by four different equations during delamination

The ASTM Standard specifies that the Modified Beam Theory with Correction Factor (MBTC) equation results in the most conservative calculation of interlaminar fracture toughness. Therefore, the fracture toughness of four specimens has been obtained using the MBTC value. The fracture toughness values are shown in Table 2 and were obtained at propagation points on the curve after it reached steady state. The values obtained were the maximum fracture toughness between 90 and 120 mm of delamination length. After 120 mm of delamination, it became increasingly difficult to track the crack length in the captured images and likely led to the slight drop-off in fracture toughness at this point. After this drop-off, the fracture toughness values increased until catastrophic failure of the specimen. This is as expected according to Hwang [64], and is likely caused by the increased angle of delamination and fiber bridging, which will be discussed later.

Table 2. Measured Mode-I interlaminar fracture toughness values

Specimen	Max Load (N)	G_I (J/m^2)
1	50.80	**996.83**
2	51.20	**1153.81**
3	47.31	**1089.14**
4	51.44	**1118.25**
	Average G_I:	**1089.51**

The load versus displacement curve of the DCB specimen measured during the Mode-I bending experiment is shown in Figure 26. The overlaid curves are theoretical approximations of the load versus displacement using linear elastic fracture mechanics beam theory. The steady decline in the load versus displacement curve after the peak load was reached demonstrates that stable crack propagation was achieved.

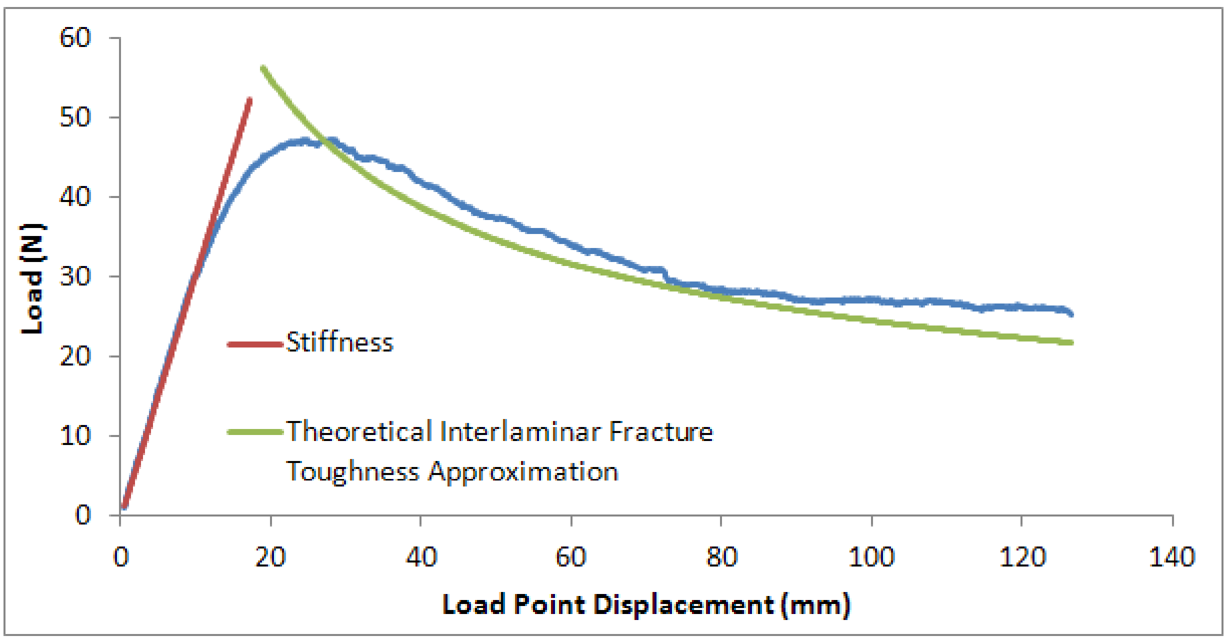

Figure 26. Load versus displacement with curve fits based on beam theory approximation

The stiffness curve of Figure 26 uses the compliance estimated by beam theory given as

$$C = \frac{8a^3}{EBh^3} \tag{18}$$

where B is the specimen width and h is half of the specimen thickness. The stiffness is then calculated as the ratio of load point displacement against compliance, *(Δ/C)*.

Figure 26 also uses a derivation of the beam theory approximation to theoretically predict the load versus displacement curve after peak load given by

$$F = \left[\frac{G_c^3 h^3 E}{27} \right]^{1/4} B\Delta^{-1/2} \tag{19}$$

This equation approximates the load as a function of interlaminar fracture toughness and displacement. The value for interlaminar fracture toughness remains constant throughout and is based on a maximum value from the R-curve. A derivation of this equation can be found in the Appendix.

It is seen in Figure 26 that the theoretical interlaminar fracture toughness approximation underestimates the load versus displacement curve. This is due to a phenomenon that occurs during delamination known as fiber bridging. Fiber bridging occurs when the fibers perpendicular to the direction of crack propagation and across the width of a unidirectional composite act to resist crack growth by “sticking” to one side of the specimen as it separates. Although this is a desirable quality in unidirectional composites that acts to increase the fracture toughness of the material, it is not accounted for in the theoretical approximation curve because this curve is derived from elementary beam theory normally used for metal beams that do not possess this quality. If it were possible to account for fiber bridging, it would be expected that the theoretical curve would be increased and could better predict the load versus displacement curve after peak load. Evidence of fiber bridging in one of the captured images during testing is shown in Figure 27.

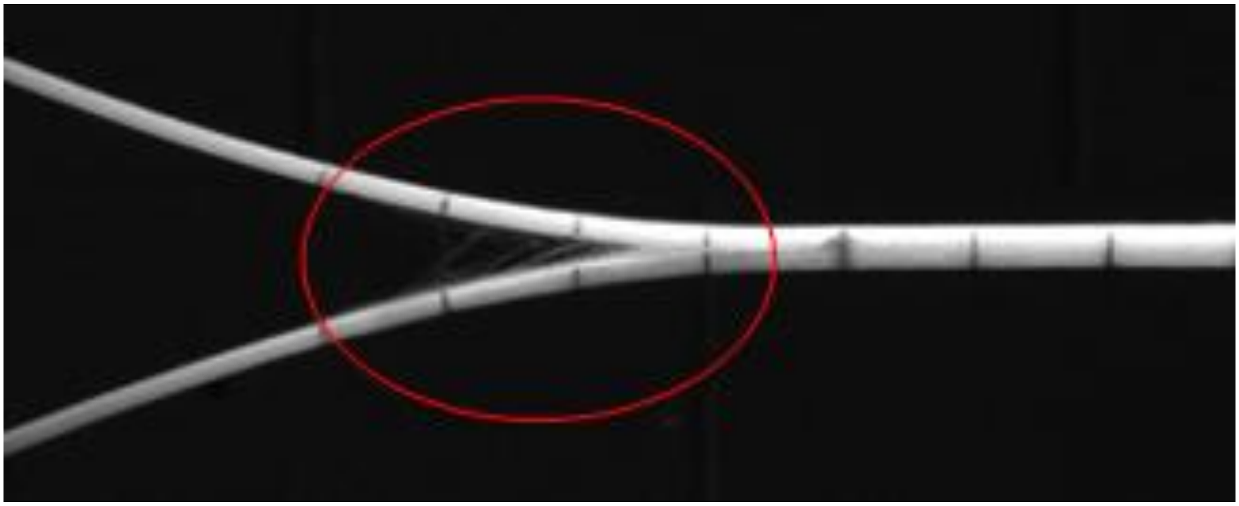

Figure 27. Fiber bridging occurring in specimen during testing

Measuring Mode-II Fracture Toughness

The results of the first set of specimen tested to calculate the Mode-II fracture toughness of the unidirectional glass/epoxy composite are shown in Figure 28. It is seen that the curves show a different trend than the Mode-I bending test in that the curve completely drops off after reaching a peak load. This is the result of unstable crack propagation and indicates a sudden crack jump in the specimen. This presents a problem because it is impossible to record fracture toughness values during propagation and limits the calculation of fracture toughness values to the point of onset of Mode-II fracture. Furthermore, it is a problem because stable crack propagation in this configuration is required for later testing in which FBG sensors will be embedded in the specimen. It will be necessary to investigate a way to solve this problem and stabilize the crack propagation.

Table 3 shows the calculated Mode-II fracture toughness values corresponding to the specimen shown in Figure 28. It is seen that there is a large variation in fracture toughness values of the specimen as high as 28% off from the average fracture toughness of the four specimens. Davies et al. [65] specify that a variation in fracture toughness of 15-20% deviation from average can be expected in situations where the crack is shown to be unstable. In addition to stabilizing crack propagation for the future testing of embedded FBG sensors, it is now also necessary to attempt to stabilize crack propagation to obtain more accurate fracture toughness values.

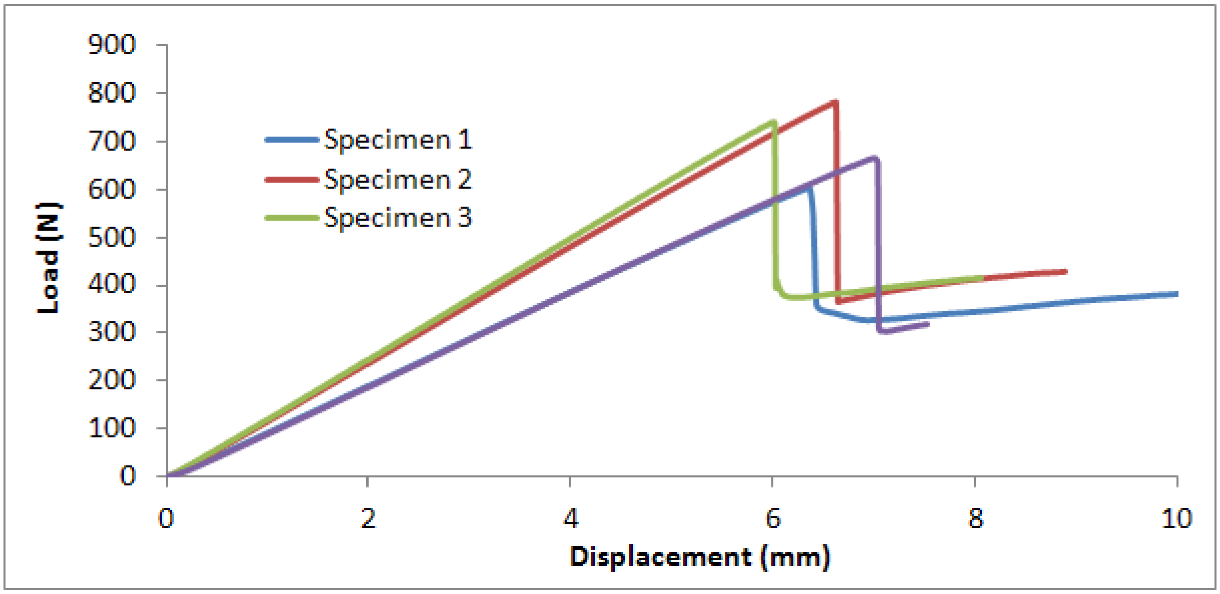

Figure 28. Load versus displacement curves of Specimen 1-4

Table 3. Measured Mode-II fracture toughness values – Panel 1

Specimen	a/L	Max Load (N)	G_{II} (J/m^2)	% Deviation
1	0.5	606.28	**1310.79**	22.61
2	0.5	780.96	**2169.34**	28.09
3	0.5	742.59	**1799.02**	6.22
4	0.5	668.13	**1495.53**	11.70
		Average G_{II}:	**1693.67**	

Stabilization of Crack Propagation Subject to Mode-II Bending

Davies et al. [65] specify that it is possible to create stable crack propagation in an ENF specimen by increasing the *a/L* ratio above 0.7. In order to test this theory, additional specimen were manufactured with an *a/L* ratio of 0.75. The load versus displacement curves of the additional ten specimens tested are shown in Figure 29.

Although Specimen 8 shows signs of stable crack propagation as it does not completely drop off vertically, the other nine specimens still show unstable crack propagation and thus an increase in *a/L* ratio could potentially stabilize crack propagation albeit with very little consistency. Table 4 shows the fracture toughness values corresponding to the specimens shown in Figure 29. It is seen that these specimens have the same deviation range in fracture toughness as the previous group.

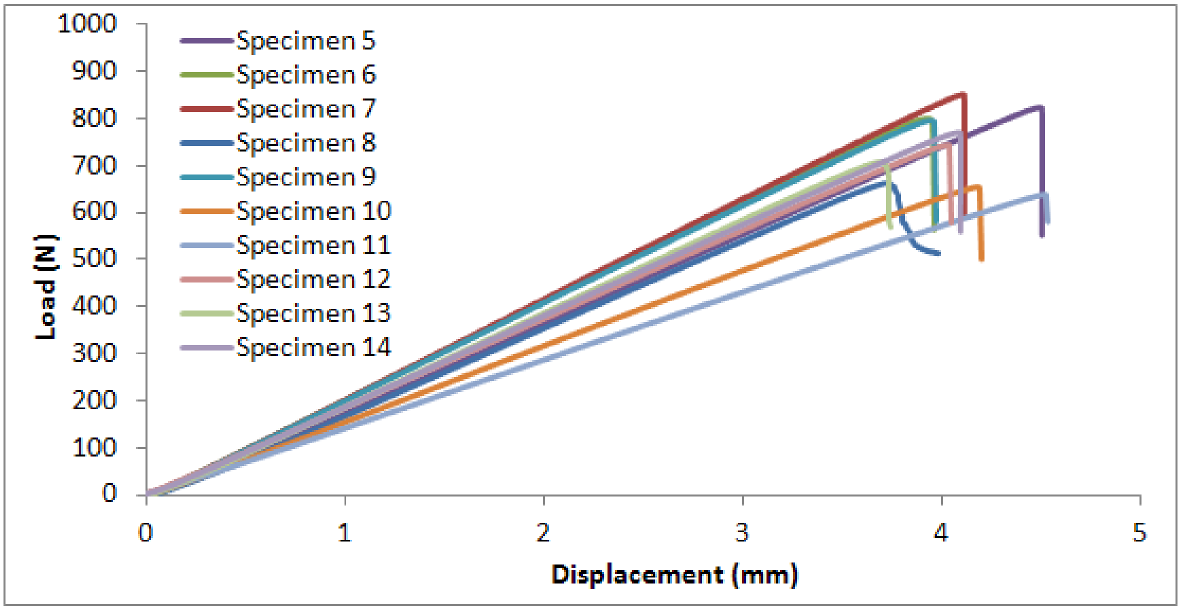

Figure 29. Load versus displacement curves of Specimen 5-14

Table 4. Measured Mode-II fracture toughness values – Panel 2

Specimen	a/L	Max Load (N)	G_{II} (J/m^2)	% Deviation
5	0.75	822.51	**2429.36**	27.03
6	0.75	799.46	**2076.31**	8.57
7	0.75	852.07	**2342.78**	22.51
8	0.75	661.50	**1463.44**	23.47
9	0.75	795.05	**2019.22**	5.59
10	0.75	652.24	**1742.03**	8.91
11	0.75	637.87	**1507.47**	21.17
12	0.75	742.73	**1967.37**	2.88
13	0.75	707.48	**1638.66**	14.31
14	0.75	769.22	**1937.00**	1.29
		Average G_{II}:	**1912.36**	

Based on these results, it is evident that further testing and investigation is needed on the ability to stabilize crack propagation. Kageyama et al. [66] created and patented a device similar to an extensometer that attaches to the delamination front of the specimen and allows for control to a constant shear displacement and produces stable crack propagation. Although this method requires the purchase of additional equipment, or the manufacturing of an extensometer-like device, it is a proven method of stabilization.

Findings

A Mode-I bending test has been performed on multiple specimens to find an average Mode-I fracture toughness value of 1090 J/m^2. An improved method for locating the crack tip and analyzing captured images of the propagating crack in MATLAB has been presented. A Mode-II bending test was performed on two sets of specimens, first on a set with an *a/L* ratio of 0.5 and then on a set with an *a/L* ratio of 0.75 in an unsuccessful attempt to stabilize crack propagation. Regardless, average Mode-II fracture toughness values of 1694 and 1912 J/m^2 were found for the first and second set of specimen, respectively, albeit from a large variation of data.

Setting Test Standards for Specimen with Embedded FBG Sensors

The Mode-I and Mode-II bending tests conducted will act as excellent baseline tests for the experiments to come in Chapter 6. In Chapter 6, FBG sensors will be embedded in the same type of specimens used in the above experiments and will be subjected to the same Mode-I and Mode-II bending tests. While stable crack propagation could not be achieved in the Mode-II bending test under monotonic loading, Chapter 6 will explore cyclic loading as a means of solving this problem. The introduction of FBG sensors into the specimen will allow an experimental validation of their damage detection capabilities and will support the results of a numerical analysis of an FBG sensor's response to non-uniform strain outlined in the next chapter.

CHAPTER 5
NUMERICAL ANALYSIS OF FBG RESPONSE TO NON-UNIFORM STRAIN

Introduction

An FBG sensor subjected to constant strain along its gauge length will maintain a linear relationship between peak wavelength and applied strain. However, when the sensor experiences non-uniform strain along its gauge length caused by local damage, the spectral response will change as a function of this non-uniform strain distribution and the linear relationship will no longer hold true. Studying the spectrum response and inherent spectrum broadening through a numerical analysis of an FBG subjected to non-uniform strain will improve structural health monitoring capabilities and aid in damage analysis.

A numerical analysis of this type has previously been used by Yashiro et al. [48] and Ling et al. [49] to build reflection spectra that verify those obtained experimentally with FBG sensors embedded in composite specimens subjected to various loading scenarios. However, in this work, the numerical analysis will be used to build hundreds of reflection spectra that can then be used to identify a new quantification parameter. It will be used to study the relationship between this quantification parameter and the strain gradient and test the established relationship's versatility. The numerical analysis will also be used to compare a new spectrum monitoring method to an existing spectrum quantification method by using each to measure the same simulated spectra.

Objectives

The objective of this work is to develop a numerical analysis method to predict a reflection spectrum of a fiber-Bragg grating subjected to non-uniform strain using a transfer matrix formulation. The effect of various non-uniform strain distributions on the reflection spectrum of an FBG sensor will be investigated. During the investigation of these various non-uniform strain distributions, an optimal parameter for quantifying the spectrum shape for monitoring damage will be identified. The proposed optimal parameter will be shown to be a better method of detecting a propagating crack than the peak intensity ratio method.

Peak Wavelength Spectrum Monitoring Method

FBG sensors are strain-based sensors that were originally developed for uniform strain measurement purposes. The peak wavelength of the reflection spectrum produced by an FBG sensor has a direct correlation with the average strain along its gauge length. However, monitoring the peak wavelength lacks a quantitative damage monitoring capability due to the resulting ambiguity in differentiating a change in signal due to a normal structural response from an abnormal response caused by damage.

Peak Intensity Ratio Spectrum Monitoring Method

Takeda et al. [27, 32, 33] proposed the peak intensity ratio method as a way to measure delamination length based on the reflection spectrum and created a quantitative damage monitoring capability for FBG sensors. The peak intensity ratio measures the intensity ratio of the two peaks that appear in the spectrum when an FBG sensor is subjected to non-uniform strain. This monitoring method is flawed because it relies on the presence of two peaks in the reflection spectrum and in some cases the spectrum is much more complex and displays several peaks. A more robust structural health monitoring parameter must be identified through a numerical analysis of the reflection spectrum.

Transfer Matrix Method

The transfer matrix formulation originally presented in [47, 56] can be employed to investigate the effect of strain gradient on the reflection spectrum of FBG sensors [57]. First, consider two counter propagating plane waves contained in an optical fiber core and traveling through a Bragg grating of length *L* and grating period Λ (Figure 30).

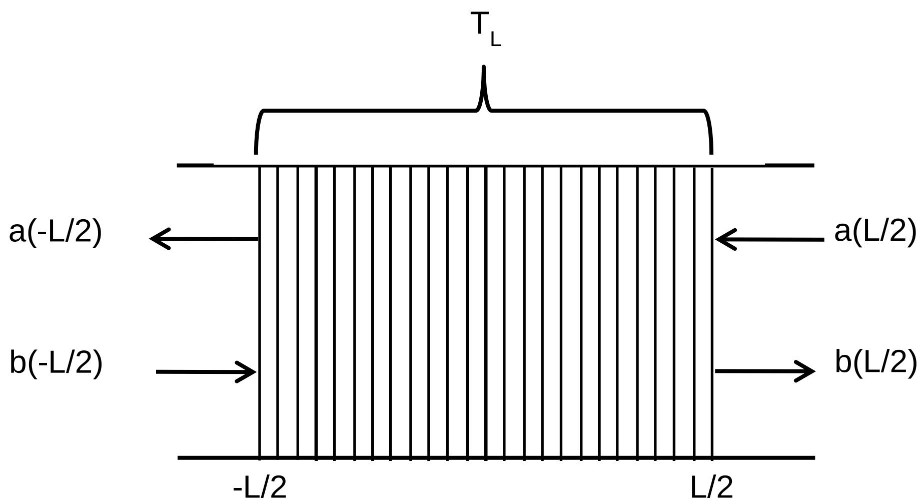

Figure 30. T-matrix model for a uniform grating

The amplitudes of the reflected light at the front and back of the grating are denoted as *a*(-*L*/2) and *a*(*L*/2), respectively, while *b*(-*L*/2) and *b*(*L*/2) correspond to the amplitudes of the transmitted light reaching the front and back of the grating, respectively. The scattering matrix in [56] can be used to obtain the transfer matrix relation [58] that relates the signals at the left side of the grating to those at the right side by

$$\begin{bmatrix} a(-L/2) \\ b(-L/2) \end{bmatrix} = \begin{bmatrix} T_{11} & T_{12} \\ T_{21} & T_{22} \end{bmatrix} \begin{bmatrix} a(L/2) \\ b(L/2) \end{bmatrix} \tag{20}$$

where

$$T_{11} = \cosh(\gamma_B \Delta z) - i\frac{\hat{\sigma}}{\gamma_B}\sinh(\gamma_B \Delta z) \tag{21}$$

$$T_{22} = \cosh(\gamma_B \Delta z) + i\frac{\hat{\sigma}}{\gamma_B}\sinh(\gamma_B \Delta z) \tag{22}$$

$$T_{12} = -i\frac{\kappa}{\gamma_B}\sinh(\gamma_B \Delta z) \tag{23}$$

$$T_{21} = i\frac{\kappa}{\gamma_B}\sinh(\gamma_B \Delta z) \tag{24}$$

with

$$\gamma_B = (\kappa^2 - \hat{\sigma}^2)^{1/2} \tag{25}$$

$$\kappa = \frac{\pi}{\lambda}\upsilon\overline{\delta n_{eff}} \tag{26}$$

$$\upsilon = \frac{1}{2}e^{\left(-\alpha\left(\frac{z}{L}\right)^2\right)} \tag{27}$$

$$\hat{\sigma} = \frac{2\pi}{\lambda}\left(n_{eff} + \overline{\delta n_{eff}}\right) - \frac{\pi}{\Lambda(z)} \tag{28}$$

where z is the position along the grating, Δz is the length of the gauge section, $\hat{\sigma}$ is the general "dc" self-coupling coefficient as a function of the propagating wavelength λ, κ is the "ac" coupling coefficient, $\overline{\delta n_{eff}}$ is the "dc" index change spatially averaged over a grating period, ν is the fringe visibility, α controls the smoothness of the generated reflection spectrum, n_{eff} is the effective index of refraction, and $\Lambda(z)$ is the effective grating period [59].

For a non-uniform grating of total length L, the grating can be divided into m individual gratings with each element being of length l_i such that $L = l_1 + l_2 + \ldots + l_m$. The T-matrix of the non-uniform grating can be written as

$$[T_L] = [T_{l_1}][T_{l_2}]\ldots[T_{l_m}] \tag{29}$$

where $[T_L]$ denotes the *T*-matrix for the whole grating and $[T_{li}]$ denotes the *T*-matrix for the *i*th grating segment. The individual gratings are assumed to be uniform but have different values of κ, Λ, and $\hat{\sigma}$. The transfer matrix relation can then be written as

$$\begin{bmatrix} a(-L/2) \\ b(-L/2) \end{bmatrix} = [T_M][T_{M-1}] \ldots [T_J] \ldots [T_l] \begin{bmatrix} a(L/2) \\ b(L/2) \end{bmatrix}. \tag{30}$$

From the boundary conditions of *a*(-*L*/2) = 0 and *b*(*L*/2) = b_L assuming no backward input on the far end of the grating, the amplitudes of the reflected and transmitted lights, a(-*L*/2) and b(-*L*/2), can be determined and used to calculate the spectral reflectivity of the grating by [57]

$$R(\lambda) = \left| \frac{a\left(-\frac{L}{2}, \lambda\right)}{b\left(-\frac{L}{2}, \lambda\right)} \right|^2 . \tag{31}$$

For a non-uniform strain field, the effective grating period defined in [57] can be written as

$$\Lambda(z) = \Lambda_0[1 + (1 - p_e)\varepsilon(z)] \tag{32}$$

where Λ_0 is the period of the grating in the reference configuration, the photoelastic constant p_e takes into account the change in effective refractive index of the optical fiber, and $\varepsilon(z)$ is the axial strain distribution. However, it was recently pointed out that the effective grating period in Eq. (32) is inaccurate [59], and a modified form of the effective grating period was given as

$$\widetilde{\Lambda}(z) = \Lambda_0[1 + (1 - p_e)\varepsilon(z) + (1 - p_e)z\varepsilon'(z)] \tag{33}$$

where ε'(z) is the strain gradient. The "dc" self-coupling coefficient in Eq. (28) must then be modified as

$$\hat{\sigma}_{modf} = \frac{2\pi}{\lambda}\left(n_{eff} + \overline{\delta n_{eff}}\right) - \frac{\pi}{\widetilde{\Lambda}(z)} \tag{34}$$

Effect of Linear Strain Distribution on the Spectrum

The modified Transfer Matrix Method was used to construct the reflection spectra of an FBG sensor subjected to linear strain distributions along its gauge length. The construction of reflection spectra at various strain gradients allowed for an investigation of spectrum bandwidth quantification methods. The grating modeled in this study has the following parameters: n_{eff} = 1.46, λ_B = 1557 nm, L = 10 mm, $\overline{\delta n_{eff}}$ = 3.4 x 10^{-4}, p_e = 0.26, and α = 1. The linear strain distribution is expressed as

$$\varepsilon(z) = b * (2z / L) \tag{35}$$

where b is the absolute strain at the front and back tips of the sensor and z is the position along the gauge length. The reflection spectra constructed with five different absolute strain values and linear strain distributions are shown in Figure 31. As the strain gradient increases, the peak intensity decreases and the spectrum bandwidth increases.

Several definitions can be used to quantify the spectrum bandwidth. The most commonly used definition is the full width at half maximum (FWHM) which corresponds to a -3 dB bandwidth in the logarithmic scale. In this investigation, different definitions of -6 dB, -10 dB, and -20 dB bandwidth are also used. The relationship between the strain gradient and the spectrum bandwidth are plotted in Figure 32. The relationships were found to be non-linear in general. However, it was found that the trend can be well approximated with linear functions especially when -10 dB and -20 dB bandwidth definitions are used. The optimal definition for measuring spectral bandwidth was determined to be -10 dB or -20 dB depending on the signal-to-noise ratio of the FBG sensor.

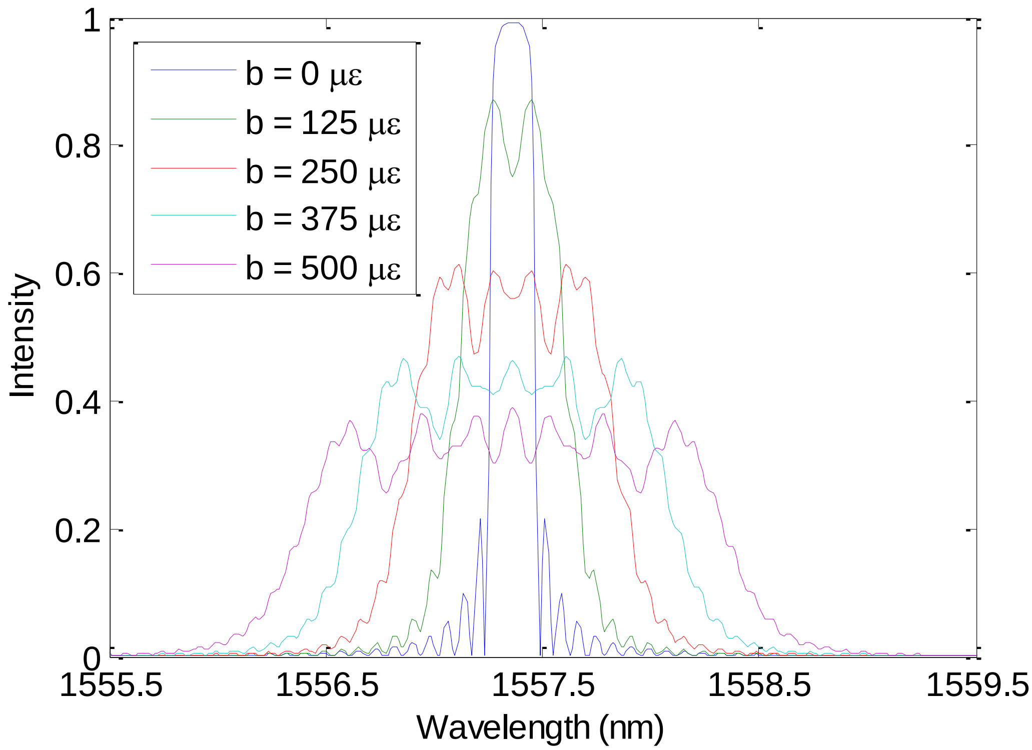

Figure 31. Reflection spectra of a FBG sensor subjected to five different absolute strain values and linear strain distributions

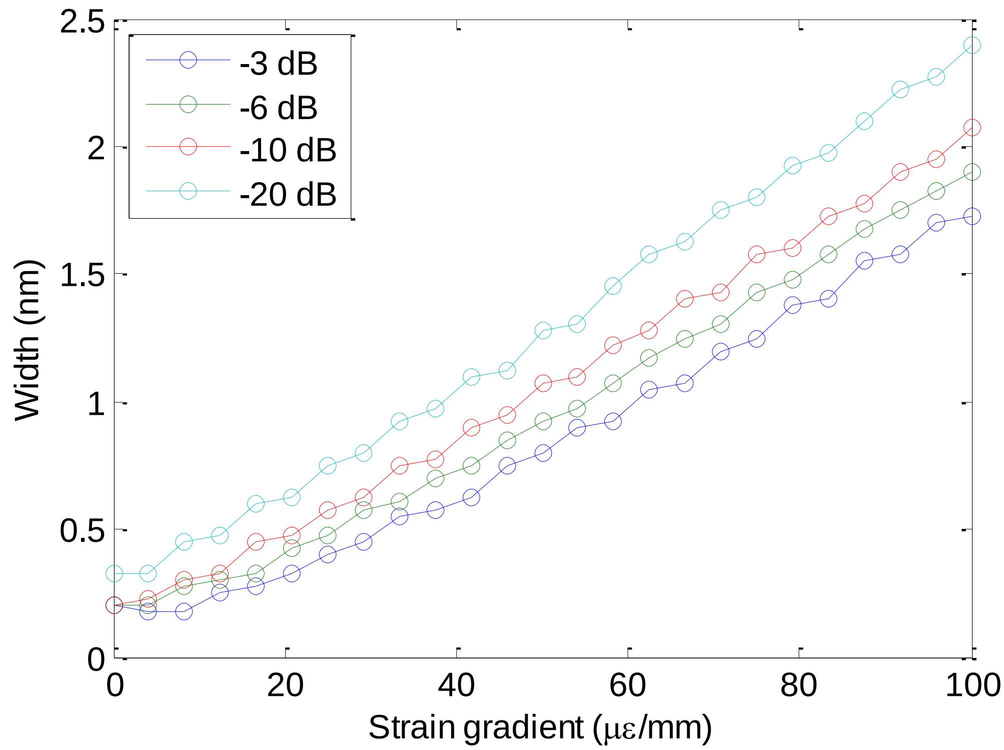

Figure 32. Relations between the strain gradient and the spectrum bandwidth determined by different definitions of the spectral bandwidth

Effect of Quadratic Strain Distribution on the Spectrum

To investigate the effect of the higher order terms on the relationship between the spectrum bandwidth and the strain gradient, the quadratic strain distributions are included in the non-uniform strain distributions as

$$\varepsilon(z) = a\left(\frac{2z}{L}\right)^2 + b\left(\frac{2z}{L}\right). \tag{37}$$

The changes in the spectrum shape due to the quadratic term are shown in Figure 33. As the magnitude of the quadratic term increases, the resulting spectra become asymmetrical but did not show any significant broadening.

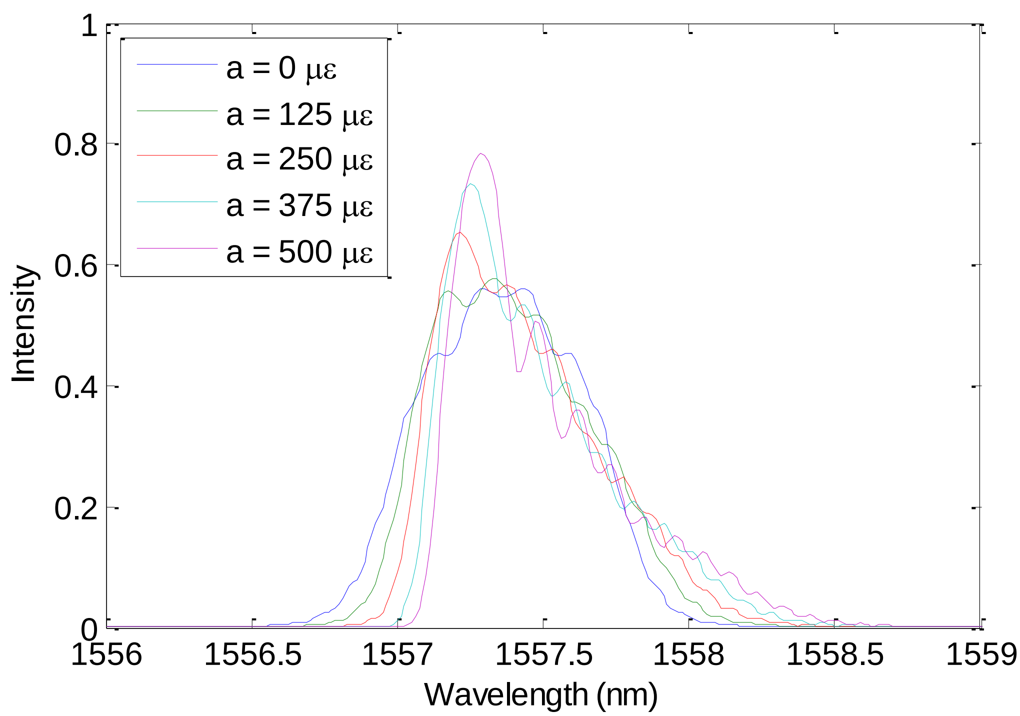

Figure 33. Reflection spectra of a FBG sensor subjected to quadratic strain distributions.

The relations between the spectrum bandwidth and the magnitude of the second order term are plotted in Figure 34. It is shown that the -20 dB bandwidth measurements remain relatively constant as the second order term increases. Thus, the presence of a second order term in the strain distribution will have little effect on the bandwidth measurement by -20 dB bandwidth, and the linear relationship between the spectrum bandwidth and the strain gradient will hold true.

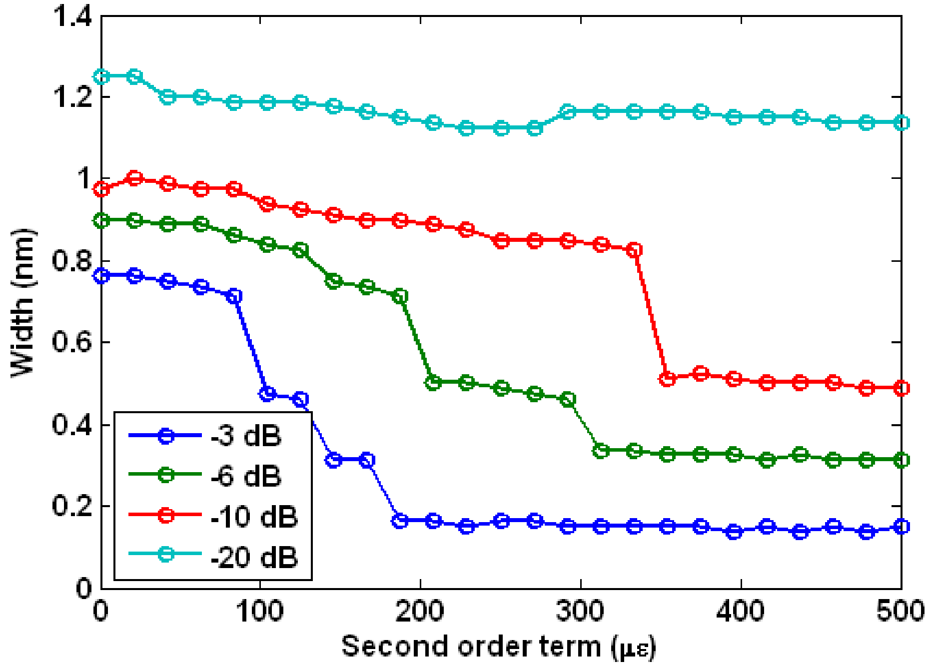

Figure 34. Relation between the spectral bandwidth and the magnitude of quadratic strain distribution

Effect of Highly Non-Uniform Strain Distribution on the Spectrum

The relationship between the strain gradient and the spectrum bandwidth was also investigated for highly non-uniform strain distributions. The reflection spectra constructed with five different absolute strain values and highly non-uniform strain distributions are shown in Figure 35.

The relationship between the strain gradient and the spectrum bandwidth measured from the reflection spectra shown in Figure 35 are plotted in Figure 36. The relationship remains best approximated with linear functions with optimal definitions for measuring spectral bandwidth of -10 dB or -20 dB. This confirms that the relationship holds true for a more complex strain distribution and one that is most likely to be experienced by an embedded FBG sensor.

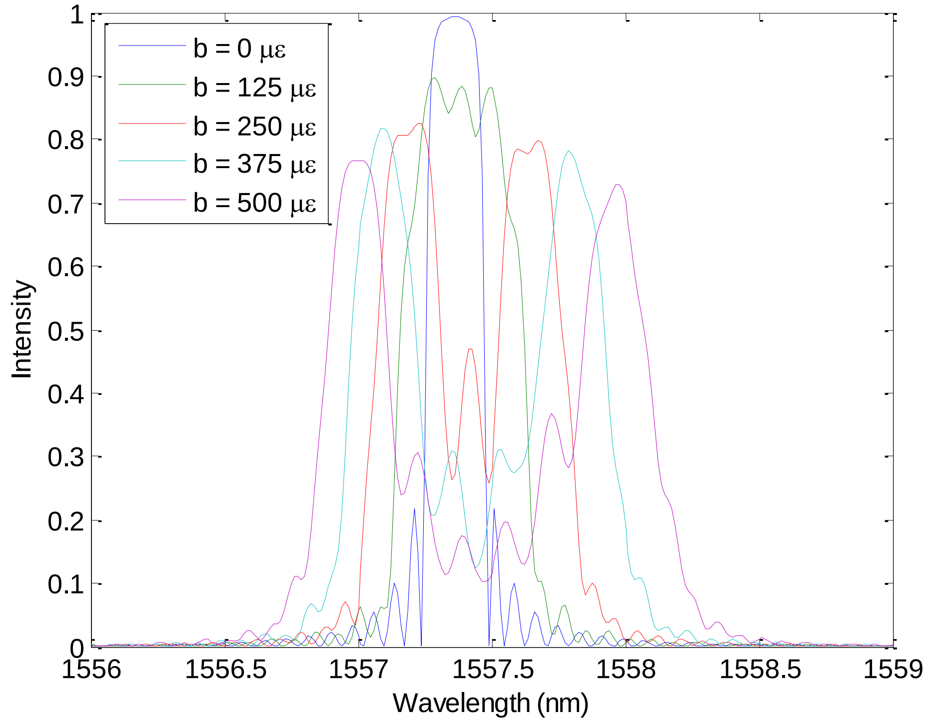

Figure 35. Reflection spectra of a FBG sensor subjected to five different absolute strain values and discontinuous strain distributions

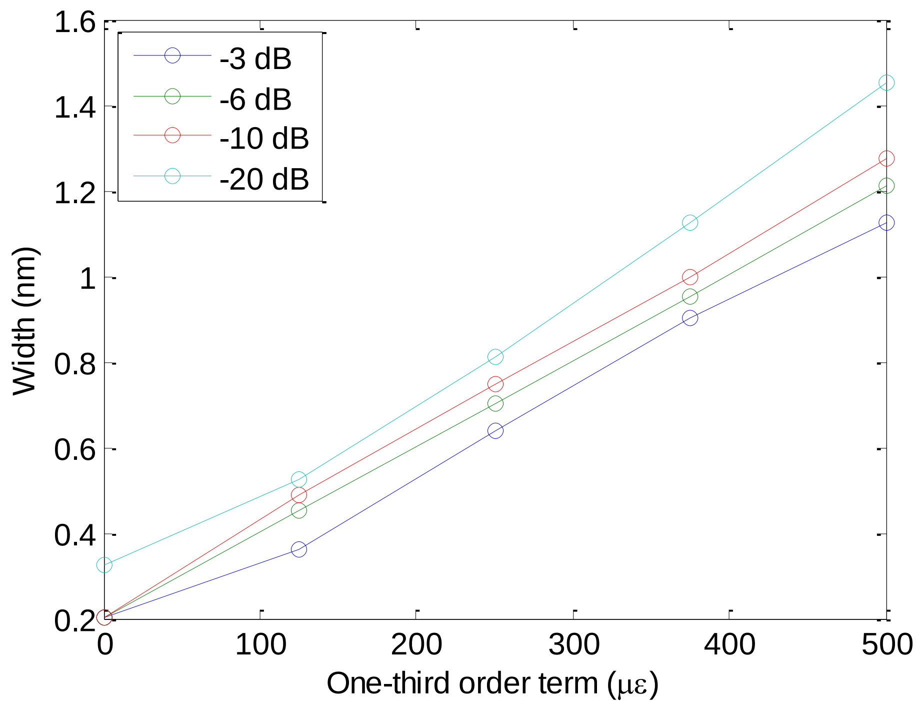

Figure 36. Relations between the strain gradient and the spectrum bandwidth determined by different definitions of the spectral bandwidth

Monitoring Peak Intensity Ratio vs. Spectrum Bandwidth

Currently, the peak intensity ratio method is being used to measure delamination length and has been identified as the only method that provides the capability for quantitative damage monitoring [27, 32, 33]. However, it is not always a simple task to identify two distinct peaks in the reflection spectrum during crack propagation. In this section, the existing spectrum quantification method (peak intensity ratio) will be compared with a new interrogation method (spectrum bandwidth).

A numerical simulation was performed in which a crack propagated along the gauge length of a FBG sensor for the purpose of comparing the peak intensity ratio and spectrum bandwidth monitoring methods. The propagating crack was simulated by moving a discontinuous strain distribution along the sensor's gauge length at 1 mm intervals and obtaining the reflection spectrum at each. The distribution of the strain is given by

$$\varepsilon(z) = b * [2(z + c) / L]^{1/3} \tag{36}$$

where c is used to shift the curve from the zero position of the gauge length. The collection of the ten discontinuous strain distributions is displayed in Figure 37.

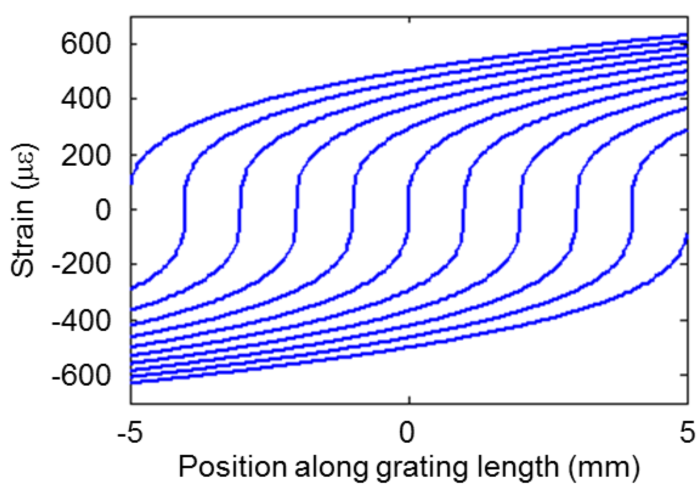

Figure 37. Collection of discontinuous strain distributions used to simulate the propagation of a crack along the FBG sensor's gauge length

A sample reflection spectrum generated at a crack tip position of -2 mm along the gauge length is shown in Figure 38. The intensities of the longer and shorter wavelength peaks are identified as I_1 and I_2, respectively. The peak intensity ratio is measured as I_1/I_2.

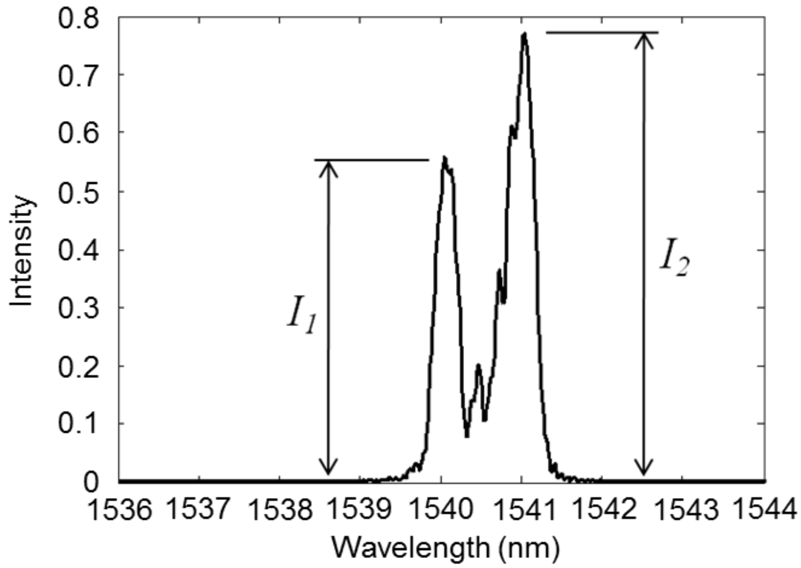

Figure 38. Reflection spectrum generated at a crack tip position of -2 mm along the gauge length

A comparison of measuring the peak intensity ratio versus the spectrum bandwidth during crack propagation is shown in Figure 39. Monitoring the peak intensity ratio (Figure 39a) produces a steadily increasing curve as the crack tip position gets further along the gauge length. However, points are only produced between -3 to 3 mm as there is only one identifiable peak in the spectrum outside this region. Alternatively, the spectrum bandwidth (Figure 39b) is able to produce measurements along the entire gauge length. All bandwidth curves show a significant spike near the front edge indicating that the crack has entered the gauge length and show only a slight change as the crack propagates through. The signals return to their initial value as the crack leaves the gauge length.

For real-time damage monitoring purposes, the spectrum bandwidth is the optimal monitoring method as it provides a continuous signal with a distinct indicator of crack detection.

Additionally, monitoring the spectrum bandwidth at a -20 dB bandwidth allows for crack detection 1 mm earlier than the peak intensity ratio method. The significant jump in width that occurs between -5 and -4 mm while measuring the -20 dB bandwidth acts as an indicator of crack detection while the peak intensity ratio method is not able to detect damage until a crack tip position of -3 mm.

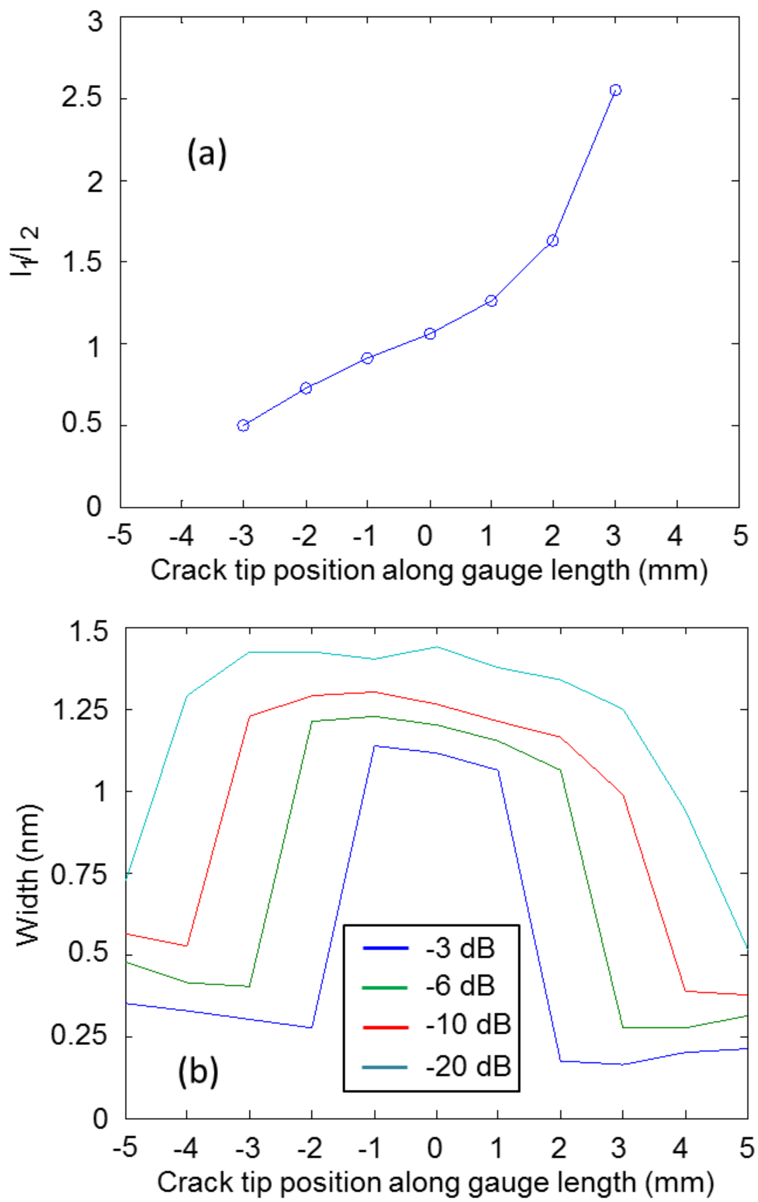

Figure 39. Peak intensity ratio (I_1/I_2) (a) and spectrum bandwidth (b) as crack propagates along gauge length

Findings

This numerical analysis employed a transfer matrix formulation in order to produce a reflection spectrum based on a user-input strain distribution. The numerical analysis was used to generate many reflection spectra to identify a parameter for adequately quantifying the signal for health monitoring purposes. The parameter, chosen as spectrum bandwidth, was compared to the strain gradient of various linear strain distributions and it was found that their relationship was close to linear. More complex strain distributions were then investigated to determine their effect on this relationship. Introducing a second order term to create a quadratic strain distribution resulted in little effect between the -20 dB bandwidth and strain gradient. Finally, a highly non-uniform strain distribution was shown to maintain the same linear relationship between bandwidth and strain gradient.

Application of Numerical Analysis to Testing of Embedded FBG Sensors

This numerical analysis has identified an optimal parameter for quantifying the reflection spectrum of an FBG sensor. It is believed that monitoring the -20 dB bandwidth during crack propagation could provide an improvement of structural health monitoring capabilities over monitoring the peak wavelength. Additionally, it could provide an improvement over the peak intensity ratio method because it is capable of providing a constant signal and an earlier crack detection time. For these reasons, a new interrogation method based on -20 dB bandwidth and center wavelength is proposed.

The benefits of spectrum bandwidth monitoring can be further investigated through experimental testing of embedded FBG sensors for structural health monitoring purposes. In Chapter 6, it will be physically demonstrated how utilizing the spectrum bandwidth monitoring method is a significant improvement over the current peak wavelength monitoring method.

CHAPTER 6
MONITORING INTERLAMINAR CRACK GROWTH IN COMPOSITE LAMINATES USING EMBEDDED FBG SENSORS

Introduction

In this work, embedded FBG sensors will be used to monitor the interlaminar crack growth in composite specimens subjected to monotonic and cyclic loading through various bending modes. The reflection spectra of the FBG sensor will be recorded as the crack propagates along the mid-plane of the specimen and will be analyzed to demonstrate crack detection capability. This work will be an experimental validation of the response of an FBG sensor to non-uniform strain, previously investigated through a numerical analysis in the previous chapter, with a focus on monitoring interlaminar crack growth using a new interrogation method.

The test procedures for the following experiments have been previously established in Chapter 4 in which baseline testing of the composite specimens was performed to set precise test parameters for stable crack propagation. Although stable crack propagation was not previously achieved under Mode-II bending, the following work will solve this problem using cyclic loading. Each specimen from the baseline testing in Chapter 4 will now include an embedded FBG sensor for structural health monitoring purposes.

Previous Work

Although many research groups have reported the presence of 'spectrum broadening' when the FBG sensor is subjected to non-uniform strain, a relatively small number of works have been made to quantify the changes of the reflection spectrum for damage monitoring purposes. Takeda et al. [27, 32, 33] used the ratio of the peak intensities in the reflection spectrum as an indicator of damage growing in composite materials and Ling et al. [34] noted that the bandwidth of the reflection spectrum increases as the non-uniformity of the strain distribution increases, but did not quantify the trend beyond the peak intensity ratio method.

The newly proposed interrogation method will both improve upon the peak intensity ratio method, as discussed in the previous chapter, and provide a robust spectrum quantification capability.

Objectives

The following experiments will validate the optimal parameter for spectrum quantification that was previously identified in Chapter 5 as the spectrum bandwidth. The benefits of using either the spectrum bandwidth or center wavelength monitoring method in place of the peak wavelength monitoring method will be clearly defined through these experiments.

Manufacturing of Composite Specimen

Unidirectional glass/epoxy composite laminates to be used in the following experiments were manufactured by a hand lay-up of 16 plies of pre-preg sheets (Cycom 1003) and cured in a hot press. During the hand lay-up process, a Teflon film of approximate length 50 mm was inserted in the mid-plane to act as an initial crack, and an FBG sensor was embedded at the +2 or +6 ply location from the mid-plane for each laminate (Figure 40). The center of the FBG sensor with a 10 mm gauge length was located approximately 12.5 mm away from the initial crack tip. The specimens measured approximately 152.4 x 25.4 x 3 mm^3.

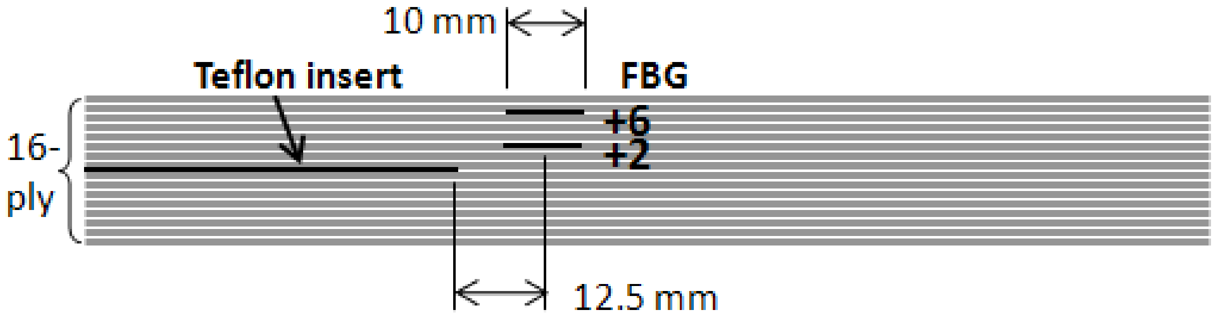

Figure 40. Side view of specimen lay-up showing an embedded Teflon insert and potential sensor locations

Mode-I Bending Interlaminar Fracture Test

A Mode-I interlaminar quasi-static fracture test was conducted as a validation experiment following the ASTM Standard D5528--01 [60]. The Double Cantilever Beam (DCB) specimen (Figure 41) with an FBG sensor embedded at the +6 ply location was pulled at 5 mm/min and the sensor was monitored using an interrogator (Micron Optics, sm125) capable of recording the reflection spectrum in the wavelength range of 1510 to 1590 nm with an accuracy of 2.5 pm and a scan frequency of 5 Hz.

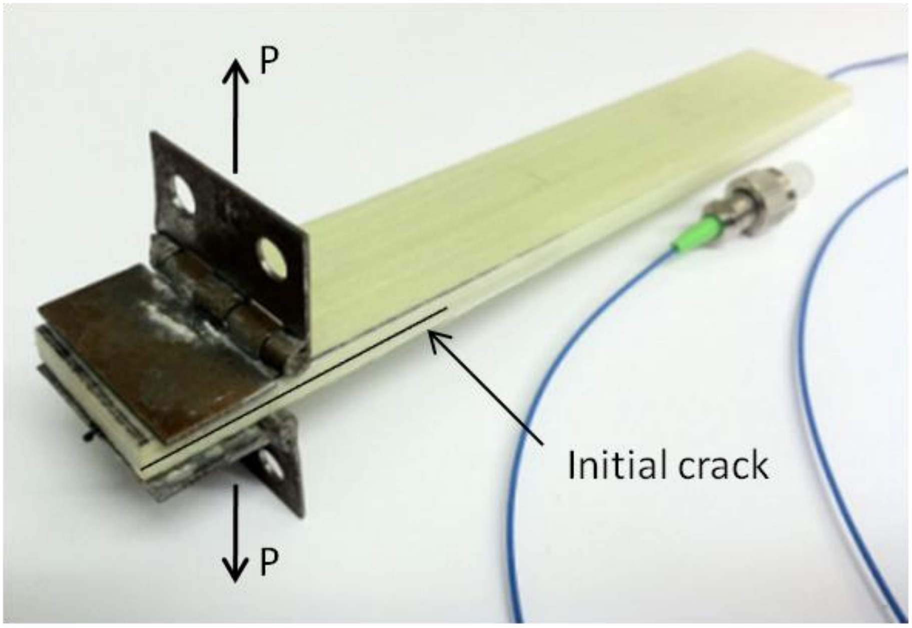

Figure 41. Double Cantilever Beam (DCB) specimen for mode-I interlaminar fracture test

Mixed-Mode Bending Interlaminar Fracture Test

A mixed-mode interlaminar fracture test was also conducted by using a mixed-mode bending (MMB) test setup shown in Figure 42. A FBG sensor was embedded at the +6 ply location. The test fixture used in this experiment is described in detail by ASTM D 6671-04 [67]. The fixture is designed to apply a specific ratio of Mode I to Mode II loading by varying the position of the loading yoke. The ratio of Mode I to Mode II loading for this experiment was 3:1 and the specimen was loaded at 2 mm/min.

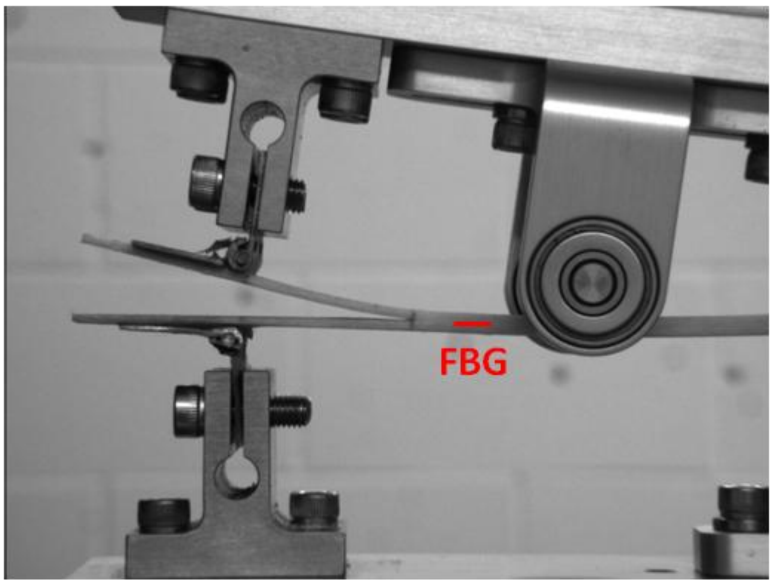

Figure 42. Mixed-mode bending test setup for mixed-mode interlaminar fracture test

Mode-II Bending Interlaminar Fracture Test

A Mode-II interlaminar fatigue fracture test was conducted by using an End Notched Flexure (ENF) test geometry shown in Figure 43. A FBG sensor was embedded at the +2 ply location. A cyclic load was applied at the mid-span at 1 Hz, and the peak load and the minimum load were 300 N and 30 N, respectively. The reflection spectrum was recorded in the same manner as the previous experiments.

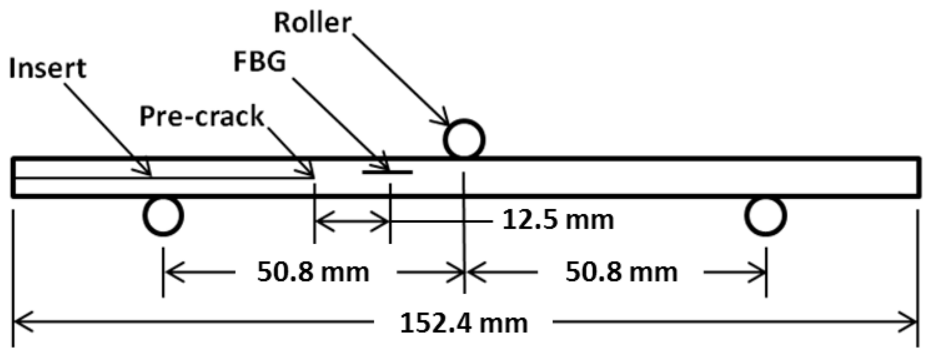

Figure 43. Edge-notched-flexure test setup for interlaminar fatigue test

Validation Experiment 1 – Double Cantilever Beam Experiment

The history of the average strain recorded by the FBG sensor during the mode-I fracture test is shown in Figure 44. The average strain is calculated by

$$\varepsilon = F_g * \left(\frac{\Delta\lambda_B}{\lambda_B}\right) \tag{38}$$

where F_g is the gage factor of the FBG sensor and $\Delta\lambda_B$ is the peak wavelength shift. The sudden jump in strain that occurs near 300 seconds is the result of the propagating crack reaching the FBG sensor.

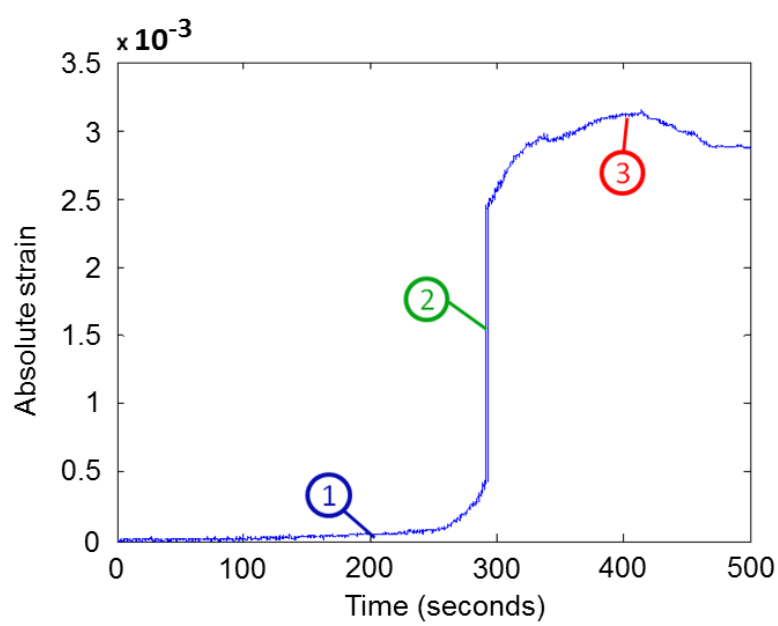

Figure 44. Time-history of the average strain during the mode-I interlaminar fracture test

The reflection spectra at the three different points indicated in Figure 44 are shown in Figure 45. At point 1, before the crack reaches the location of the sensor, the reflection spectrum shows a distinct peak with a bandwidth of approximately 1 nm. At point 2, once the crack is within the gage section of the sensor, the amplitude signal decreases and the spectrum becomes broader while displaying multiple peaks. The spectral bandwidth has increased to approximately 4 nm. The behavior of the signal at this point indicates that the FBG sensor has detected the non-uniform strain caused by the interlaminar crack growth. At point 3, once the crack tip has passed the location of the sensor, the spectrum returns to the original shape and shows one distinct peak that is similar to the initial peak. The shift of the peak wavelength indicates that the FBG sensor is subjected to a uniform compression due to the bending of the beam.

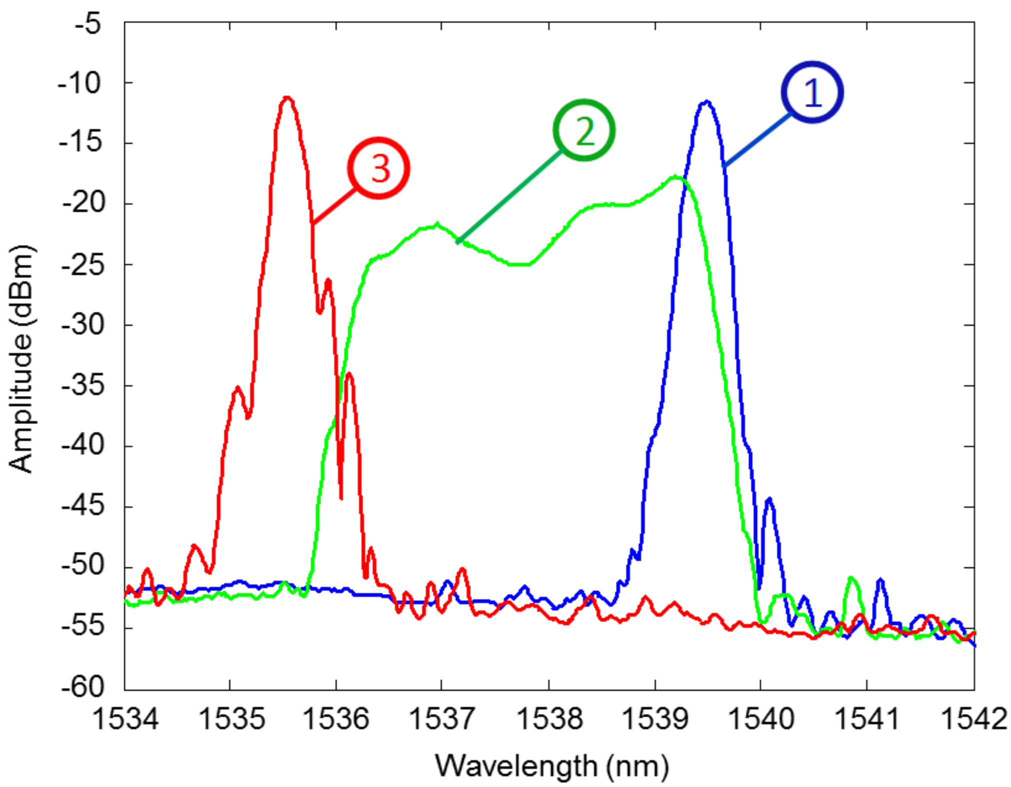

Figure 45. The reflection spectra at the three different points indicated in Figure 44

The peak wavelength, center wavelength, and -20 dB bandwidth measured during the Mode-I interlaminar fracture test on a DCB specimen with a +6 sensor embedding location are shown in Figure 46. All signals remain constant until the crack reaches the vicinity of the FBG sensor. As the crack reaches the sensor, the strain concentration near the crack tip causes the shift and broadening of the reflection spectrum. The bandwidth signal increases as the crack approaches, reaches a peak when the crack tip reaches the center of the gauge section, and returns to nearly the initial bandwidth as the crack passes the sensor. As a result, the peak wavelength changes rapidly while the center wavelength changes gradually. It is noted that monitoring the spectral bandwidth allows early detection of crack propagation.

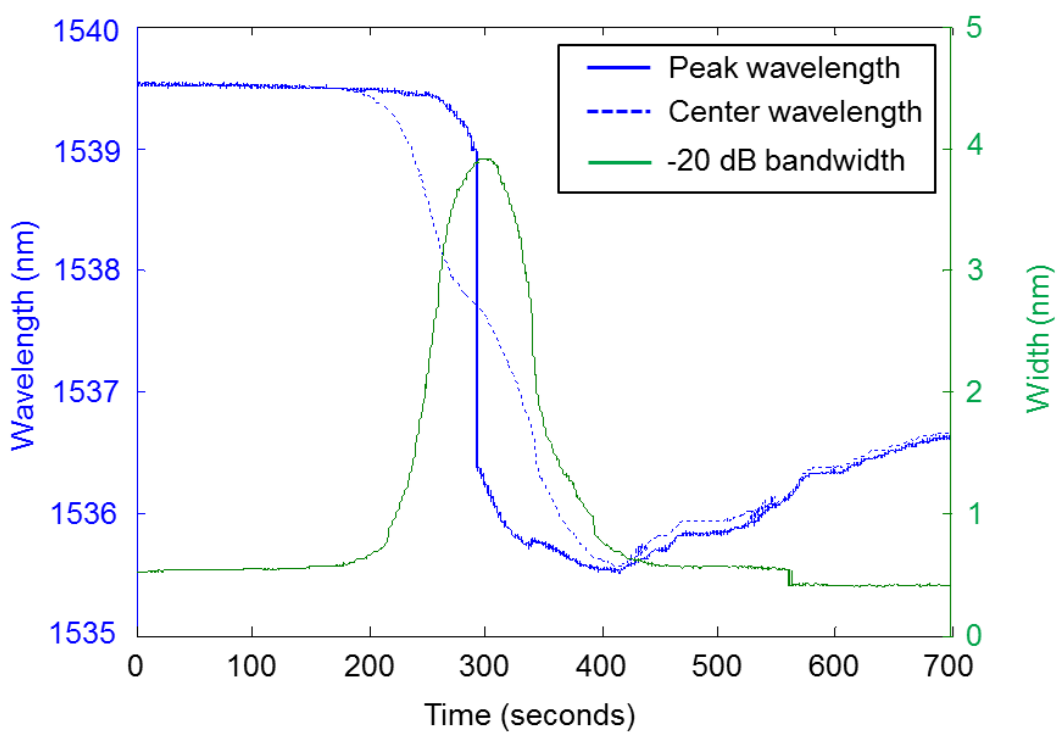

Figure 46. Time-histories of the peak wavelength, center wavelength, and bandwidth during the mode-I interlaminar fracture test with a +6 sensor embedding location

The peak wavelength, center wavelength, and -20 dB bandwidth measured during the Mode-I interlaminar fracture test on a DCB specimen with a +2 sensor embedding location are shown in Figure 47. Embedding the FBG sensor closer to the mid-plane and propagating crack causes the signals to show a small amount of noise and fluctuation. It is clear that the signals at a +2 sensor embedding location are not as smooth as the signals at a +6 sensor embedding location.

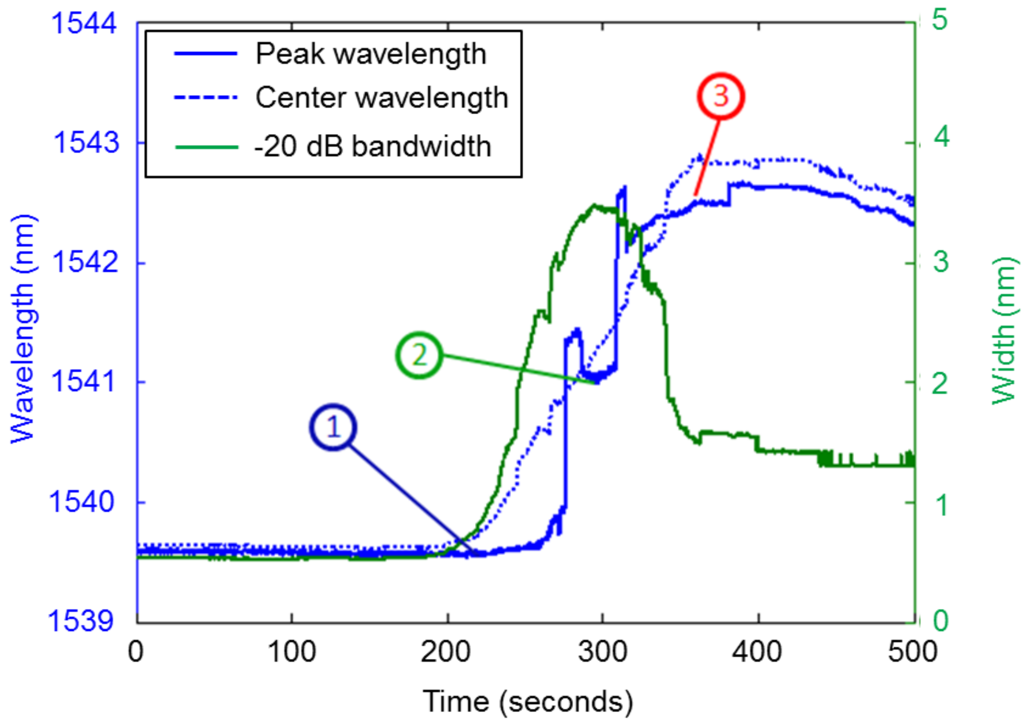

Figure 47. Time-histories of the peak wavelength, center wavelength, and bandwidth during the mode-I interlaminar fracture test with a +2 sensor embedding location

The reflection spectra at the three different points indicated in Figure 47 are shown in Figure 48. In the previous test, it was shown that the reflection spectrum at point 2 displayed only two distinct peaks as is typically expected when an FBG sensor is subjected to non-uniform strain. However, in this test, the reflection spectrum at point 2 displays more than two distinct peaks. The presence of more than two distinct peaks in the reflection spectrum causes problems for the peak intensity ratio monitoring method used by previous research groups for monitoring crack growth.

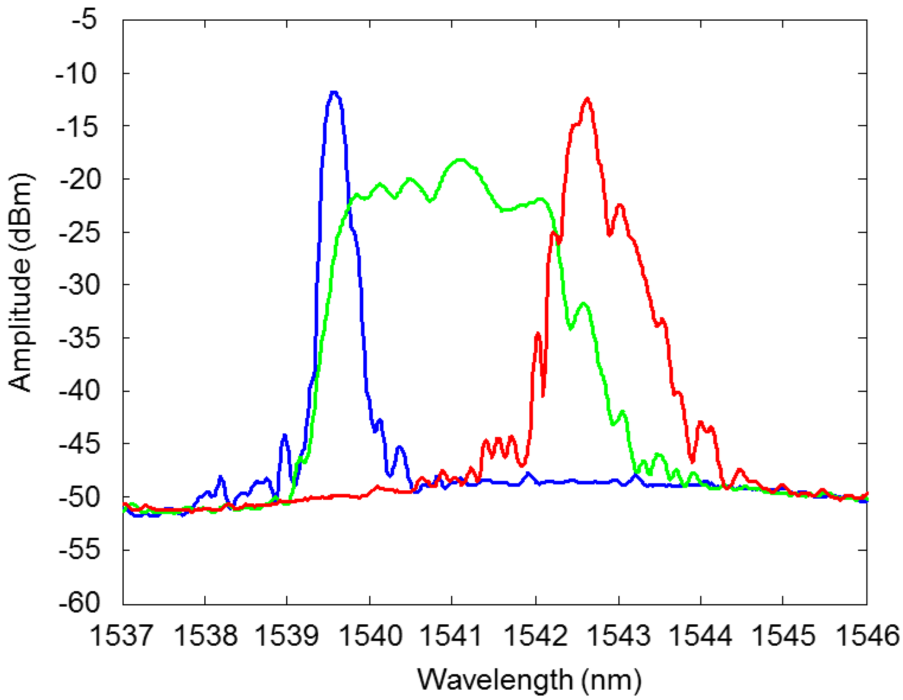

Figure 48. Reflection spectra at the three points indicated in Figure 47

Validation Experiment 2 – Mixed-Mode Bending Experiment

In order to verify the crack detection capability of the FBG sensors under more complex loading conditions, the reflection spectrum of the FBG sensor during the mixed-mode bending test is analyzed by following the same procedure. The time-histories of the peak wavelength, center wavelength, and bandwidth measured during the mixed-mode fracture test with a +6 sensor embedding location are shown in Figure 49. The peak and center wavelength signals differ from those of the Mode-I case in that the signals show a steady increase of wavelength prior to crack detection. This gradual shift is caused by the uniform axial strain due to the global bending of the specimen. It is noted that the bandwidth signal remains unchanged until the interlaminar crack reaches the vicinity of the FBG sensor. This result indicates that the spectrum bandwidth is insensitive to the uniform strain and detects only the non-uniform strain caused by the interlaminar crack. Therefore, monitoring the spectrum bandwidth not only provides early detection of crack propagation but also differentiates the normal structural responses from the responses due to the localized defects.

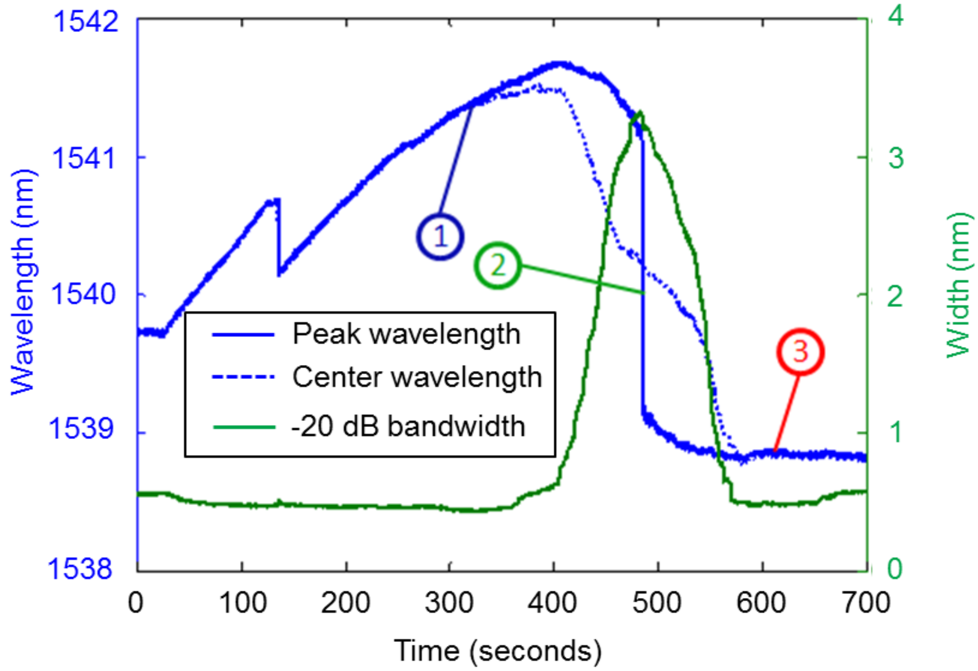

Figure 49. Time-histories of the peak wavelength, center wavelength, and bandwidth during the mixed-mode interlaminar fracture test with a +6 sensor embedding location

The reflection spectra at the three different points indicated in Figure 49 are shown in Figure 50. The reflection spectrum at point 2 is nearly flat at the peak amplitude and just barely displays two distinct peaks. A reflection spectrum of this type is very close to presenting a significant problem to the peak intensity monitoring method because if the spectrum were to remain flat at the peak amplitude, two distinct peaks would not be identified and damage would not be detected.

The time-histories of the peak wavelength, center wavelength, and bandwidth measured during the mixed-mode fracture test with a +2 sensor embedding location are shown in Figure 51. The smoothness of the signals shows little difference when compared to those at the +6 sensor embedding location.

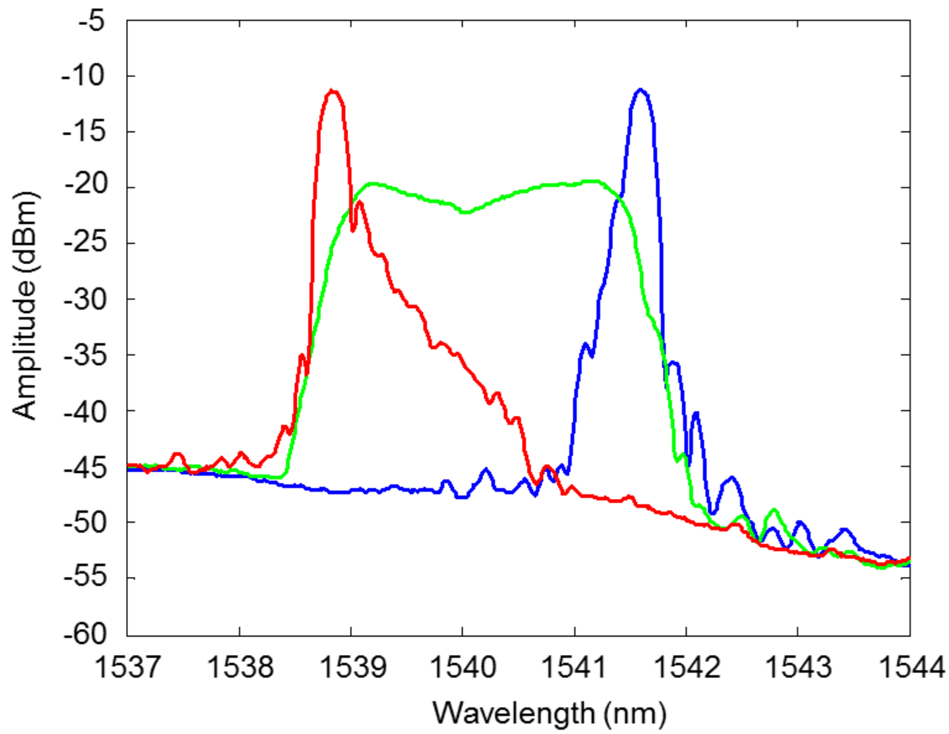

Figure 50. Reflection spectra at the three points indicated in Figure 49

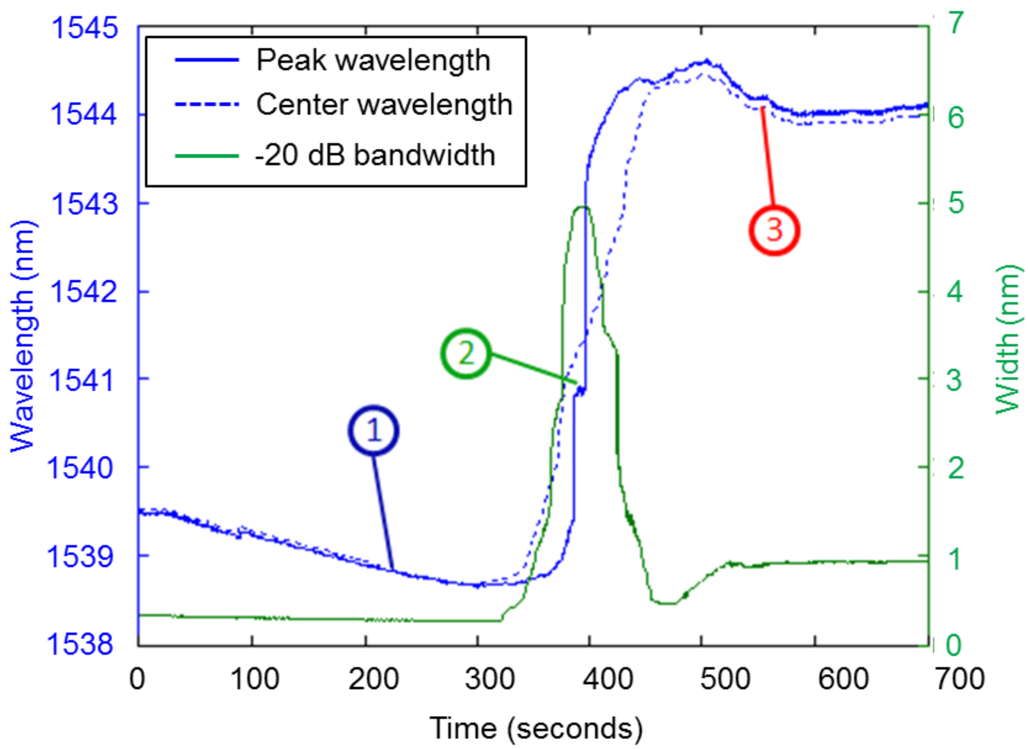

Figure 51. Time-histories of the peak wavelength, center wavelength, and bandwidth during the mixed-mode interlaminar fracture test with a +2 sensor embedding location

The reflection spectra at the three different points indicated in Figure 51 are shown in Figure 52. The presence of more than two distinct peaks in the reflection spectrum at point 2 could again present problems for the peak intensity ratio monitoring method.

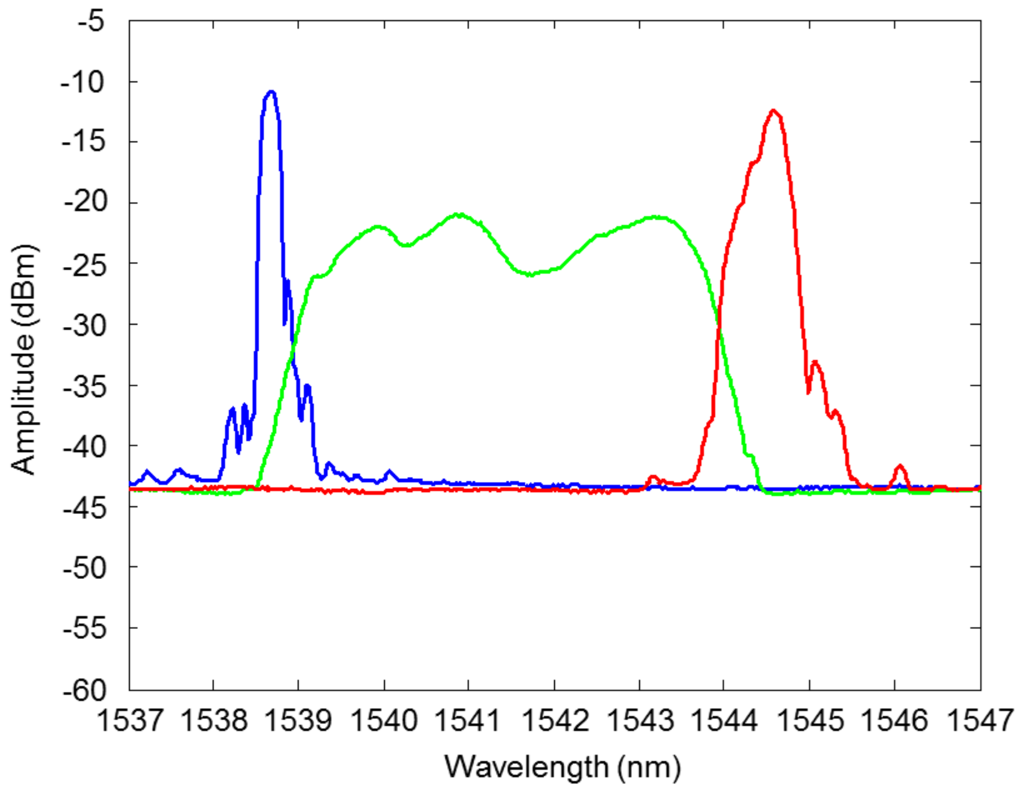

Figure 52. Reflection spectra at the three points indicated in Figure 51

Validation Experiment 3 – End-Notched Flexure Specimen Subject to Cyclic Loading

In order to demonstrate the applicability of the spectral-bandwidth monitoring to interlaminar fatigue crack growth, the reflection spectrum obtained during the ENF fatigue test is analyzed using the same procedure. The time-history of the interlaminar fatigue crack growth under cyclic Mode-II loading is shown in Figure 53. The crack tip position was determined from the compliance of the ENF specimen calibrated with various delamination lengths. It is shown that the crack propagated along the FBG sensor in a slow and stable manner.

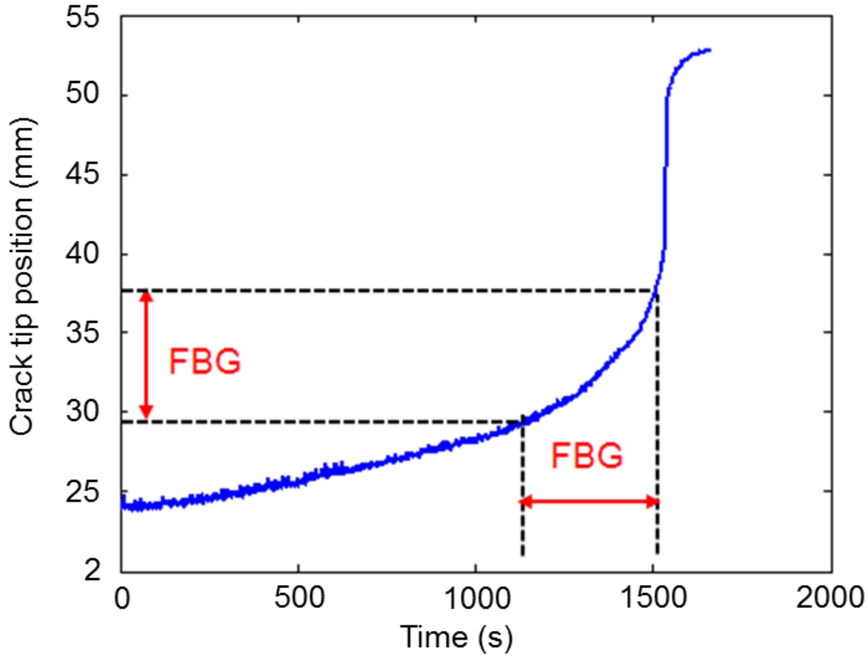

Figure 53. Time-history of interlaminar fatigue crack growth in an edge-notched-flexure specimen

The time-histories of the peak wavelength, center wavelength, and bandwidth measured during the fatigue test are shown in Figure 54. The initial Bragg wavelength of the sensor is approximately 1540 nm. The peak wavelength signal oscillates in a way that mirrors the cyclic loading applied to the specimen. The amplitude of the oscillation remains constant until the fatigue crack reaches the location of the FBG sensor. During this period, the bandwidth signal does not show any oscillation, which indicates that the sensor is subjected to uniform compressive strain due to the bending of the beam. The changes in the amplitude and sign of the wavelength shift shown at approximately 1400 seconds indicate that the crack tip has passed the location of the sensor and the loading applied to the sensor has changed from compression to tension. The amplitude of the bandwidth oscillation increases as the crack tip reaches the location of the sensor and causes non-uniform strain within the gauge section. It is important to note that the increase of the bandwidth amplitude is detected approximately 200 seconds earlier than the changes in the peak wavelength signals. As the crack tip travels across the gauge section, the amplitude of the bandwidth signal attains a maximum and decreases to zero. As discussed earlier, monitoring the bandwidth signal provides the unique benefit of detecting localized defects even in the presence of complex loading modes and fatigue spectrum.

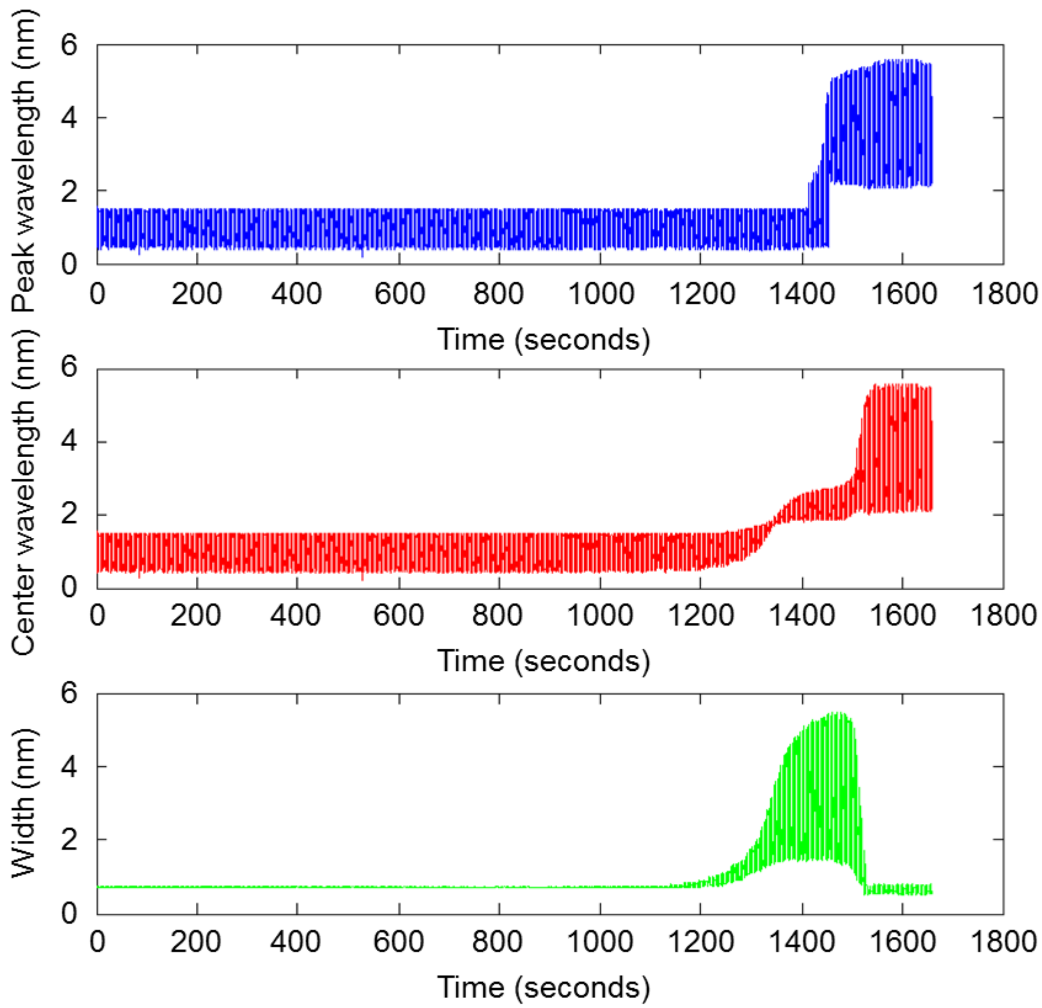

Figure 54. Time-histories of the peak wavelength, center wavelength, and bandwidth during the mode-II interlaminar fatigue test.

Findings

Multiple experiments were performed to monitor interlaminar crack growth in a composite specimen with an embedded FBG sensor. The reflection spectrum was measured during the experiments using three spectrum quantification parameters: peak wavelength, center wavelength, and the optimal parameter identified with the numerical analysis in Chapter 5 – bandwidth. In the Mode-I and Mixed-Mode fracture tests, it was found that the center wavelength and bandwidth monitoring methods were able to detect damage prior to the peak wavelength method. In the Mode-II fatigue test, it was also found that the center wavelength and bandwidth monitoring methods were able to detect damage earlier. Additionally, measuring the spectral response with the bandwidth method allowed the signal to remain constant despite the fluctuation from cyclic loading experienced by the peak and center wavelength methods.

The spectral bandwidth monitoring method has been shown to be a more robust and effective method than the previous monitoring method of peak wavelength and the peak intensity ratio method previously employed by Takeda et al. [27, 32, 33] through multiple experiments and various bending modes.

Specimen with Multiple Embedded FBG Sensors

After improving upon past methods of monitoring crack growth in small-scale composite specimen with a single FBG sensor, it is of interest to transition to larger specimen with multiple embedded FBG sensors. In the previous experiments, the crack propagation direction and approximate position was known, however it is important to investigate scenarios where the crack propagation direction is not known or the point at which damage will occur is not known. Using multiple embedding locations and spacing out the positioning of the sensors will increase the damage detection probability in such scenarios and cover a more sufficient area in large-scale composite panels. The next chapter will focus on this task.

CHAPTER 7
DEVELOPMENT OF A SMART COMPOSITE PANEL

Introduction

A large-scale, thick-section woven composite panel with multiple embedded FBG sensors was created using the Vacuum-Assisted Resign Transfer Molding (VARTM) process to investigate its self-diagnostic ability after sustaining impact damage. A proof loading test, meant to represent in-service loading of a large panel, was performed on the smart composite panel both before and after impact damage to investigate the change in peak wavelength shift of the sensors. The difference in behavior of the peak wavelength shift signal during proof loading before and after the panel was impacted was used to detect impact damage.

Previous work

Previous work done by Takeda [46] et al. employed compression loading of a large composite panel with multiple embedded FBG sensors to detect impact damage based on the behavior of the reflection spectrum of the FBG sensors. The problem with this method is that the research group only demonstrated the damage detection ability by further damaging the panel. For structural health monitoring purposes, this is unacceptable because the method should be capable of monitoring for defects without further increasing the damage. While this group also demonstrated the ability to detect the dynamic impact event with a high frequency interrogator, it is necessary to research alternative monitoring methods using low frequency interrogators because high frequency interrogators are extremely expensive.

Objectives

A new method for monitoring and detecting damage caused by impact loading on a thick-section woven composite panel using multiple embedded FBG sensors will be developed and demonstrated. The method will show that damage can be passively detected simply by utilizing the natural bending of the panel that occurs in applications where the panel itself or the structure it is attached to is experiencing periodic stress from usage.

Manufacturing of the Smart Composite Panel

A woven composite panel of 609.6 x 304.8 x 10.16 mm^3 (16 plies) was prepared to be cured using the VARTM process as shown in Figure 55. The panel was designed to allow two smart composite panels, each containing 3 embedded FBG sensors, and two dummy composite panels without FBG sensors to be cut from it.

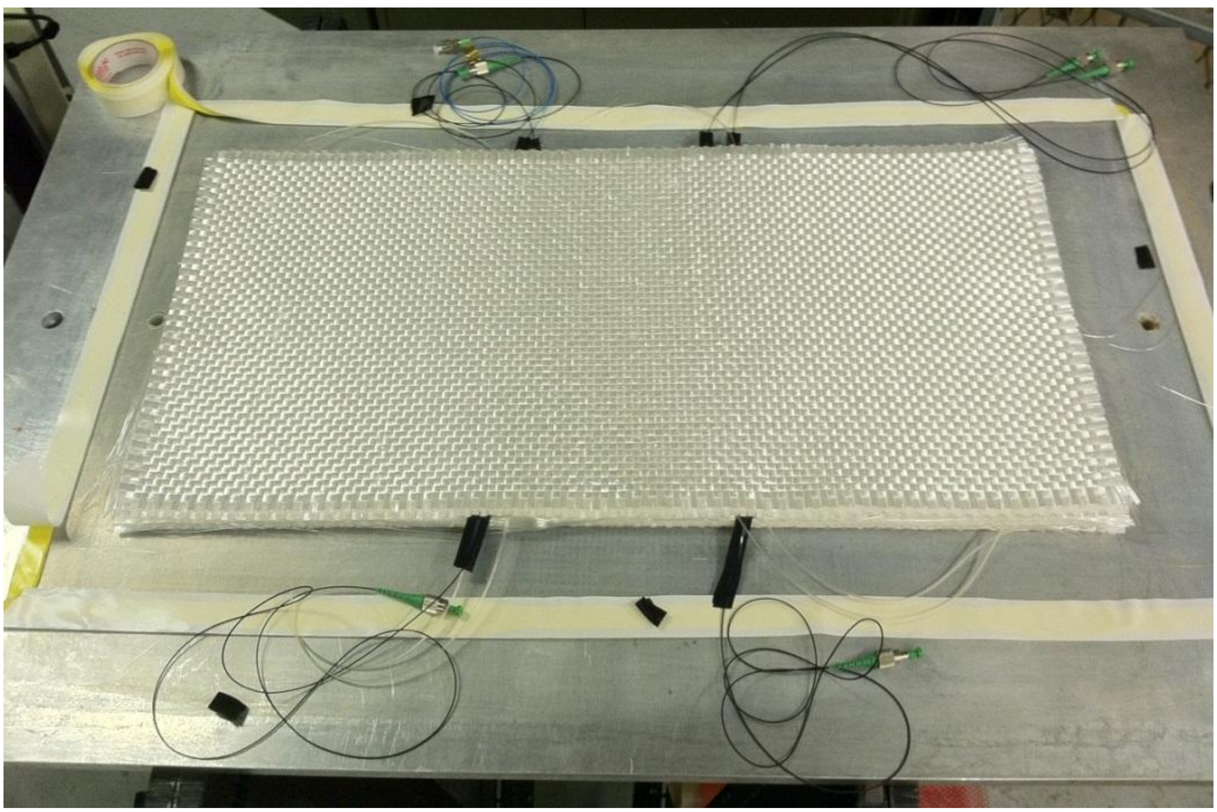

Figure 55. Lay-up of woven composite plies before VARTM

During the hand lay-up of the woven plies, six FBG sensors were embedded approximately 7.62 mm (12 plies) from the surface by threading the optical fiber underneath a single weave until the gauge length was positioned beneath it as seen in Figure 56. A cross-sectional view of the embedding location of the FBG sensors in the thickness of the panel is shown in Figure 57.

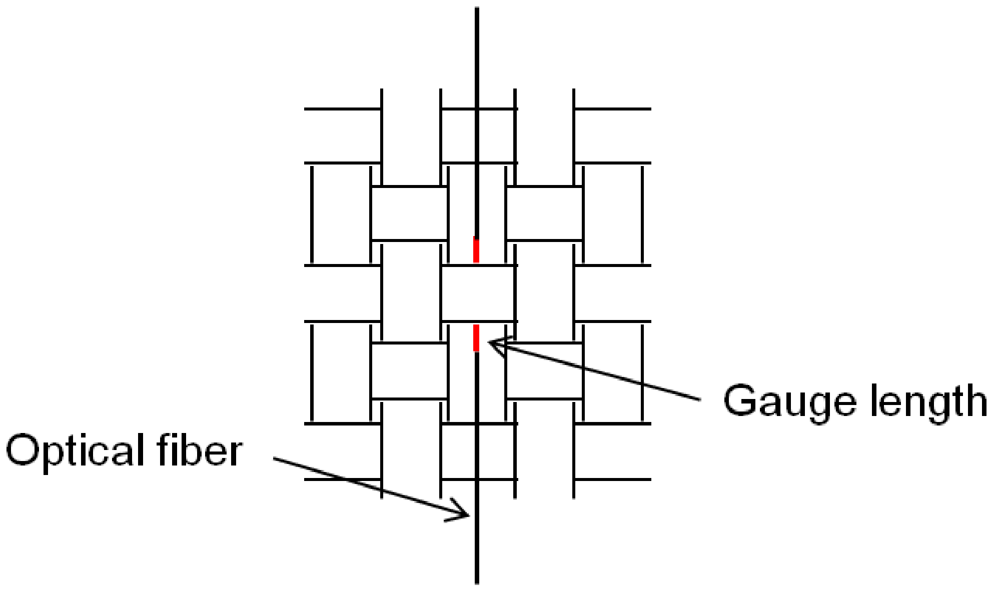

Figure 56. Embedding position of FBG sensor in woven layer

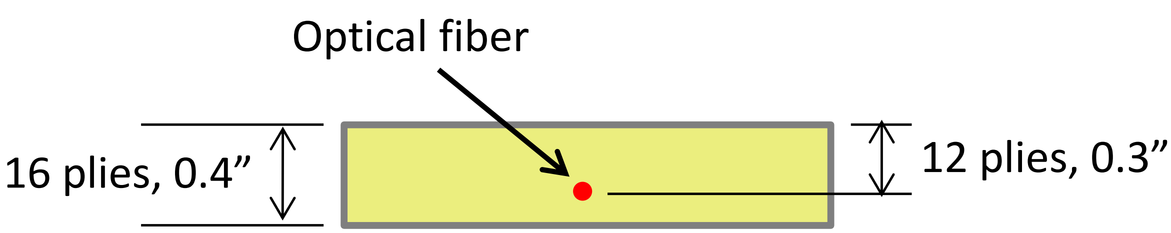

Figure 57. Cross-sectional view of the embedding location of FBG sensors in the thickness of the panel

The positioning of the FBG sensors for the smart composite panels is shown in Figure 58. The sensors were positioned so that they would all be within the loading span during the proof loading test.

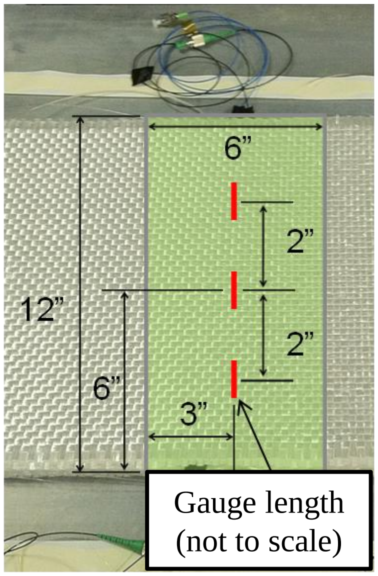

Figure 58. Positioning of FBG sensors in woven composite panel and smart composite panel dimensions

The plate configuration during the VARTM process is shown in Figure 59. Multiple vacuum bags were required to ensure a tight seal as air leakage occurred if the coated optical fibers were not on the inside of the yellow tacky tape. The resin used was two-part epoxy (SC-15 - Applied Poleramics) mixed at a 100:30 ratio of part A:B, respectively. After the resin was pulled through the panel, it was cured in a hot oven for 2 hours at 60 °C followed by 4 hours at 94 °C.

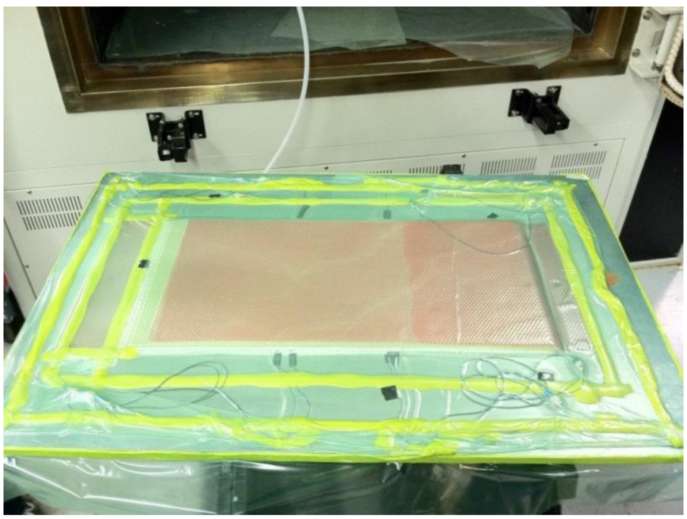
Figure 59. Plate configuration during the VARTM process

One of the final smart composite panels cut from the completed 304.8 x 609.6 mm^2 plate and the FBG sensor embedding locations is shown in Figure 60.

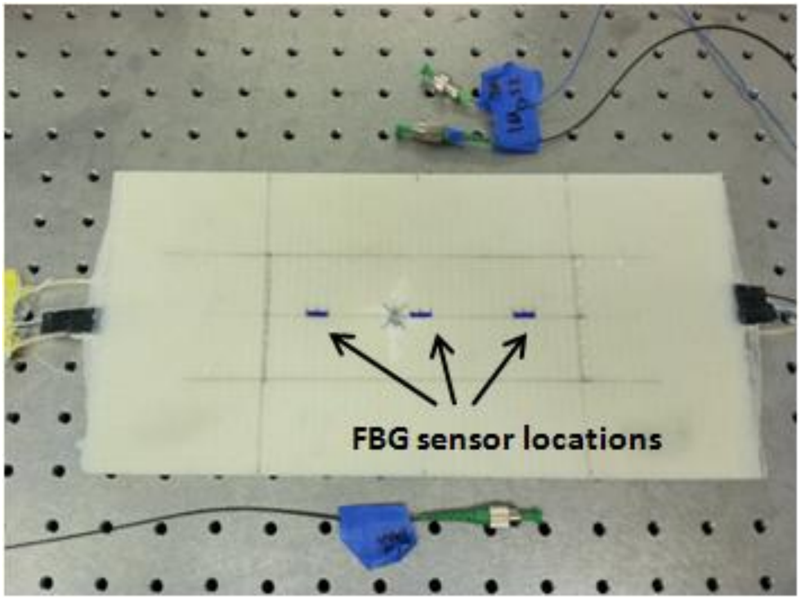

Figure 60. Smart composite panel with FBG sensor embedding locations

Proof Loading Test

A proof loading bending test was performed on the smart composite panel (SCP) prior to impact damage. The SCP was centered in a 4-point bending fixture with a support span and loading span of 203.2 mm and 152.4 mm, respectively. The FBG sensors were nearest to the bottom of the SCP. The test set-up is shown in Figure 62. The SCP was twice loaded and unloaded to a peak load of 35 kN at a constant displacement rate of 5 mm/min. The time histories of the load and displacement during proof loading of the undamaged panel are shown in Figure 61. The loading remained within the linear-elastic region of the material to prevent unwanted damage prior to impact testing. It was critical that the SCP remained undamaged to ensure all damage incurred was solely the result of impact damage. During loading, the reflection spectra of the FBG sensors were recorded using a Micron Optics interrogator (sm-125) for later analysis.

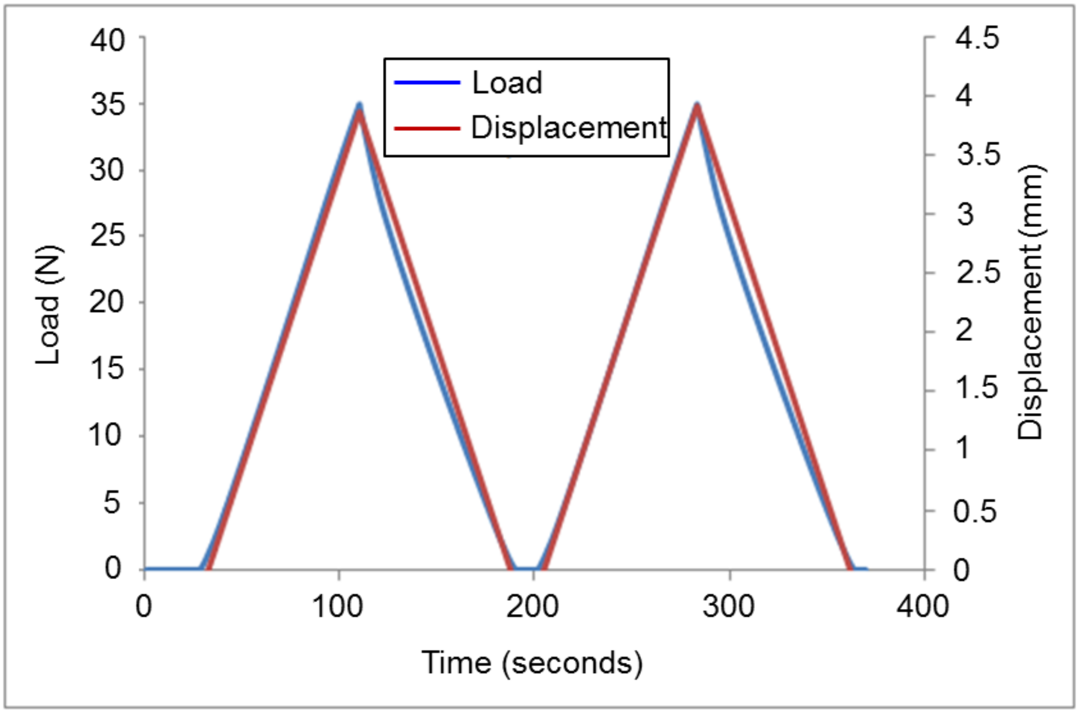

Figure 61. Time histories of load and displacement during proof loading of the undamaged SCP

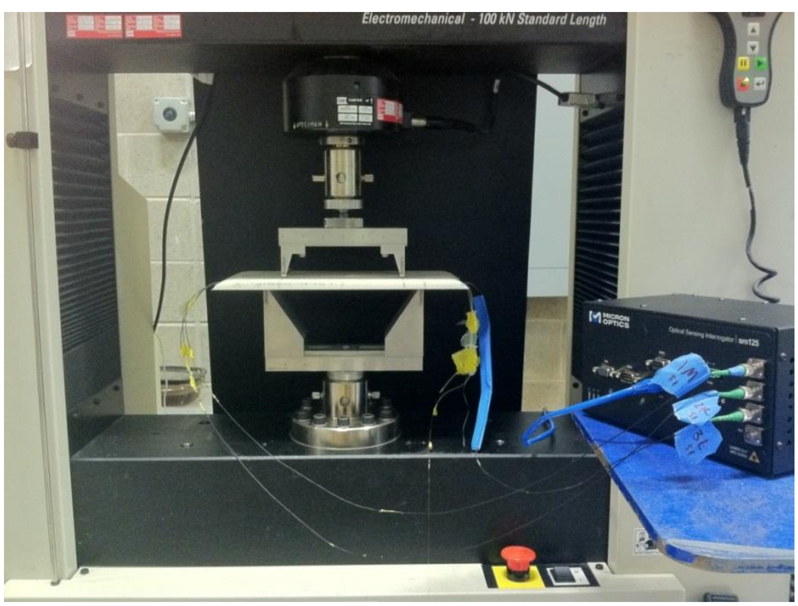

Figure 62. Proof loading test set-up

Drop-Weight Impact Test

After proof loading of the undamaged SCP, damage was inflicted using an Instron drop-weight impact tower. The SCP was subjected to 135 J of impact energy at the impact location indicated in Figure 63. This particular amount of impact energy was chosen because it created a damage area with an approximate two inch diameter. This allowed for the point of impact to be a sufficient distance away from the middle sensor while still encompassing it in the damage area. The impact location was chosen so that each sensor was a different distance away from impact. The SCP was impacted on the rough side of the panel 12 plies (7.62 mm) away from the embedded FBG sensors.

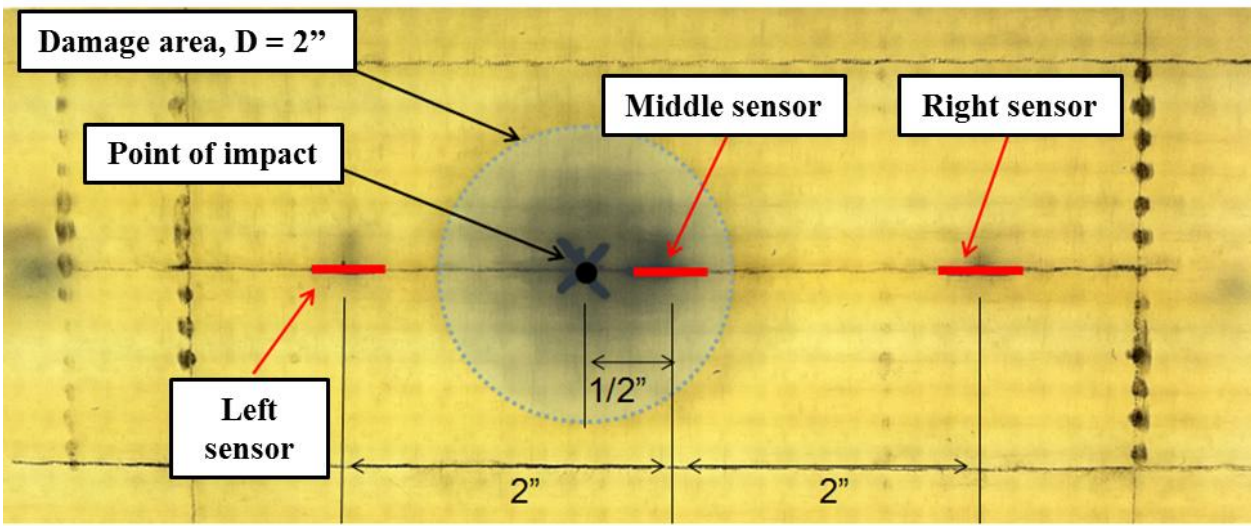

Figure 63. Impact location and damage area

The support fixture on which the SCP was placed for impact loading using the drop-weight impact tower is shown in Figure 64. The SCP was secured to the support fixture at each roller using a rubber band to prevent rebounding upon impact.

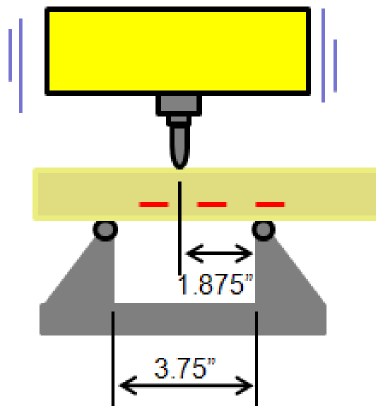

Figure 64. The support fixture on which the SCP was placed for impact loading using the drop-weight impact tower

After impact testing, a final proof loading bending test was performed on the damaged SCP. Proof loading of the damaged SCP was carried out in the same manner as proof loading of the undamaged SCP and again the reflection spectra of the FBG sensors were recorded. The time histories of the load and displacement during proof loading of the damaged SCP are shown in Figure 65.

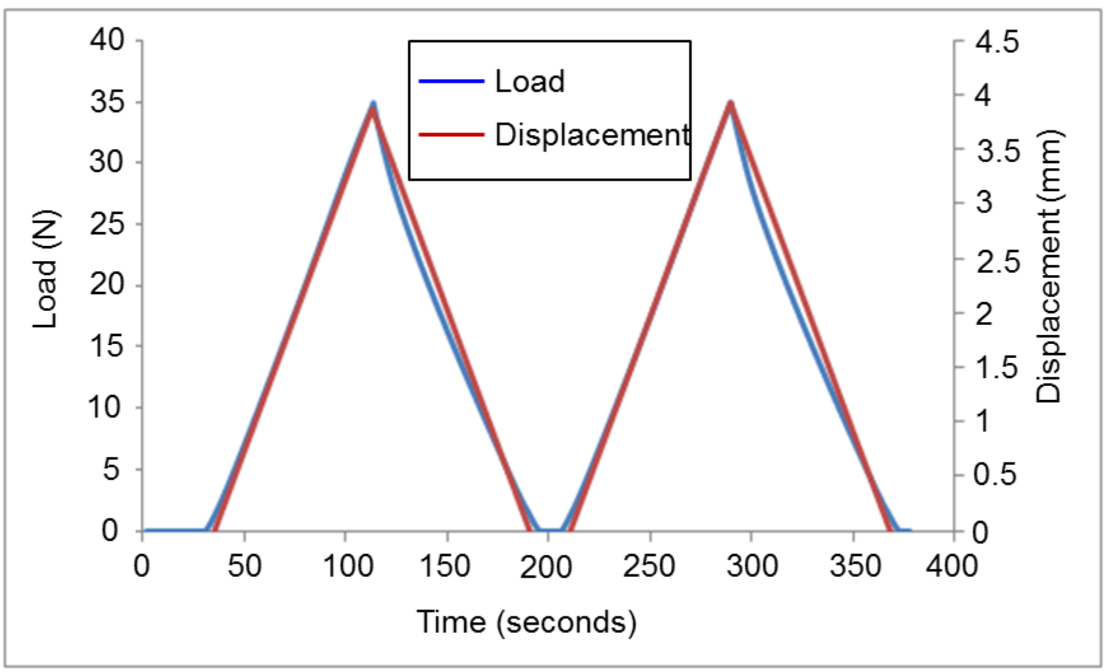

Figure 65. Time histories of load and displacement during proof loading of the damaged SCP

Detecting Damage by Monitoring Peak Wavelength Shift

The time histories of the peak wavelength shift of the embedded FBG sensors during the proof loading test before and after impact damage on the SCP are shown in Figure 66 and Figure 67, respectively. The peak wavelength shift is measured as the difference between the current peak wavelength at time *t* and the initial peak wavelength.

Prior to impact damage, the sensors are shown to be functioning properly as they all follow the two loading cycles without any discrepancies. After impact damage, the middle sensor, located within the damage zone, no longer follows the linear rise and fall of the loading cycles and only reaches a third of the maximum peak wavelength shift reached during proof loading before impact damage. This change in behavior is a clear indication that the impact damage was detected by the middle sensor. It was predicted that the impact damage would cause the panel to become more compliant and therefore the peak wavelength shift would increase in magnitude rather than decrease. However, the embedding of the FBG sensor into the weave rather than in between plies may have caused this discrepancy. The desensitization of the sensor to strain after damage is believed to be caused by the separation of the sensor from the woven threads due to impact thus limiting its ability to bend with the panel. It may have also been caused by the less compliant, undamaged areas of the panel near the edges taking on the stress during loading and absorbing a significant amount of strain away from the damaged area.

The left sensor, the second closest sensor to the damage zone, was also able to detect damage albeit with a less significant change in peak wavelength shift during proof loading after impact. The peak wavelength shift of the left sensor shows significant fluctuation during both loading and unloading cycles and this indicates damage is nearby. Alternatively, the right sensor, the furthest sensor from the damage zone, remains unchanged.

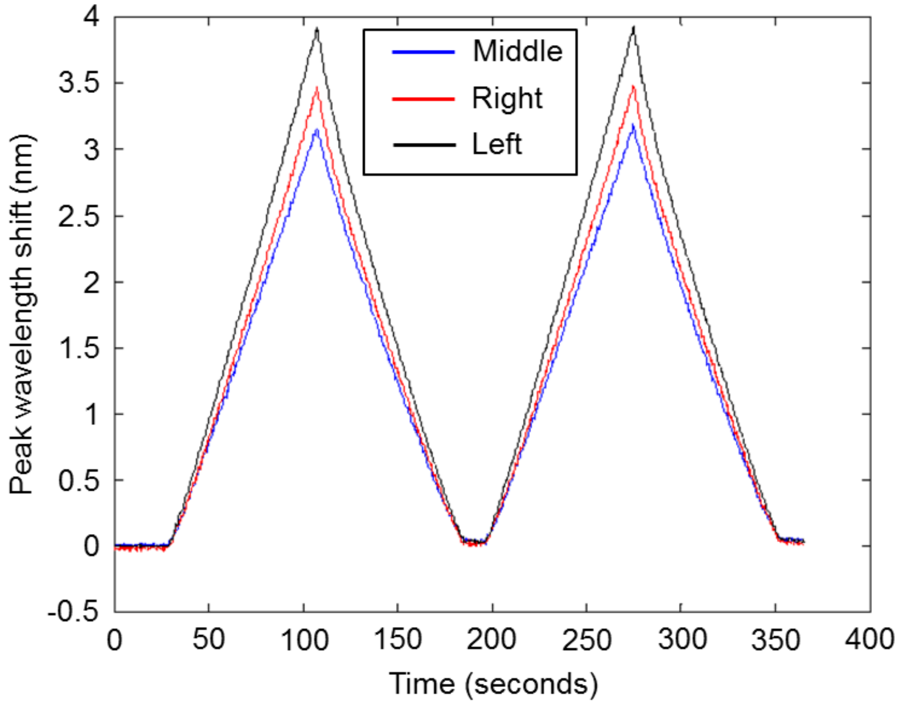

Figure 66. Time history of peak wavelength shift of the embedded FBG sensors during the proof loading test before impact damage on the SCP

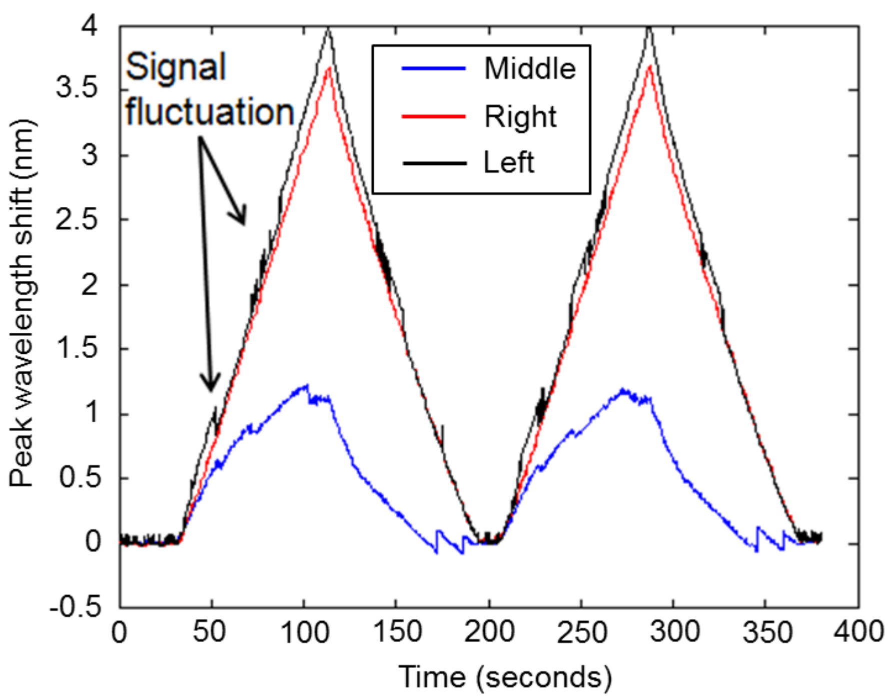

Figure 67. Time history of peak wavelength shift of the embedded FBG sensors during the proof loading test after impact damage on the SCP

Findings

A new method that aims to utilize the passive loading and unloading of a composite structure in service for impact detection purposes has been found to be effective. This new method was tested on a large-scale, thick-section composite panel with three embedded FBG sensors subjected to proof loading meant to simulate the passive stresses on a structure both before and after impact damage to investigate the difference in spectral response. The sensors' signals were monitored before and after impact during proof loading and the presence of impact damage was detected by monitoring the peak wavelength shift of the sensors located within or nearby the damage zone.

Future Work on Smart Composite Panels

Future work would include developing the capability to locate impact damage based on the response of the embedded FBG sensors. This could be done by determining the FBG sensor embedding locations that optimize impact damage detection capability relative to the impact energy. Additionally, the size and thickness of the panel could be increased while implementing additional FBG sensors to achieve a closer representation of a full-scale panel.

CHAPTER 8
CONCLUSIONS

The development of real-time structural health monitoring techniques for composite structures using embedded FBG sensors was thoroughly detailed. A new sensor interrogation method was introduced based on a numerical analysis of an FBG sensor subjected to non-uniform strain. The current interrogation method for damage detection was improved upon using the new sensor interrogation method that made earlier detection times possible in multiple bending modes as demonstrated in various experiments. Small-scale health monitoring capabilities were extended to thick-section composite panels with multiple FBG sensors to investigate and transition to large-scale applications.

Durability testing of FBG sensors embedded in composite laminates was performed through quasi-static tension testing and drop-weight impact testing. In quasi-static tension testing, the embedded sensors survived until catastrophic failure of the specimen. It was found that exceeding the prescribed sensor cut-off point incurred a residual effect on the reflection spectrum causing it to lose intensity upon the reintroduction of strain to the sensor. The embedded sensors subjected to impact loading survived multiple localized impacts and failed only when complete splitting in the fiber direction of the specimen occurred. Impacts directly centered on the center of an embedded sensor's gauge length caused the reflection spectrum to broaden and reduce in intensity as the number of impacts increased. It was found that embedded FBG sensors remained intact and functional until failure of the composite. The survivability of embedded FBG sensors was adequately established.

The Mode-I and Mode-II fracture toughness of Cycom 1003, a glass fiber/epoxy composite, were measured and baseline testing parameters were set to achieve stable crack propagation for future testing of DCB and ENF specimens with embedded FBG sensors. An improved method for measuring the Mode-I fracture toughness for a translucent composite material was presented. By slightly modifying the procedure outlined in ASTM D 5528, more data points were produced and more accurate data was obtained. The Mode-II fracture toughness was calculated albeit with a high percent of variation as expected when unstable crack propagation is present. An attempt was made at stabilizing the crack by increasing the a/L ratio in the specimen but testing showed an inconsistent ability to produce a stable crack propagation in more than one specimen.

A numerical analysis utilizing a transfer matrix formulation was used to investigate the effect of non-uniform strain on an FBG sensor's response. A new interrogation method of the reflection spectrum using bandwidth and center wavelength was introduced. A nearly linear relationship between bandwidth and strain gradient was found when a -20 dB bandwidth was used to quantify the reflection spectrum of a sensor subjected to linear strain. This relationship held true for a highly non-uniform strain distribution and was unaffected by the introduction of a second order term to create a quadratic strain distribution. The reflection spectrum resulting from a simulated propagating crack was measured using the peak intensity ratio method and the proposed bandwidth method. It was shown that the bandwidth method detected the propagating crack before the peak intensity ratio method if the -10 or -20 dB bandwidth measurement was used.

Three experiments were conducted to validate the findings of the numerical analysis. First, damage was monitored using the newly proposed interrogation method by an FBG sensor embedded in DCB and MMB composite specimens subjected to Mode-I and Mixed-mode bending interlaminar fracture tests, respectively. Monitoring the reflection spectrum using the newly proposed method allowed for earlier damage detection than the peak wavelength monitoring method. An additional experiment was conducted in which damage was monitored by an FBG sensor embedded in an ENF composite specimen subjected to a Mode-II bending interlaminar fatigue test. Cyclic loading was used to create stable crack propagation in an ENF specimen. The sensor survived the duration of fatigue loading and the new interrogation method demonstrated the ability to detect damage earlier than the peak wavelength method.

A new method for monitoring and detecting damage caused by an impact event on a large-scale, thick-section woven composite panel using multiple embedded FBG sensors was developed. A proof loading test, meant to represent in-service loading of a large panel, was performed on the smart composite panel both before and after impact damage to investigate the change in peak wavelength shift of the sensors. It was found that irregular behavior of the peak wavelength shift during proof loading of the damaged smart composite panel acted as a good indicator that impact damage was detected. The FBG sensors embedded within and nearby the damage zone detected the presence of damage.

This work hopes to provide the bridge between simple, single FBG sensor experiments to complex, multiple FBG sensor large-scale applications that is necessary for the development of full-scale smart panels in composite structures. The research conducted not only establishes the excellent feasibility of FBG sensors for real-time structural health monitoring but also improves upon past interrogation methods and develops a new damage monitoring method that will be crucial to implementing thick-section smart composite panels.

APPENDIX

APPENDIX

Distribution Statement

UNCLASSIFIED: Distribution Statement A. Approved for public release.

Derivation of Interlaminar Fracture Toughness Curve

$$G_c = \frac{F^2}{2B}\left(\frac{dC}{da}\right)$$

$$C = \left(\frac{8a^3}{EBh^3}\right)$$

$$G_c = \frac{F^2}{2B}\left(\frac{24a^2}{EBh^3}\right)$$

$$G_c = \frac{12F^2a^2}{EB^2h^3}$$

$$a^3 = \frac{CEBh^3}{8}$$

$$G_c = \frac{12F^2}{EB^2h^3}\left(\frac{CEBh^3}{8}\right)^{2/3}$$

$$G_c = \frac{12F^2}{EB^2h^3}\left(\frac{(\Delta/F)EBh^3}{8}\right)^{2/3}$$

$$G_c = \frac{3F^{4/3}\Delta^{2/3}}{E^{1/3}B^{4/3}h^2}$$

$$\left(F^{4/3}\right)^{3/4} = \left(\frac{G_cE^{1/3}B^{4/3}h^2}{3\Delta^{2/3}}\right)^{3/4}$$

$$F = \left(\frac{G_c^3Eh^3}{27}\right)^{1/4} B\Delta^{-1/2}$$

REFERENCES

REFERENCES

1. M. Kobayashi, K.-T. Wu, L. Song, C.-K. Jen and N. Mrad, "Structural health monitoring of composites using integrated flexible piezoelectric ultrasonic transducers," *Journal of Intelligent Material Systems and Structures* 20, (2009): 969-977.

2. L. Yin, X.-M. Wang and Y.-P. Shen, "Damage-monitoring in composite laminates by piezoelectric films," *Computers & Structures* 59, no. 4 (1996): 623-630.

3. C. Ramos, R. de Oliveira, A. T. Marques and O. Frazao, "Measurement of dynamic strain using an optic fibre system in adaptive composite laminates with an integrated piezoelectric sensor/actuator," *Optica Applicata* 41, no. 1 (2011): 79-88.

4. H. T. Banks, D. J. Inman, D. J. Leo and Y. Wang, "An experimentally validated damage detection theory in smart structures," *Journal of Sound and Vibration* 191, no. 5 (1996): 859-880.

5. S.G. Galea, W.K. Chiu and J. Paul, "Use of piezoelectric films in detecting and monitoring damage in composites," *Journal of Intelligent Material Systems and Structures* 4, (1993): 330-336.

6. P. Tan and L. Y. Tong, "Delamination detection of composite beams using piezoelectric sensors with evenly distributed electrode strips," *Journal of Composite Materials* 38, no. 4 (2004): 321-352.

7. P. Tan and L. Y. Tong, "Identification of delamination in a composite beam using integrated piezoelectric sensor/actuator layer," *Composite Structures* 66, no. 1-4 (2004): 391-398.

8. X. P. Qing, S. J. Beard, A. Kumar and T. K. Ooi, "Built-in sensor network for structural health monitoring of composite structure," *Journal of Intelligent Material Systems and Structures* 18, (2007): 39-49.

9. I.-G. Kim, H.-Y. Lee and J.-W. Kim, "Impact damage detection in composite laminates using PVDF and PZT sensor signals," *Journal of Intelligent Material Systems and Structures* 16, (2005): 1007-1013.

10. W.K. Chiu, S.C. Galea, H. Zhang, R. Jones, and Y.C. Lam, "The use of piezoelectric thin film sensors for structural integrity monitoring," *Journal of Intelligent Material Systems and Structures* 5, (1994): 683-693.

11. I. Kim, H. T. Hahn and D. Weems, "Impact monitoring in smart composite structures using piezoelectric sensors," *Proceedings of 6th Japan-U.S. Conference on Composite Materials,* Technomics Pub Co., pp. 201-210.

12. C. Y. Park, I. Kim and Y. S. Lee, “Monitoring of low-velocity impact damage initiation of gr/ep panel using piezoelectric thin film sensor,” *Journal of the Korean Society for Composite Materials* 15, no. 2 (2002): 11-17.

13. J. Haywood, P. T. Coverley, W. J. Staszewski, and K. Worden, “An automatic impact monitor for a composite panel employing smart sensor technology,” *Smart Material Structures* 14, (2005): 265-271.

14. F. T. Calkins, A. B. Flatau and M. J. Dapino, “Overview of magnetostrictive sensor technology,” *Journal of Intelligent Material Systems and Structures* 18, (2007): 1057-1066.

15. X. Chen and M. Anjanappa, “Health monitoring of composites embedded with magnetostrictive thick film without disassembly,” *Smart Material Structures* 15, (2006): 20-32.

16. H. Kwun and K. A. Bartels, “Magnetostrictive sensor technology and its applications,” *Ultrasonics* 36, (1998): 171-178.

17. P. Tan and L. Y. Tong, “Multiple delamination detection of composite beam using magnetostrictive patch,” *AIAA Journal* 44, no. 11 (2006): 2547-2551.

18. A. V. Krishnamurthy, M. Anjanappa, Z. Wang and X. Chen, “Sensing of delaminations in composite laminates using embedded magnetostrictive particle layers,” *Journal of Intelligent Material Systems and Structures* 10, (1999): 825-835.

19. R. Jones and S. Galea. “Health monitoring of composite repairs and joints using optical fibres.” *Composite Structures* 58 (November 2002): 397-403.

20. H.-Y. Ling, K.-T. Lau, and L. Cheng. “Determination of dynamic strain profile and delamination detection of composite structures using embedded multiplexed fibre-optic sensors.” *Composite Structures* 66 (October 2004): 317-326.

21. S. Minakuchi, Y. Okabe, and N. Takeda. “Real-time detection of debonding between honeycomb core and facesheet using a small-diameter FBG sensor embedded in adhesive layer.” *Journal of Sandwich Structures and Materials* 9 (January 1, 2007): 9-33.

22. Y. Okabe, J. Kuwahara, K. Natori, N. Takeda, T. Ogisu, S. Kojima, and S. Komatsuzaki. “Evaluation of debonding progress in composite bonded structures using ultrasonic waves received in fiber Bragg grating sensors.” *Smart Materials and Structures* 16 (August 1, 2007): 1370-1378.

23. Y. Okabe, R. Tsuji, and N. Takeda. “Application of chirped fiber Bragg grating sensors for identification of crack locations in composites.” *Composites Part A: Applied Science and Manufacturing* 35 (January 2004): 59-65.

24. L. Sorensen, J. Botsis, T. Gmür, and J. Cugnoni. “Delamination detection and characterisation of bridging tractions using long FBG optical sensors.” *Composites Part A: Applied Science and Manufacturing* 38 (October 2007): 2087-2096.

25. N. Takeda, Y. Okabe, and T. Mizutani. “Damage detection in composites using optical fibre sensors.” *Proceedings of the Institution of Mechanical Engineers, Part G: Journal of Aerospace Engineering* 221 (January 1, 2007): 497-508.

26. N. Takeda, Y. Okabe, J. Kuwahara, S. Kojima, and T. Ogisu. “Development of smart composite structures with small-diameter fiber Bragg grating sensors for damage detection: Quantitative evaluation of delamination length in CFRP laminates using Lamb wave sensing.” *Composites Science and Technology* 65 (December 2005): 2575-2587.

27. S. Takeda, Y. Okabe, and N. Takeda. “Delamination detection in CFRP laminates with embedded small-diameter fiber Bragg grating sensors.” *Composites Part A: Applied Science and Manufacturing* 33 (July 2002): 971-980.

28. S. Takeda, Y. Okabe, and N. Takeda. “Monitoring of Delamination Growth in CFRP Laminates using Chirped FBG Sensors.” *Journal of Intelligent Material Systems and Structures* 19 (May 10, 2007): 437-444.

29. S. Yashiro, T. Okabe, and N. Takeda. “Damage identification in a holed CFRP laminate using a chirped fiber Bragg grating sensor.” *Composites Science and Technology* 67 (February 2007): 286-295.

30. G. Zhou, and L. M. Sim. “Damage detection and assessment in fibre-reinforced composite structures with embedded fibre optic sensors-review.” *Smart Materials and Structures* 11 (December 1, 2002): 925-939.

31. Y. Okabe, S. Yashiro, T. Kosaka, and N. Takeda, “Detection of transverse cracks in CFRP composites using embedded fiber Bragg grating sensors,” *Smart materials and structures* 9 (2000): 832.

32. S. Takeda, Y. Okabe, T. Yamamoto, and N. Takeda, “Detection of edge delamination in CFRP laminates under cyclic loading using small-diameter FBG sensors,” *Composites science and technology* 63, no. 13 (2003): 1885–1894.

33. S. Takeda, T. Yamamoto, Y. Okabe, and N. Takeda, “Debonding monitoring of composite repair patches using embedded small-diameter FBG sensors,” *Smart materials and structures* 16 (2007): 763.

34. H. Y. Ling, K. T. Kau, Z. Su, and E. T. T. Wong, “Monitoring mode II fracture behaviour of composite laminates using embedded fiber-optic sensors,” *Composites Part B: Engineering* 38, no. 4 (2007): 488–497.

35. K. S. C. Kuang and W. J. Cantwell, "Detection of impact damage in thermoplastic-based fiber-metal laminates using optical fiber sensors," *Journal of Materials Science Letters* 21, no. 17 (2002): 1351-1354.

36. A. Chambers, M. Mowlem, and L. Dokos. "Evaluating impact damage in CFRP using fibre optic sensors." *Composites Science and Technology* 67 (May 2007): 1235-1242.

37. C.-C. Chang, and J. S. Sirkis. "Design of fiber optic sensor systems for low velocity impact detection." *Smart Materials and Structures* 7 (April 1, 1998): 166-177.

38. C. Park, K. Peters, M. Zikry, Todd Haber, Stephen Schultz, and Richard Selfridge. "Peak wavelength interrogation of fiber Bragg grating sensors during impact events." *Smart Materials and Structures* 19 (April 1, 2010): 045015.

39. H. Tsuda, N. Toyama, K. Urabe, and J. Takatsubo. "Impact damage detection in CFRP using fiber Bragg gratings." *Smart Materials and Structures* 13 (August 1, 2004): 719-724.

40. H. Tsutsui, A. Kawamata, J. Kimoto, A. Isoe, Y. Hirose, T. Sanda, and N. Takeda. "Impact damage detection system using small-diameter optical-fiber sensors embedded in CFRP laminate structures." *Advanced Composite Materials* 13 (March 1, 2004): 43-55.

41. H. Tsutsui, A. Kawamata, T. Sanda, and N. Takeda. "Detection of impact damage of stiffened composite panels using embedded small-diameter optical fibers." *Smart Materials and Structures* 13 (December 1, 2004): 1284-1290.

42. T. Vella, S. Chadderdon, R. Selfridge, S. Schultz, S. Webb, C. Park, K. Peters, and M. Zikry. "Full-spectrum interrogation of fiber Bragg gratings at 100 kHz for detection of impact loading." *Measurement Science and Technology* 21 (September 1, 2010): 094009.

43. S. Takeda, S. Minakuchi, Y. Okabe, and N. Takeda. "Delamination monitoring of laminated composites subjected to low-velocity impact using small-diameter FBG sensors." *Composites Part A: Applied Science and Manufacturing* 36 (July 2005): 903-908.

44. R. J. Van Steenkiste and G. S. Springer, *Strain and Temperature Measurement with Fiber Optic Sensors*, Lancaster, PA: Technomic, 1997.

45. J. Ang, H.C.H. Li, I. Herszberg, M.K. Bannister, A.P. Mouritz, "Tensile fatigue properties of fibre Bragg grating optical fibre sensors," *International Journal of Fatigue* 32, no. 4 (2010): 762-768.

46. S-i. Takeda, Y. Aoki, Y. Nagao, Monitoring of CFRP stiffened panel under compressive loading using FBG sensors, Composite Structures (2011), doi:10.1016/j.compstruct.2011.02.020.

47. M. Yamada and K. Sakuda, "Analysis of almost-periodic distributed feedback slab waveguide via a fundamental matrix approach," *Applied Optics* 26, (1987): 2474-2478.

48. S. Yashiro, N. Takeda, T. Okabe, and H. Sekine. "A new approach to predicting multiple damage states in composite laminates with embedded FBG sensors." *Composites science and technology* 65, no. 3-4 (2005): 659–667.

49. H. Ling, K. Lau, L. Cheng, and K. Chow, "Embedded fibre Bragg grating sensors for non-uniform strain sensing in composite structures," *Meas Sci Technol* 16, (2005) 2415–2424.

50. H.-y. Ling, K.-t. Lau, L. Cheng, and K.-w. Chow, "Embedded fiber Bragg grating sensors for non-uniform strain sensing in composite structures," *Measurement Science and Technology* 16 (2005): 2415-2424.

51. A. Gill, K. Peters, and M. Struder, "Genetic algorithm for the reconstruction of Bragg grating sensor strain profiles," *Measurement Science and Technology* 15 (2004): 1877-1884.

52. S. Huang, M. M. Ohn, R. M. Measures, "Phase-based Bragg intragrating distributed strain sensor," *Applied Optics* 35, no. 7 (1995): 1135-1142.

53. H. R. Williams, R. S. Trask, and I.P. Bond, "Self-healing sandwich panels: Restoration of compressive strength after impact," *Composites Science and Technology* 68 (2008): 3171-3177.

54. E. Kirkby, R. de Oliveira, V. Michaud, and J. A. Manson, "Impact localization with FBG for a self-healing carbon fibre composite structure," *Composite Structures* 94 (2011): 8-14.

55. H. Jeong, and Y. S. Jang, "Wavelet analysis of plate wave propagation in composite laminates," *Composite Structures* 49 (2000): 443–50.

56. H. A. Haus, "Mirrors and interferometers," in *Waves and Fields in Optoelectronics,* N. Holonyak, ed. (Prentice-Hall, Englewood Cliffs, N.J., 1984), Chap. 3, p. 55-80.

57. S. Huang, M. LeBlanc, and M. M. Ohn, "Bragg intragrating structural sensing," *Applied Optics* 34, no. 22 (1995): 5003–5009.

58. T. Erdogan, "Fiber grating spectra," *J. Lightwave Technol.*, vol.15, pp. 1227-1294, Aug. 1997.

59. M. Prabhugoud and K. Peters, "Modified Transfer Matrix Formulation for Bragg Grating Strain Sensors," *Journal of Lightwave Technology* 22, no. 10 (10, 2004): 2302-2309.

60. ASTM D 5528-01 (Reapproved 2007), "Mode I Interlaminar Fracture Toughness of Unidirectional Fiber-Reinforced Polymer Matrix Composites," ASTM International, W. Conshohocken, Pa. (first issued in 1994).

61. R. J. Sanford, *Principles of Fracture Mechanics,* Prentice Hall, Upper Saddle River, NJ, 2003.

62. S. N. Chatterjee, "Analysis of Test Specimens for Interlaminar Mode II Fracture Toughness, Parts 1 and 2," J. Comp. Mater., Vol 25, 1991, pp. 470-493 and pp. 494-511.

63. ASTM D 790-10, "Standard Test Methods for Flexural Properties of Unreinforced and Reinforced Plastics and Electrical Insulating Materials," ASTM International, W. Conshohocken, Pa.

64. W. Hwang and K.S. Han, "Interlaminar fracture behavior and fiber bridging of glass-epoxy composite under mode I static and cyclic loadings," J. Compos. Mater.,23, 396–430 (April,1989).

65. P. Davies, B. R. K. Blackman and A. J. Brunner, 'Standard Test Methods for Delamination Resistance of Composite Materials: Current Status', Applied Composite Materials 5, 1998.

66. K. Kageyama, M. Kikuchi, and N. Yanagisawa, "Stabilized End Notched Flexure Test: Characterization of Mode II Interlaminar Crack Growth," Composite Materials: Fatigue and Fracture, Third Volume, ASTM STP 1110, 1991, pp. 210-225.

67. ASTM D 6671-04, "Standard Test Method for Mixed Mode I–Mode II Interlaminar Fracture Toughness of Unidirectional Fiber Reinforced Polymer Matrix Composites," ASTM International, W. Conshohocken, Pa.

68. "Cytec Cyply 1002 Epoxy Fiberglass Composite, Unidirectional." Cytec Cyply 1002 Epoxy Fiberglass Composite, Unidirectional. Web. 16 Mar. 2010. <http://www.matweb.com/search/datasheet.aspx?matguid=3f2253a553404b13893830617250b5d8&ckck=1>.

69. [25]. Department of Defense Handbook, Composite Materials Handbook, Volume 1. Polymer Matrix Composites Guidelines for Characterization of Structural Materials, 2002.